UNIVERSIDADE ESTADUAL DE CAMPINAS
Instituto de Geociências

RAPHAEL BIANCHI HUNGER

GEOQUÍMICA DE ELEMENTOS TRAÇO E GEOCRONOLOGIA U-Pb EM APATITA DE SISTEMAS COBRE-OURO NEOARQUEANOS E PALEOPROTEROZOICOS DO DOMÍNIO CARAJÁS, BRASIL: IMPLICAÇÕES PARA A EVOLUÇÃO DE FLUIDOS E METALOGÊNESE

TRACE ELEMENT GEOCHEMISTRY AND U-Pb GEOCHRONOLOGY IN APATITE OF NEOARCHEAN AND PALEOPROTEROZOIC COPPER-GOLD SYSTEMS OF THE CARAJÁS DOMAIN, BRAZIL: IMPLICATIONS FOR FLUID EVOLUTION AND METALLOGENESIS

CAMPINAS
2023

RAPHAEL BIANCHI HUNGER

GEOQUÍMICA DE ELEMENTOS TRAÇO E GEOCRONOLOGIA U-Pb EM APATITA DE SISTEMAS COBRE-OURO NEOARQUEANOS E PALEOPROTEROZOICOS DO DOMÍNIO CARAJÁS, BRASIL: IMPLICAÇÕES PARA A EVOLUÇÃO DE FLUIDOS E METALOGÊNESE

TESE APRESENTADA AO INSTITUTO DE GEOCIÊNCIAS DA UNIVERSIDADE ESTADUAL DE CAMPINAS COMO PARTE DOS REQUISITOS EXIGIDOS PARA OBTENÇÃO DO TÍTULO DE DOUTOR EM CIÊNCIAS NA ÁREA DE GEOLOGIA E RECURSOS NATURAIS

ORIENTADOR: PROF. DR. ROBERTO PEREZ XAVIER

COORIENTADORA: PROFA. DRA. CAROLINA PENTEADO NATIVIDADE MORETO

ESTE EXEMPLAR CORRESPONDE À VERSÃO FINAL DA TESE DEFENDIDA PELO ALUNO RAPHAEL BIANCHI HUNGER E ORIENTADA PELO PROF. DR. ROBERTO PEREZ XAVIER

CAMPINAS

2023

Ficha catalográfica
Universidade Estadual de Campinas
Biblioteca do Instituto de Geociências
Marta dos Santos - CRB 8/5892

H109g

Hunger, Raphael Bianchi, 1990-
Trace element geochemistry and U-Pb geochronology in apatite of Neoarchean and Paleoproterozoic copper-gold systems of the Carajás Domain, Brazil : implications for fluid evolution and metallogenesis / Raphael Bianchi Hunger. – Campinas, SP : [s.n.], 2023.

Orientador: Roberto Perez Xavier.
Coorientador: Carolina Penteado Natividade Moreto.
Tese (doutorado) – Universidade Estadual de Campinas, Instituto de Geociências.

1. Depósitos hidrotermais. 2. Geoquímica. 3. Apatita. 4. Geocronologia. 5. Província Mineral de Carajás. I. Xavier, Roberto Perez, 1958-. II. Moreto, Carolina Penteado Natividade, 1985-. III. Universidade Estadual de Campinas. Instituto de Geociências. IV. Título.

Informações Complementares

Título em outro idioma: Geoquímica de elementos traço e geocronologia U-Pb em apatita de sistemas cobre-ouro neoarqueanos e paleoproterozoicos do Domínio Carajás, Brasil : implicações para a evolução de fluidos e metalogênese
Palavras-chave em inglês:
Hydrothermal deposits
Geochemistry
Apatite
Geochronology
Carajás Mineral Province
Área de concentração: Geologia e Recursos Naturais
Titulação: Doutor em Geociências
Banca examinadora:
Roberto Perez Xavier [Orientador]
David Josef Cornelius Debruyne
Rafael Rodrigues de Assis
Glaucia Nascimento Queiroga
Felipe Holanda dos Santos
Data de defesa: 31-08-2023
Programa de Pós-Graduação: Geociências

Identificação e informações acadêmicas do(a) aluno(a)
- ORCID do autor: https://orcid.org/0000-0003-3712-8406
- Currículo Lattes do autor: http://lattes.cnpq.br/1837273377441629

UNIVERSIDADE ESTADUAL DE CAMPINAS
INSTITUTO DE GEOCIÊNCIAS

UNICAMP

AUTOR: Raphael Bianchi Hunger

GEOQUÍMICA DE ELEMENTOS TRAÇO E GEOCRONOLOGIA U-PB EM APATITA DE SISTEMAS COBRE-OURO NEOARQUEANOS E PALEOPROTEROZOICOS DO DOMÍNIO CARAJÁS, BRASIL: IMPLICAÇÕES PARA A EVOLUÇÃO DE FLUIDOS E METALOGÊNESE

TRACE ELEMENT GEOCHEMISTRY AND U-PB GEOCHRONOLOGY IN APATITE OF NEOARCHEAN AND PALEOPROTEROZOIC COPPER-GOLD SYSTEMS OF THE CARAJÁS DOMAIN, BRAZIL: IMPLICATIONS FOR FLUID EVOLUTION AND METALLOGENESIS

ORIENTADOR: PROF. DR. ROBERTO PEREZ XAVIER
COORIENTADORA: PROFA. DRA. CAROLINA PENTEADO NATIVIDADE MORETO

Aprovada em: 31/08/2023

EXAMINADORES:

Prof. Dr. Roberto Perez Xavier - Presidente

Prof. Dr. David Jozef Cornelius Debruyne

Prof. Dr. Rafael Rodrigues de Assis

Profa. Dra. Glaucia Nascimento Queiroga

Prof. Dr. Felipe Holanda dos Santos

A Ata de Defesa assinada pelos membros da Comissão Examinadora consta no processo de vida acadêmica do aluno.

Campinas, 31 de agosto de 2023.

SÚMULA CURRICULAR

RAPHAEL BIANCHI HUNGER

Possui graduação em Geologia (2015) e mestrado em Geociências (2017) pela Universidade Estadual de Campinas (UNICAMP), sendo atualmente estudante de doutorado em Geociências e Licenciatura em Geografia pela mesma universidade. Realizou estágio de 6 meses (Fev-Mar/2020 e Jan-Abr/2022) no *Cardiff Earth Laboratory for Trace Element and Isotope Chemistry* (CELTIC) da *Cardiff University*, através do Programa Institucional de Doutorado Sanduíche no Exterior (DSE), no âmbito da CAPES/PrInt-Unicamp. Tem experiência na área de Geociências, com ênfase em Metalogênese, Petrografia, Mineralogia, Geologia Isotópica, Inclusões Fluidas e Geocronologia. Atuou como monitor em diversas disciplinas da graduação, incluindo Mineralogia, Geologia Econômica, Sedimentologia, Estratigrafia, Elementos de Geologia para Biologistas, Petrografia e Petrologia Ígnea, Sistemas de Informações Georreferenciadas (SIG), Sensoriamento Remoto e Geoquímica Analítica. Foi membro da equipe de Orientação Educacional e corpo docente (professor de Geografia) do Curso Vilarejo (2020). Durante o primeiro semestre de 2021, atuou como professor conferencista da disciplina "Geologia Econômica I" pela Universidade Estadual Paulista (UNESP - Rio Claro). Atualmente é professor de Geografia para o ensino médio e coorientador pedagógico do Colégio Anglo Paulínia.

AGRADECIMENTOS

Meus mais sinceros agradecimentos a todos aqueles que de alguma forma contribuíram para o desenvolvimento desta pesquisa e participaram desta longa e atribulada jornada.

A Deus, por seu Amor incondicional.

À minha família: Elaine, Rodolpho, Fernanda, Lucas, Euterpia, Dagmar, Reinaldo e Thelma. Obrigado por todo amor, carinho, incentivo, suporte emocional e por estarem ao meu lado em todos os momentos!

Aos meus falecidos avô e padrinho: Flávio e Carlos. Independentemente de onde estiverem, sei que ainda olham por mim.

Aos amigos de longa data: Anderson Yin, Tatiane e Rafael Baez, Beatriz Spalletta, Guilherme Paes Leme, Laura Segovia, Alexandre Bliska, Beatris Ferragut, Vinícius Thomazelli, Karen Muzarra, Vonei Cene, Júlia Castelli, Teocarlos Alita, Ricardo Chuffi, João Ralha, Henrique Brandão, Tatiane Meirelles, Pedro e Bruna Pinheiro, Lucas Di Salvo, Helen Nascimento, Maísa Trovó, Thiago Santos, Tales Rodrigues, Mateus Basso, Nathália Prado, Jessica Didole, Gustavo Melo, João Motta, Jozias Bravo, Poliana Vidal, Tainá Nogueira, Caroline Araujo, Marcos Fernando, Letícia Prado, Érica Rodrigues e Rebeca Mayra. Obrigado pela parceria, pelas memórias construídas e por todas aquelas que ainda virão. Amo vocês!

Aos amigos da lendária Rep do Morto: Welison Alves, Rodolfo Tonoli, Bruno Joel, André Sanchez, Lucas Pellegrino. Do ensino médio para a vida! Que Sagarana nos acompanhe.

Aos melhores amigos que a pós-graduação poderia me proporcionar: Poliana Toledo, José Henrique, Bruno Conty, Laura Scarano, Daniel Martins, Éverton Valezio, Sanny Castro, Igor Kamargo, Filipe Faria, Bruna Husak, Alessandra Casagrande, Kamila Fernandes, André Kunifoshita, Robert Muniz, Ian Cerdeira, Ana Carolina Ceolin, Vinicius Gaino, Thaís Nasato. Sou muito grato por ter conhecido cada um de vocês. Obrigado por tornarem essa caminhada mais leve!

Aos meus queridos orientadores: prof. Roberto Xavier e profa. Carolina Moreto, pelos ensinamentos compartilhados, pela paciência, pelas "puxadas de orelha" e pelas discussões que certamente elevaram a qualidade desta pesquisa. Muito obrigado por todo apoio oferecido ao longo de toda a minha trajetória na pós-graduação!

Aos responsáveis pelos laboratórios de pesquisa do Instituto de Geociências da UNICAMP, em especial ao Dailto Silva e a Erica Tonetto, por todo suporte dado nas etapas analíticas deste trabalho.

To the School of Earth and Environmental Sciences of the Cardiff University, for welcoming me as one of their overseas students and allowing me to develop part of my research during my 6-month internship.

To my supervisor at Cardiff University, prof. Morten Andersen, for all the experience shared, the support during the analytical routines in the CELTIC lab and for accepting to be my mentor during my time abroad.

To my dear friend Frantz Ossa Ossa, for every minute dedicated to help me during lab work and the patience and professionalism to explain all procedures. I have learned so much from you.

À Coordenação de Aperfeiçoamento de Pessoal de Nível Superior – CAPES – Código de Financiamento 001, pela bolsa de doutorado com a qual fui contemplado (processo 88882.329728/2019-01) e pela oportunidade de realizar meu doutorado sanduíche através do Programa CAPES-PrInt (Edital PRPG 002/2019).

À Vale, por todo apoio logístico, operacional e financeiro dado durante minha pesquisa de campo e etapas analíticas. Agradeço especialmente a toda a equipe de funcionários do N5 e aos geólogos Fernando Matos, Saney Freitas e Ezequiel Pozocco.

RESUMO

O Domínio Carajás (3,0–2,55 Ga), na porção sudeste do Cráton Amazônico, contém um notável número de depósitos de óxido de ferro-cobre-ouro (IOCG) e tipo *granite-related* formados em épocas metalogenéticas distintas, desde o Neoarqueano (ca. 2,7 e 2,5 Ga) ao Paleoproterozoico (ca. 1,88 Ga). A apatita é um mineral acessório onipresente nestes depósitos, ocorrendo geralmente associada a alterações sódico-cálcicas iniciais ou em paragênese com zonas de minério ricas em sulfetos. Com base em dados de LA-ICP-MS e EPMA *in situ* de cristais de apatita, combinados com imagens de catodoluminescência, investigamos as variações morfológicas e composicionais entre amostras de seis depósitos IOCG do Domínio Carajás, incluindo os depósitos Sequeirinho, GT-46, Grota Funda, Igarapé Bahia, Sossego e Alvo 118, além do depósito tipo *granite-related* Santa Lúcia. Os resultados deste estudo demonstram que os grãos de apatita nestes sistemas são texturalmente complexos e normalmente exibem diferentes domínios sob imagem de catodoluminescência, que são marcados por diferentes composições de elementos traços e padrões de fracionamento ETR distintos. Tais variações composicionais e morfológicas são aqui interpretadas como reflexo da história de interação fluido-apatita durante a evolução hidrotermal em escala de depósito, tendo esta sido regulada por regimes de fluidos distintos que não possuem relação direta com alguma época metalogenética em específico (Neoarqueano vs. Paleoproterozoico). Processos de dissolução-reprecipitação mediados por atividade metassomática foram, portanto, os principais responsáveis pela remobilização interna de ETR na apatita e pela precipitação de fases secundárias ricas em ETR (e.g., monazita, allanita, xenotima) associadas a domínios alterados nos grãos analisados. As condições redox que operaram durante o desenvolvimento dos processos hidrotermais que afetaram a apatita nos depósitos estudados variam de relativamente reduzidas (Sequeirinho, GT-46, Grota Funda e Sossego) a estados mais oxidados (Santa Lúcia, Igarapé Bahia/Alemão e Alvo 118). Por fim, os resultados de geocronologia U-Pb obtidos neste estudo sugerem que a apatita relacionada ao minério do depósito Santa Lúcia registrou uma sobreposição de eventos metassomáticos que envolveu pelo menos três pulsos hidrotermais distintos, abrangendo o Neoarqueano (ca. 2,56 Ga) e o Paleoproterozoico (ca. 2,1 e 1,81 Ga).

Palavras-chave: Depósitos hidrotermais; Geoquímica; Apatita; Geocronologia; Província Mineral de Carajás.

ABSTRACT

The Meso- to Neoarchean (3.0–2.55 Ga) Carajás Domain, in the southeastern portion of the Amazonian Craton, contains a remarkable number of iron oxide-copper-gold (IOCG) and granite-related Cu-Au-(Sn-Bi-W) deposits formed at distinct metallogenic epochs that span from the Neoarchean (ca. 2.7 and 2.5 Ga) to the Paleoproterozoic (ca. 1.88 Ga). Apatite is a ubiquitous accessory mineral in these deposits, generally occurring associated with early sodic-calcic alteration assemblages or in paragenesis with sulfide-rich ore zones. Based on *in-situ* LA-ICP-MS and EPMA data of apatite, combined with cathodoluminescence imaging, we investigate morphological and compositional variations among samples from six IOCG deposits of the Carajás Domain, including the Sequeirinho, GT-46, Grota Funda, Igarapé Bahia, Sossego and Alvo 118 deposits, as well as the Santa Lúcia granite-related deposit. The results of this study demonstrate that apatite grains in these systems are texturally complex and normally exhibit different domains under cathodoluminescence imaging, which are marked by distinctive trace element compositions and rare earth element (REE) patterns. Such compositional and morphological variations are here interpreted to reflect the history of fluid-apatite interaction at a deposit scale, which involved distinct fluid regimes that had no specific connection with metallogenic epochs in particular (Neoarchean vs. Paleoproterozoic). Coupled dissolution-reprecipitation processes mediated by metasomatic activity were, therefore, the main responsible for REE internal remobilization within apatite and the precipitation of secondary REE-bearing phases (e.g., monazite, allanite, xenotime) associated with altered domains in the analysed grains. Redox conditions operating during the course of hydrothermal processes that affected apatite in the studied deposits vary from relatively reduced (Sequeirinho, GT-46, Grota Funda, and Sossego) to more oxidized states (Santa Lúcia, Igarapé Bahia/Alemão, and Alvo 118). Lastly, U-Pb results obtained in this study suggest that ore-related apatite from the Santa Lúcia deposit recorded a superimposition of metasomatic events that involved at least three distinct hydrothermal pulses, spanning from the Neoarchean (ca. 2.56 Ga) to the Paleoproterozoic (ca. 2.1 and 1.81 Ga).

Keywords: Hydrothermal deposits; Geochemistry; Apatite; Geochronology; Carajás Mineral Province.

LISTA DE ILUSTRAÇÕES

ANEXO A

ANEXO B

LISTA DE TABELAS

ANEXO A

ANEXO B

SUMÁRIO

1. INTRODUÇÃO

A metalogenia do cobre no Domínio Carajás (DC), um segmento Arqueano da Província Carajás na margem sudeste do Cráton Amazônico Brasileiro (**Fig. 1a**), é consideravelmente complexa, contando com múltiplos eventos formadores de minério no tempo. Esses eventos foram as principais causas que levaram à formação de uma ampla variedade de depósitos de cobre no DC, incluindo, entre outros, sistemas de óxido de ferro-cobre-ouro (IOCG) e Cu-Au-(W-Bi-Sn) tipo *granite-related* (POLLARD *et al.*, 2019; XAVIER *et al.*, 2012, 2017). Do ponto de vista genético, características marcantes que diferem os depósitos tipo *granite-related* dos IOCG incluem sua natureza pobre em óxidos de ferro, extensas zonas de alteração ricas em quartzo-muscovita (e.g., greisenização), paragênese de minério relativamente reduzida e afinidade geoquímica por elementos granitófilos (e.g., W, Bi, Sn, Li) (GRAINGER *et al.*, 2008; HUNGER *et al.*, 2021; POLLARD *et al.*, 2019; TALLARICO *et al.*, 2004). O momento de formação dos depósitos IOCG em Carajás é atribuído a pelo menos três grandes episódios mineralizantes (HUNGER *et al.*, 2018; MELO *et al.*, 2016; MORETO *et al.*, 2015a; 2015b; TOLEDO *et al.*, 2019; XAVIER *et al.*, 2017) que ocorreram em um amplo intervalo de tempo entre o início do Neoarqueano (ca. 2,72–2,68 Ga e ca. 2,57 Ga) e o Paleoproterozoico (ca. 1,90–1,87 Ga). Em contrapartida, os depósitos tipo *granite-related* foram formados predominantemente durante o Paleoproterozoico em ca. 1,88 Ga, exceto o depósito Santa Lúcia, que constitui o único representante Neoarqueano (ca. 2,68 Ga; Hunger et al., 2021) desta classe de depósitos conhecido até agora. No entanto, estudos recentes demonstraram que a evolução desses depósitos de cobre-ouro não é necessariamente restrita a uma dessas grandes épocas metalogenéticas, mas, em vez disso, teria envolvido numerosos pulsos hidrotermais que causaram, entre outras coisas, a sobreposição de assembleias de alteração hidrotermal, aporte e remobilização de metais, além da superposição de idades mesmo em escala de depósito (MELO *et al.*, 2021; MORETO *et al.*, 2015a; 2015b; PREVIATO *et al.*, 2020; TOLEDO *et al.*, 2019). Nesse sentido, compreender como esses depósitos evoluíram no tempo têm se mostrado uma tarefa desafiadora em Carajás, tornando-se necessário o uso de novas abordagens para melhor delimitar os processos hidrotermais que levaram à sua formação no DC.

A composição de elementos traço em apatita têm sido amplamente utilizada como uma ferramenta robusta para rastrear processos magmático-hidrotermais em uma variedade de sistemas minerais (BOUZARI *et al.*, 2016; HARLOV, 2015; MAO *et al.*, 2016; MERCER;

WATTS; GROSS, 2020). De fato, a apatita representa um dos fosfatos mais comuns em rochas ígneas (PICCOLI; CANDELA, 2002) e uma fase mineral característica de zonas de alteração hidrotermal ou mineralizadas de uma ampla variedade de sistemas minerais (BARTON, 2014; BROOM-FENDLEY *et al.*, 2016; DECRÉE *et al.*, 2020; SKIRROW, 2022). Devido à sua capacidade de incorporar estruturalmente uma quantidade significativa de elementos, incluindo halogênios (F e Cl), elementos terras raras (ETR), além de importantes metais de transição (HUGHES; RAKOVAN, 2015; PAN; FLEET, 2002), a apatita tem sido amplamente utilizada como um *proxy* para a fugacidade de oxigênio (fO_2) em sistemas magmáticos (CAO *et al.*, 2012; MILES *et al.*, 2014), um traçador detrítico para estudos de proveniência (O'SULLIVAN *et al.*, 2020), e um poderoso indicador petrogenético-metalogenético (BELOUSOVA *et al.*, 2002; MAO *et al.*, 2016; NATHWANI *et al.*, 2020; PAN *et al.*, 2016; SHA; CHAPPELL, 1999). Adicionalmente, a apatita pode representar um geocronômetro U-Pb eficaz, considerando sua temperatura de fechamento de até 600ºC (COCHRANE *et al.*, 2014; KIRKLAND *et al.*, 2018).

Embora relativamente resistente ao intemperismo e à difusão isotópica abaixo de 550°C (COLE; CHAKRABORTY, 2001), a apatita é particularmente sensível a processos de dissolução-reprecipitação induzidos por fluidos, que são geralmente responsáveis por promover mudanças em sua composição e textura (HARLOV, 2015; HARLOV; WIRTH; FÖRSTER, 2005). Através dessas mudanças, a apatita é capaz de registrar informações cruciais acerca da sobreposição de eventos metassomáticos no tempo, definindo assim diferentes estágios de formação (BOUZARI *et al.*, 2016; ZIRNER *et al.*, 2015). Deste modo, a partir do uso integrado de dados químicos e evidências texturais, estas últimas geralmente acessadas por catodoluminescência ou imagens de elétrons retroespalhados, a apatita representa uma excelente ferramenta para investigar a história geoquímica de sistemas magmático-hidrotermais complexos (BOUZARI *et al.*, 2016; DECRÉE *et al.*, 2020-; LU *et al.*, 2021; MERCER; WATTS; GROSS, 2020).

Em Carajás, a apatita representa um mineral acessório típico de zonas de minério ricas em sulfetos ou um componente de assembleias minerais de alteração sódico-cálcica iniciais que eventualmente acompanham a formação de corpos de magnetita maciços nos depósitos de cobre-ouro (HUNGER *et al.*, 2021; MONTEIRO *et al.*, 2008a; XAVIER *et al.*, 2012). Apesar de sua ocorrência comum, no entanto, estudos prévios utilizando apatita para rastrear processos magmático-hidrotermais nesses depósitos ainda são escassos e essencialmente concentrados em alguns casos de estudo (DINIZ *et al.*, 2023; XAVIER *et al.*,

2011). Assim, este estudo combina imagens de catodoluminescência com dados obtidos através de análises *in-situ* por ablação a laser via espectrometria de massa com plasma acoplado indutivamente (LA-ICP-MS) e por microssonda eletrônica (EPMA), para investigar variações morfológicas e composicionais entre cristais de apatita de sete depósitos de cobre-ouro do DC, formados em diferentes épocas metalogenéticas e em distintos contextos geológicos locais.

2. OBJETIVOS

O objetivo desta pesquisa em nível de doutorado é realizar a caracterização textural e química de cristais de apatita associados a zonas de alteração hidrotermal e mineralizadas de depósitos cobre-ouro da Província Carajás, de modo a:

1) Determinar possíveis mecanismos de mobilização hidrotermal de elementos traço em apatita, assim como identificar eventos de sobreposição, visando melhor caracterizar a evolução dos fluidos nesses depósitos de cobre-ouro;
2) Identificar semelhanças e contrastes geoquímicos entre os depósitos estudados, que possam apresentar implicações para a metalogênese do Domínio Carajás;
3) Estabelecer a cronologia de eventos hidrotermais responsáveis por processos de dissolução-reprecipitação de apatita no depósito tipo *granite-related* Santa Lúcia.

3. CONTEXTO GEOLÓGICO REGIONAL DO DOMÍNIO CARAJÁS

O DC (**Fig. 1b–c**), na porção norte da Província Carajás, é limitado ao sul pelo Domínio Rio Maria (DRM) e, ao norte, pelo Domínio Bacajá (DB). O DRM constitui um terreno granito-*greenstone* Mesoarqueano (3,0–2,86 Ga; ALMEIDA *et al.*, 2010) composto por suítes tonalito-trondhjemito-granodiorito (TTG), sanukitóides, leucogranitos potássicos e sequências metavulcanossedimentares (ALMEIDA *et al.*, 2011), enquanto o DB consiste predominantemente de granitóides Paleoproterozoicos (2,3–2,05 Ga; MACAMBIRA *et al.*, 2009; VASQUEZ *et al*. 2008a). Segundo Motta *et al.* (2019), os domínios Carajás e Bacajá compartilham uma evolução prolongada e precedente ao Ciclo Orogênico Transamazônico (2,26–1,86 Ga; CORDANI; TEIXEIRA, 2007; TASSINARI; MACAMBIRA, 1999; VASQUEZ *et al.*, 2008b). Tal evolução teria envolvido uma crosta arqueana semelhante, porém configurações litosféricas modificadas quando comparadas a litosfera mais profunda que reside sob o DRM, cuja evolução crustal foi relativamente estável e mais antiga. Uma zona de sutura inferida (Zona de Cisalhamento Buritirama; COSTA *et al*., 2016) separa o DC do bloco Bacajá e é parcialmente composta por sequências deposicionais de plataforma da Formação Buritirama (OLIVEIRA *et al.*, 2017; SALGADO *et al.*, 2019). Em contrapartida, o limite aproximado entre os domínios Carajás e Rio Maria é definido através de uma descontinuidade regional de direção E-W, estabelecida a partir de parâmetros geofísicos (FEIO *et al.*, 2013; MOTTA *et al.*, 2019).

Ortognaisses migmatíticos do Complexo Xingu (2,97–2,86 Ga; AVELAR *et al.*, 1999; MACHADO *et al.*, 1991), o Ortogranulito Chicrim-Cateté (3,0–2,86 Ga; PIDGEON; MACAMBIRA; LAFON, 2000) e sequências tipo *greenstone belt* mesoarqueanas (ca. 2,97 Ga; MORETO *et al.*, 2015; SIEPIERSKI; FERREIRA FILHO, 2016) compreendem as principais rochas de embasamento do DC. Adicionalmente, um conjunto distinto de metagranitóides que incluem, entre outros, os tonalitos Bacaba (ca. 3,0 Ga; MORETO *et al.*, 2011) e Campina Verde (2,87–2,85 Ga; FEIO *et al.*, 2013), o granulito félsico Ouro Verde (3,05 – 2,93 Ga; MARANGOANHA; OLIVEIRA; DALL'AGNOL, 2019) e os granitos Canaã dos Carajás (ca. 2,96 Ga; FEIO *et al.*, 2013), Bom Jesus (ca. 2,83 Ga; FEIO *et al.*, 2013) e Serra Dourada (ca. 2,86 Ga; MORETO *et al.*, 2011), são também considerados parte do embasamento.

Sequências metavulcanossedimentares neoarqueanas (ca. 2,76–2,73 Ga; MARTINS *et al.*, 2017; TALLARICO *et al.*, 2005; TRENDALL *et al.*, 1998) correlacionadas ao Supergrupo Itacaiúnas (DOCEGEO, 1988; MACHADO *et al.*, 1991; WIRTH; GIBBS;

OLSZEWSKI JR., 1986) ocorrem sobrepostas às rochas do embasamento. O Supergrupo Itacaiúnas foi originalmente subdividido nos grupos Igarapé Salobo, Grão Pará, Igarapé Bahia e Igarapé Pojuca (DOCEGEO, 1988) que, segundo Tavares *et al*. (2018), são principalmente representados, da base para o topo, por rochas vulcânicas, formação ferrífera bandada e associações clástico-sedimentares. Alternativamente, Araújo e Nogueira (2019) e Araújo Filho *et al.* (2020) reinterpretaram a estratigrafia das sequências metavulcanossedimentares da Bacia de Carajás e propuseram a seguinte sucessão ascendente: Grupo Grão Pará (formações Parauapebas, Carajás e Igarapé Bahia), sobreposto pelas formações Serra Sul, Azul, Águas Claras e Gorotire.

A Formação Serra Sul representa uma sucessão siliciclástica de aproximadamente 600 m de espessura e composta por diamictitos subglaciais e marinhos, por sua vez intercalados com estratos de argilito e folhelho preto (ca. 2,58–2,06 Ga; ARAÚJO; NOGUEIRA, 2019), que recobrem as sequências metavulcanossedimentares do Grupo Grão Pará. Sobrepondo-se a esses depósitos glaciogênicos, as formações Azul, Águas Claras e Gorotire são predominantemente caracterizadas por um amplo conjunto de conglomerados, arenitos, siltitos e argilitos depositados em ambientes de *offshore* marinho e costeiro-fluvial a aluvial, entre ca. 2,37 e 2,0 Ga (ARAÚJO FILHO; NOGUEIRA; ARAÚJO, 2020; ARAÚJO; NOGUEIRA, 2019; JUSTO *et al.*, 2018; MOUGEOT *et al.*, 1996). Por fim, sucessões sedimentares orosirianas atribuídas ao Grupo Paredão (ca. 2,0 Ga; PEREIRA *et al.*, 2009) afloram em porções do DC e DB e compreendem brechas sedimentares, conglomerados polimíticos a oligomíticos e arenitos imaturos originados em ambientes de leques aluviais continentais e fluviais entrelaçados (TAVARES *et al.*, 2018).

Granitos alcalinos sintectônicos do tipo A2, compreendendo as suítes Plaquê, Planalto, Estrela, Serra do Rabo, Igarapé-Gelado e Pedra Branca (ca. 2,76–2,73 Ga; AVELAR *et al.*, 1999; BARROS *et al.*, 2004, 2009; FEIO *et al.*, 2012, 2013; HUHN; MACAMBIRA; DALL'AGNOL, 1999; SARDINHA; BARROS; KRYMSKY, 2006), além de granitos peralcalinos à metaluminosos formados em ca. 2,57 Ga (Old Salobo, Itacaiúnas e GT-46; MACHADO *et al.*, 1991; SOUZA; MACAMBIRA; SHELLER, 1996; TOLEDO *et al.*, 2019), definem dois grandes episódios de magmatismo granítico de idade Neoarqueana reconhecidos no DC. Além disso, granitos alcalinos à subalcalinos e metaluminosos à levemente peraluminosos da Suíte Intrusiva Serra dos Carajás (granitos Central de Carajás, Young Salobo, Cigano, Pojuca, Breves e Rio Branco; MACHADO *et al.*, 1991; TALLARICO *et al.*, 2004), marcam um evento granítico Paleoproterozoico (ca. 1,88 Ga) de abrangência regional na província. Adicionalmente, episódios de magmatismo máfico-

ultramáfico registrados no DC (ca. 2,76–2,74 Ga) são principalmente representados pela formação do Complexo Luanga, da Suíte Intrusiva Cateté e do Diopsídio-Norito Pium (FERREIRA FILHO *et al.*, 2007; MACHADO *et al.*, 1991; SANTOS; GALARZA; OLIVEIRA, 2013).

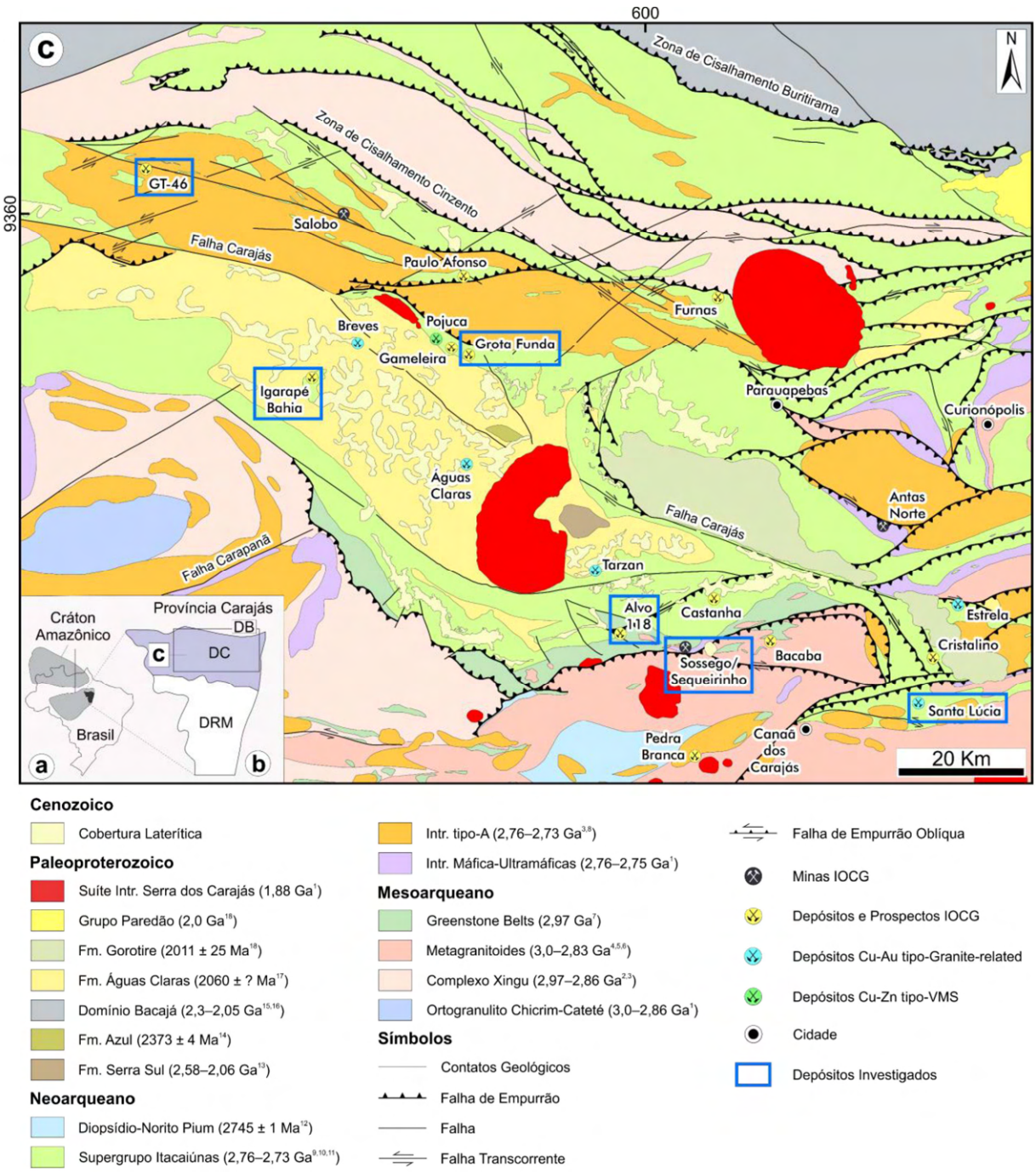

Figura 1. (a) Localização da Província Carajás (preto) na porção nordeste do Cráton Amazônico (cinza-claro), Brasil. (b) Segmentação da Província Carajás no Domínio Rio Maria (sul) e Domínio Carajás (norte), este separado do Domínio Bacajá pela Zona de Cisalhamento Buritirama. (c) Mapa geológico simplificado do Domínio Carajás, evidenciando

a distribuição espacial de importantes depósitos cupríferos e das minas de Cu atualmente em operação, juntamente com as principais estruturas regionais. As caixas azuis indicam a localização aproximada dos depósitos investigados (modificado de COSTA et al., 2016). Dados geocronológicos compilados de: 1–Pidgeon et al. (2000); 2–Machado et al. (1991); 3–Avelar et al. (1999); 4–Moreto et al. (2011); 5–Feio et al. (2013); 6–Marangoanha et al. (2019); 7–Moreto et al. (2015); 8–Feio et al. (2012); 9–Trendall et al. (1998); 10–Tallarico et al. (2005); 11–Martins et al. (2017); 12–Santos et al. (2013); 13–Araújo e Nogueira (2019); 14–Justo et al. (2018); 15–Macambira et al. (2009); 16–Vasquez et al. (2008a); 17–Mougeot et al. (1996); 18–Pereira et al. (2009). Abreviaturas: IOCG = óxido de ferro-cobre-ouro, VMS = sulfeto maciço vulcanogênico.

A formação da Bacia de Carajás têm sido associada tanto à condições intracratônicas (DOCEGEO, 1988; TAVARES *et al.*, 2018), como a ambientes relacionados a arcos magmáticos continentais (DARDENNE; FERREIRA FILHO; MEIRELLES, 1988; FIGUEIREDO E SILVA *et al.*, 2020). Segundo Pinheiro e Holdsworth (2000), a deformação transtensional e transpressional progressiva ao longo das zonas de cisalhamento regionais de direção E-W e ESE-NNW (e.g., Cinzento e Carajás, ao norte, e Canaã, ao sul) foi o principal fator responsável pela inversão da bacia e pela foliação E-W pervasiva registrada no DC.

4. GEOLOGIA LOCAL DOS DEPÓSITOS DE COBRE-OURO INVESTIGADOS

4.1. Depósito tipo granite-related Santa Lúcia

O depósito Santa Lúcia (5–14 Mt @ 1,4–2,0% Cu, 0,2–0,4 g/t Au; (OZ MINERALS, 2019) está situado no Cinturão Sul do Cobre do DC e é hospedado por uma rocha riolítica subvulcânica correlacionada ao Grupo Grão Pará (**Fig. 2a–b**). Um corpo pegmatítico intrusivo não mineralizado corta a rocha hospedeira subvulcânica, exibindo características macro- (e.g., megacristais boudinados) e microscópicas (e.g., estiramento de cristais) que sugerem uma colocação durante a transição entre regimes de deformação dúctil para rúptil. O sistema hidrotermal Santa Lúcia é marcado por um evento precoce de alteração com clorita, que é sobreposto por alteração potássica (K-feldspato) espacialmente restrita e greisenização. Ambos os estágios de alteração potássica e tipo greisen são interpretados como espacial- e geneticamente associados com a colocação do pegmatito na área do depósito. O minério de cobre-ouro está espacialmente associado a domínios greisenizados e é principalmente representado por brechas matriz suportadas ricas em calcopirita, com esfalerita e pirrotita. Fluorapatita e quartzo são os principais minerais de ganga encontrados nas zonas de minério do depósito, ocorrendo em paragênese com os sulfetos. Vênulas de sericita e hematita sobrepõem-se as zonas de alteração hidrotermal e de minério previamente formadas. Uma idade $^{207}Pb/^{206}Pb$ de 2688 ± 27 Ma (MSWD = 0,14) foi obtida através de análises *in-situ* de grãos de monazita hidrotermais associados a mineralização do depósito Santa Lúcia (HUNGER *et al.*, 2021).

4.2. Depósito IOCG Sossego

O depósito Sossego (98,3 Mt @ 0,69% Cu, 0,19 g/t Au; VALE, 2021) localiza-se ao longo da zona de cisalhamento regional WNW-ESE de Canaã, no Cinturão Sul do Cobre, e compreende dois corpos de minério principais denominados Sequeirinho e Sossego (**Fig. 3a**; MONTEIRO *et al.*, 2008a). O corpo Sequeirinho (**Fig. 3b**), que é responsável por 85% dos recursos gerais do depósito (MONTEIRO *et al.*, 2008a), é hospedado principalmente pelo Granito Mesoarqueano Sequeirinho (ca. 3,0 Ga; MORETO *et al.*, 2015) e, em menor grau, pelo metadacito Pista e um corpo intrusivo de gabronorito (ca. 2,97 Ga e 2,74 Ga, respectivamente; MORETO *et al.*, 2015). Todas as rochas hospedeiras foram submetidas a processos de alteração hidrotermal que incluem um estágio de alteração sódica regional e inicial (albita-hematita), seguido por alterações sódico-cálcicas (actinolita-albita-magnetita-apatita), potássica (biotita e K-feldspato) e clorítica (clorita-epidoto-allanita) (MONTEIRO *et al.*, 2008a; MORETO *et al.*, 2015). Corpos brechados com mergulho acentuado concentram a

maior parte da mineralização de cobre-ouro, que está associada a uma assembleia cálcica rica em epidoto. Nas brechas mineralizadas, fragmentos ricos em magnetita-actinolita-apatita constituem o conjunto mineral mais antigo, que é envolvido por uma matriz contendo calcopirita, pirita, siegenita, millerita, cassiterita, esfalerita e ouro (MONTEIRO *et al.*, 2008a). Uma idade U-Pb em monazita de 2712 ± 4,7 Ma é interpretada como o momento de formação da mineralização IOCG para o corpo de minério Sequeirinho (MORETO *et al.*, 2015).

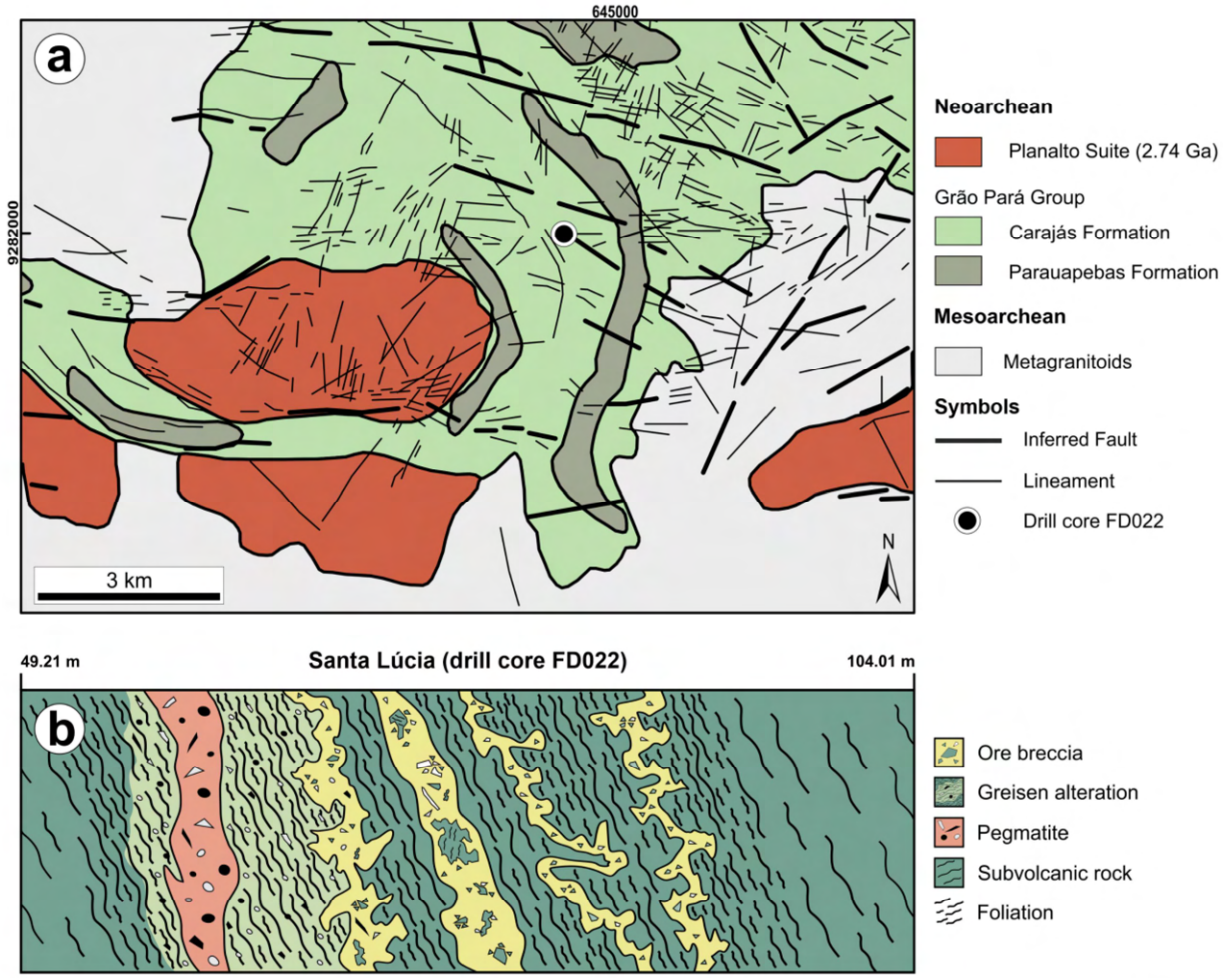

Figura 2. (a) Mapa geológico simplificado e (b) representação esquemática da distribuição das rochas hospedeiras e zonas de alteração hidrotermal e mineralizadas do depósito Santa Lúcia.

O corpo de minério Sossego (**Fig. 3c**) localiza-se a nordeste do corpo Sequeirinho e é principalmente hospedada por uma intrusão de granito granofírico Neoarqueano (ca. 2,74 Ga; MORETO *et al.*, 2015). A sequência de estágios de alteração hidrotermal no depósito é semelhante à observada no Sequeirinho, abrangendo associações de alteração sódica precoces (albita-calcita) e sódico-cálcica (actinolita-albita-magnetita-apatita), sobrepostas por

assembleias de alteração potássica e clorítica relativamente mais expressivas (MONTEIRO *et al*., 2008a). Corpos de brecha subverticais representam o principal estilo de mineralização de cobre-ouro, que é caracterizado principalmente por uma paragênese rica em calcopirita-pirita-quartzo-carbonato-apatita. Um estágio tardio de alteração hidrolítica (sericita-hematita-quartzo-clorita-calcita), predominantemente desenvolvido sob condições rúpteis, juntamente com a evidência de preenchimento de espaço aberto nas brechas, indicam que o corpo Sossego define um seguimento estruturalmente mais raso do sistema hidrotermal do depósito Sossego (MONTEIRO *et al.,* 2008a). A datação U-Pb *in situ* de cristais de monazita produziu uma idade de 1879 ± 4,1 Ma para o corpo de minério Sossego (MORETO *et al*., 2015).

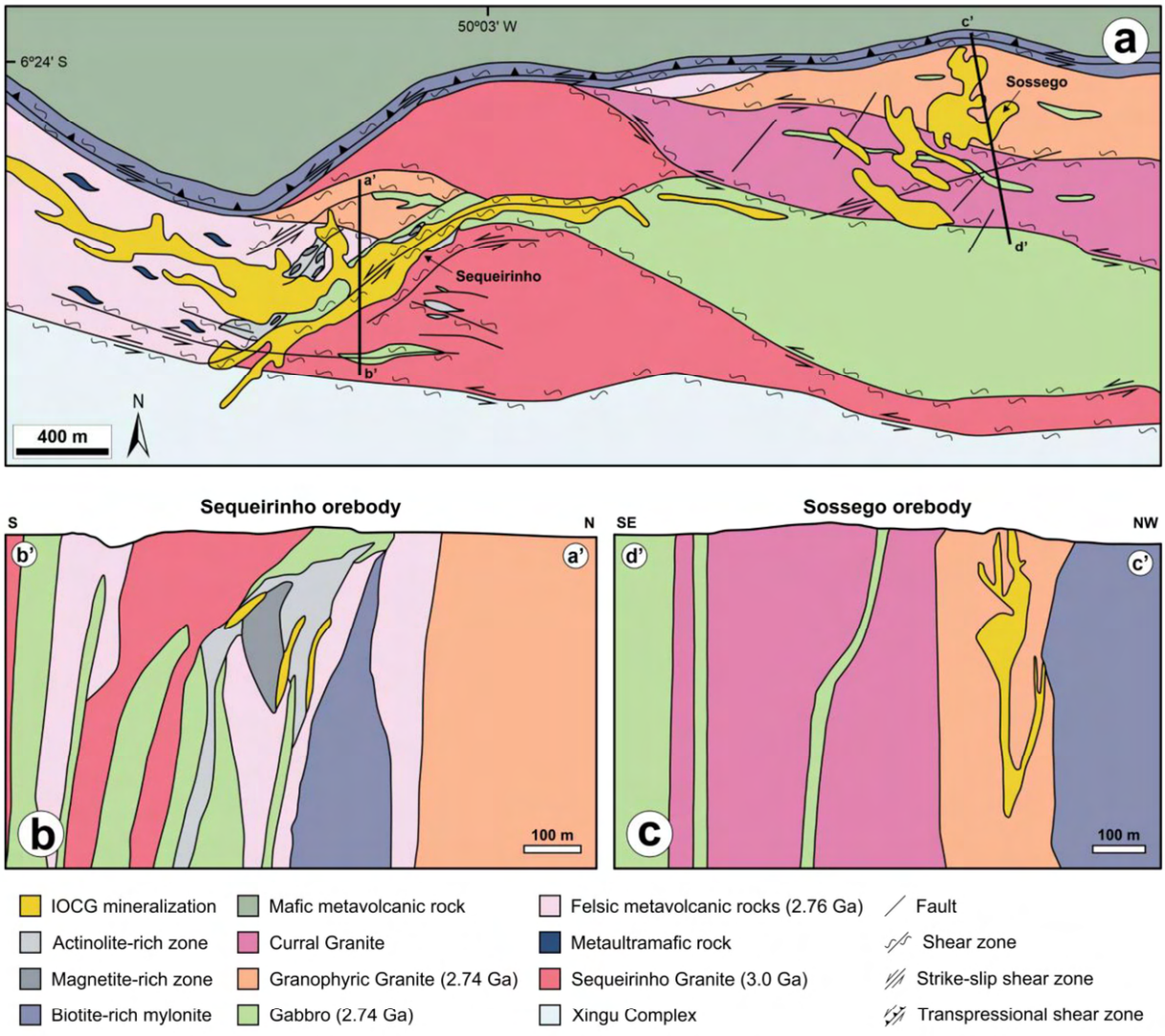

Figura 3. (a) Mapa geológico da região sul do DC, indicando a localização dos corpos de minério Sequeirinho e Sossego. (b) Perfis geológicos dos corpos Sequeirinho e (c) Sossego (modificado de MORETO et al., 2015).

4.3. Depósito IOCG GT-46

O depósito GT-46, também conhecido como Igarapé Cinzento, está inserido na zona de cisalhamento Cinzento de direção WNW-ESE, que define uma grande descontinuidade regional que também acomoda os depósitos IOCG Salobo, Paulo Afonso e Furnas IOCG, na porção norte do DC. Localmente, o depósito situa-se nos flancos sub-verticais de uma estrutura em dobra que afeta os anfibolitos hospedeiros (2774 ± 19 Ma, U-Pb em zircão) e rochas xistosas, bem como formações ferríferas bandadas metamorfoseadas do Grupo Grão Pará (Fig. 3a; SILVA *et al.*, 2005; TOLEDO *et al.*, 2019). Um evento tectono-metamórfico regional entre 2,77 e 2,72 Ga é interpretado como a principal causa para a foliação Sn observada nas rochas anfibolíticas hospedeiras, cujo conjunto mineral (i.e., hornblenda + plagioclásio + diopsídio + apatita) indica um metamorfismo de fácies anfibolito superior. A deformação heterogênea ocorrida durante o desenvolvimento da zona de cisalhamento Cinzento em ca. 2,72 Ga gerou uma foliação Sn+1 que transpõe a Sn previamente estabelecida. Rochas intrusivas cortam a sequência metavolcano-sedimentar do depósito e incluem um tonalito foliado (2560 ± 3,2 Ma), granodiorito, pegmatito (2562 ± 39 Ma, U-Pb em zircão; 2449 ± 44 Ma, Re-Os em molibdenita), granito indeformado (2564 ± 3,6 Ma) e diques de diabásio (TOLEDO *et al.*, 2019).

Assembleias de alteração sódico-cálcicas e potássicas expressivas, juntamente com um intenso metassomatismo ferrífero, representam a sequência de alteração precoce que precedeu o primeiro estágio de mineralização disseminada com calcopirita-bornita-magnetita no depósito (mineralização I; **Fig. 3b**). Veios mineralizados e corpos de brecha com magnetita maciça e calcopirita (mineralização II) sobrepõem zonas alteração hidrotermal previamente formadas, porém são cortados por halos de cloritização diretamente associados à colocação dos granitóides (TOLEDO *et al.*, 2019). Segundo Toledo *et al.* (2019), a circulação de fluidos hidrotermais dentro da zona de cisalhamento Cinzento foi responsável pelo desenvolvimento do primeiro estágio de mineralização no depósito GT-46 (2718 ± 56 Ma, Re-Os em molibdenita). Assim, um evento de formação de minério hidrotermal sobreposto entre ca. 2,72 e 2,5 Ga teria desencadeado a formação da mineralização II.

4.4. Depósito IOCG Grota Funda

O depósito Grota Funda (15–40 Mt @ 0,8–1,2% Cu; HUNGER *et al.*, 2018), no setor norte do DC, está localizado no sistema de falha Pojuca de direção WNW-ESSE, juntamente com os depósitos polimetálicos Pojuca e Gameleira. O depósito é hospedado principalmente por rochas ígneas máficas (basalto e diabásio) atribuídas ao Grupo Igarapé

Pojuca e, em menor extensão, por uma unidade gabroica, BIF, e uma rocha subvulcânica félsica (Fig. 3c-d). As rochas hospedeiras máficas foram intensamente afetadas por estágios de alteração hidrotermal sódico-cálcica, férrica, potássica e com clorita-quartzo-turmalina. Três estágios de mineralização de cobre foram identificados no depósito Grota Funda, incluindo corpos maciços de magnetita-calcopirita (I), minério brechado de calcopirita-magnetita-pirrotita-esfalerita (II) e zonas maciças de calcopirita-clorita-quartzo (III). Estes eventos foram respectivamente associados aos estágios de enriquecimento em Fe e de alteração potássica e clorítica. Associados a brecha mineralizada (mineralização II), apatita, quartzo e turmalina representam os principais minerais de ganga, ocorrendo circundados por calcopirita maciça. Veios de quartzo-carbonato com texturas de preenchimento de espaço aberto cortam todas as rochas hospedeiras do depósito, bem como zonas de alteração hidrotermal pretéritas. Uma idade Re-Os modelo em molibdenita de 2530 ± 60 Ma (σ) é atualmente interpretada como o momento de formação da mineralização I no depósito Grota Funda (HUNGER *et al.*, 2018).

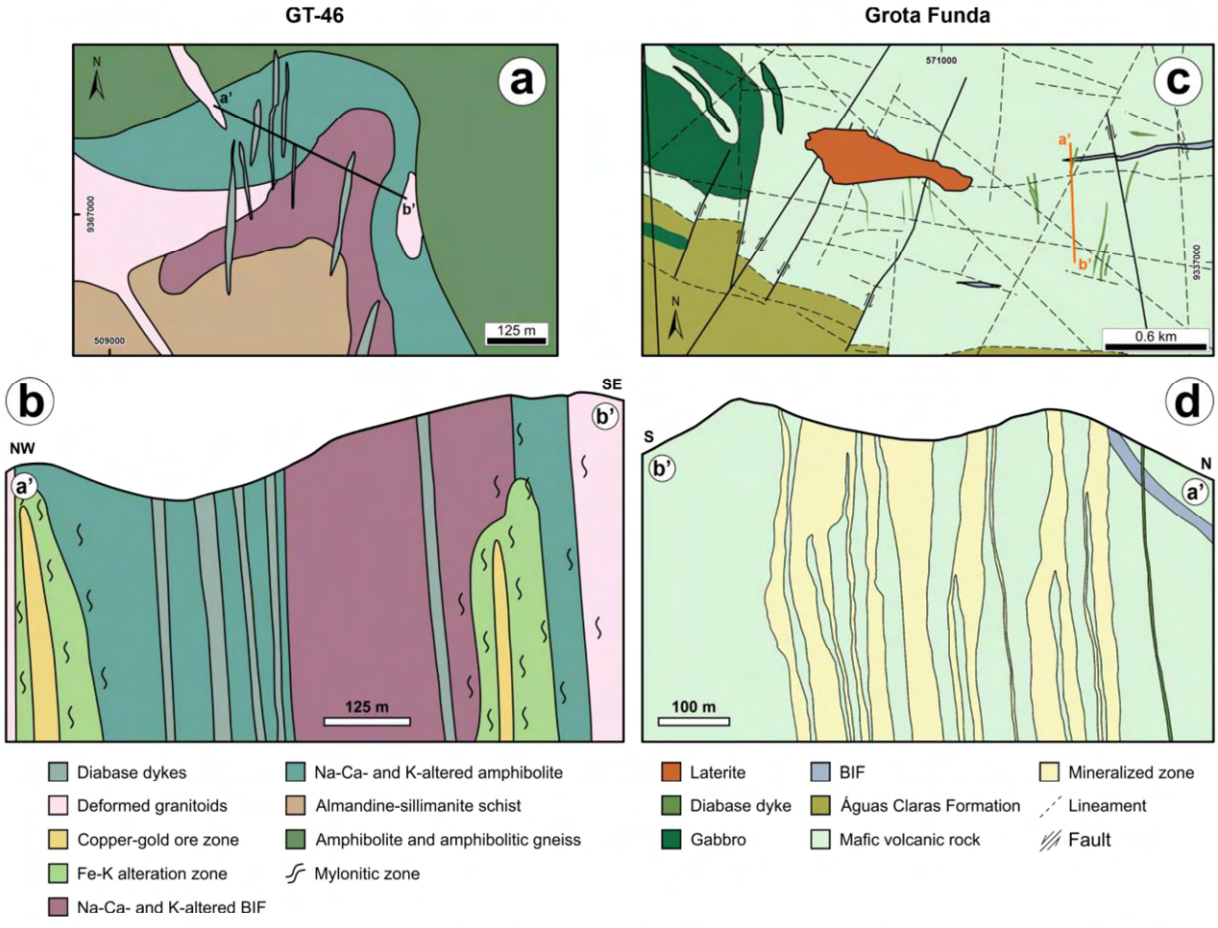

Figura 4. (a) Mapa geológico simplificado e (b) perfil geológico NW-SE do depósito GT-46, mostrando as principais rochas hospedeiras, zonas de alteração hidrotermal e corpos

mineralizados (modificado de TOLEDO *et al.*, 2019). (c) Mapa geológico e (d) perfil geológico S-N do depósito Grota Funda (modificado de HUNGER *et al.*, 2018). Abreviações: BIF = formação ferrífera bandada.

4.5. Depósito IOCG Igarapé Bahia/Alemão

O depósito Igarapé Bahia/Alemão (219 Mt @ 1,4% Cu, 0,86 g/t Au; TALLARICO *et al.*, 2005) está localizado no setor norte do DC, próximo à zona de cisalhamento Carajás em e inserido em uma janela erosiva através das rochas metassedimentares da Formação Águas Claras (FAC; MELO *et al.*, 2019). O depósito consiste em quatro corpos de minério distintos denominados Alemão, Acampamento Norte, Acampamento Sul e Furo 30 (**Fig. 5**), coletivamente hospedados pelas rochas metavulcanossedimentares do Grupo Igarapé Bahia e uma metagrauvaca da FAC (DREHER *et al.*, 2008; MELO *et al.*, 2019; TALLARICO *et al.*, 2005). Estudos anteriores descreveram o depósito de Igarapé Bahia como um minério tipo *stringer* formado no final do Arqueano ao Paleoproterozoico (FERREIRA FILHO, 1985), que foi posteriormente interpretado como uma mineralização singenética de cobre-ouro relacionada a um sistema vulcano-exalativo análogo ao tipo Besshi (ALMADA; VILLAS, 1999; DREHER *et al.*, 2008; VILLAS; SANTOS, 2001). Por outro lado, uma associação com depósitos da classe IOCG e, portanto, uma origem epigenética para a mineralização cobre-ouro no depósito Igarapé Bahia, foi inicialmente proposta por (Huhn e Nascimento (1997) e posteriormente endossada por Tazava e Oliveira (2000) e Tallarico *et al.* (2005).

Mais recentemente, Melo *et al.* (2019) sugeriram que os nódulos e camadas de calcopirita encontrados na sequência metassedimentar superior (ca. 2,76–2,73 Ga) do Grupo Igarapé Bahia representariam uma mineralização primária e singenética de cobre no depósito, possivelmente formada por processos exalativos semelhantes aos descritos em sistemas tipo VHMS. Esta mineralização primária teria sido sobreposta por um sistema mineralizante IOCG em ca. 2,55–2,57 Ga (MELO *et al.*, 2019; TALLARICO *et al.*, 2005), por sua vez associado à deformação dúctil e brechamento hidrotermal. O sistema hidrotermal IOCG é caracterizado por uma evolução paragenética que começou com uma alteração cálcico-sódica distal e espacialmente restrita, seguida por estágios de alteração potássica-(férrica), carbonática-(magnetita) e com clorita. A mineralização de cobre-ouro é semelhante para todos os corpos de minério e principalmente confinada a zonas miloníticas e brechas hidrotermais. Uma característica marcante desses corpos de minério é a abundância de fosfatos, incluindo apatita, queralita e autunita, bem como tungstatos como scheelita e wolframita. Veios tardios

de quartzo-carbonato-calcopirita cortam todas as zonas de alteração hidrotermal e os corpos de minério (MELO *et al.*, 2019).

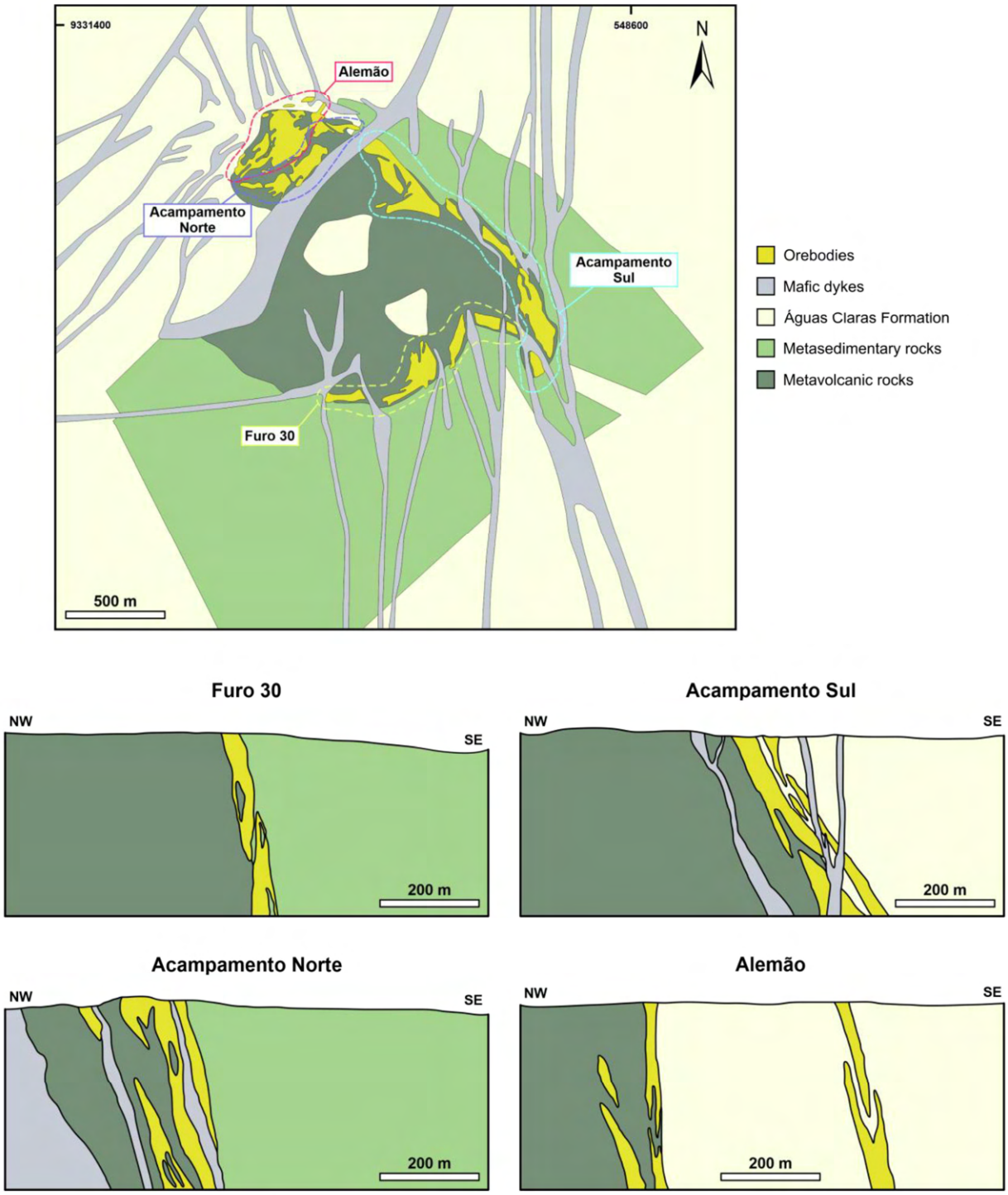

Figura 5. Mapa geológico da área do depósito Igarapé Bahia/Alemão, mostrando as regiões aproximadas referentes aos corpos de minério Furo 30, Acampamento Sul, Acampamento Norte e Alemão (curvas coloridas pontilhadas). As respectivas seções geológicas para cada um dos corpos de minério estão evidenciadas abaixo (modificado de MELO *et al.*, 2019).

4.6. Depósito IOCG Alvo 118

O depósito Alvo 118 (170 Mt @ 1,0% Cu, 0,3 g/t Au; RIGON *et al.*, 2000) está situado a aproximadamente 12 km a oeste do depósito Sossego, adjacente ao contato entre o embasamento Mesoarqueano e as unidades metavolcanosedimentares do Supergrupo Itacaiúnas (ca. 2,76 Ga). Dentro da zona de cisalhamento Canaã, o depósito compreende dois corpos de minério tabulares e subverticais principais denominados Principal Trend e Trend 2, que são primariamente hospedados por rochas máficas a metavulcânicas intermediárias associadas ao Grupo Grão Pará e, em menor extensão, por granito, gabro e intrusões de diques de quartzo porfirítico (**Fig. 6**; RIGON *et al.*, 2000; TALLARICO, 2003; TORRESI *et al.*, 2012). As idades de cristalização do granito (2743 ± 3 Ma) e dos diques porfiríticos (2654 ± 9 Ma) foram estimadas pela datação SHRIMP II ^{207}Pb-^{206}Pb em zircão (TALLARICO, 2003). Com exceção dos diques, todos os litotipos foram intensamente afetados por alteração hidrotermal estruturalmente controlada, por sua vez marcada por uma foliação milonítica penetrante e caracterizada pela seguinte sequência zonal: (i) alteração sódica distal e pouco desenvolvida com escapolita e albita; (ii) alteração potássica com desenvolvimento de biotita nas rochas metavulcânicas máficas e gabro, ou substituição de plagioclásio por K-feldspato nas rochas hospedeiras félsicas. Neste caso a alteração está geralmente associada à silicificação e formação de magnetita; (iii) alteração clorítica pervasiva, representada por halos proximais ao redor dos corpos de minério de cobre-ouro ou uma rede complexa de veios transversais nas rochas hospedeiras e; (iv) alteração com quartzo-sericita e veios de calcita-fluorita (TORRESI *et al.*, 2012).

A mineralização de cobre-ouro em ambos os corpos de minério do depósito é caracterizada principalmente por brechas matriz suportadas ricas em calcopirita (até 60% vol.), além de veios *stockwork* desenvolvidos em regime de deformação rúptil. A assembleia de minério consiste em calcopirita, hematita, bornita, magnetita e pirita subordinada, que ocorrem em associação com calcita, quartzo, clorita e apatita (TORRESI *et al.*, 2012). Idades U-Pb (SHRIMP II) de 1869 ± 7 Ma e 1868 ± 7 Ma, obtidas através da datação de xenotima associada a mineralização maciça e venular, respectivamente, restringem a época de formação das mineralizações do depósito Alvo 118 ao Paleoproterozoico (TALLARICO, 2003).

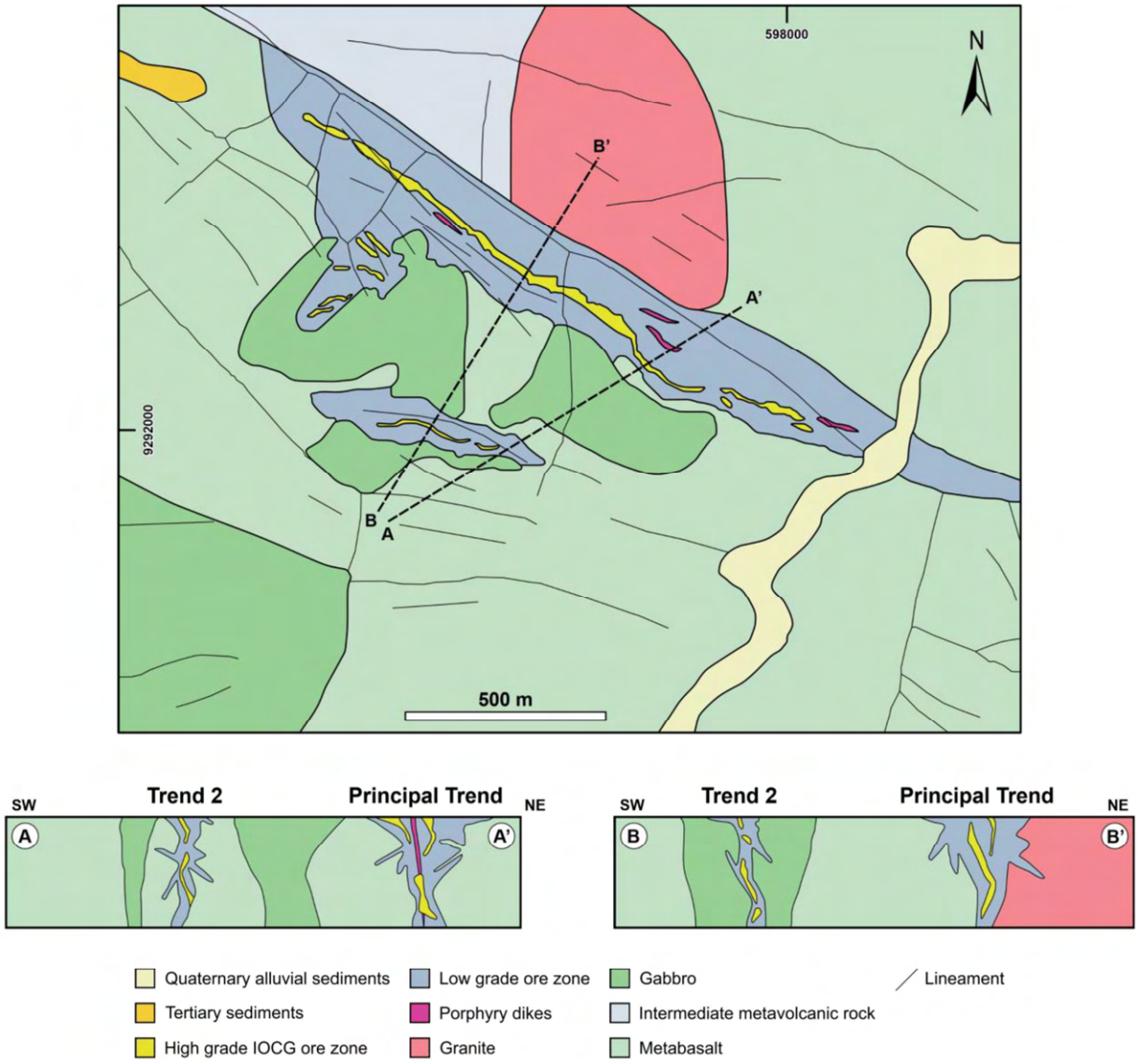

Figura 6. Mapa geológico simplificado e perfis geológicos do depósito IOCG Alvo 118, demonstrando a geometria dos corpos de minério Trend Principal e Trend 2 (modificado de TORRESI et al., 2012).

5. MATERIAIS E MÉTODOS

5.1. Seleção de Amostras e Petrografia

Estudos petrográficos detalhados de lâminas delgadas contendo apatita dos depósitos de cobre-ouro Santa Lúcia (amostra SL-22/76,1), Sequeirinho (amostras SEQ-99/291,2 e SEQ-99/304), GT-46 (amostra IC-44/340,1), Grota Funda (amostra GR-39/339,7), Igarapé Bahia (amostra IB-332/235,7), Sossego (amostra SOS-315/235,4) e Alvo 118 (amostra ALV-443/196,3) foram inicialmente realizados para o estabelecimento de relações paragenéticas. Um sumário descritivo com as formas de ocorrência da apatita em cada um dos depósitos investigados é mostrado na **Tabela 1**. Grãos de apatita representativos foram então investigados através de imagens BSE e CL usando um microscópio eletrônico de varredura (MEV) modelo LEO 430i (*Zeiss Company*), equipado com um detector CL *Gatan Chroma*, para determinar domínios texturais complexos. As imagens do CL foram adquiridas sob uma voltagem de aceleração de 15 kV, distância de trabalho de 16 mm e corrente de ablação entre 6 e 10 nA. Inclusões e sobrecrescimentos em apatita foram identificadas usando um sistema de espectroscopia de raios-X por dispersão de energia (EDS) acoplado ao mesmo equipamento MEV. Todas essas etapas analíticas foram executadas no Instituto de Geociências da Universidade Estadual de Campinas (UNICAMP), Brasil.

5.2. Análises de Microssonda Eletrônica

As análises de EPMA foram realizadas em um instrumento JEOL JXA-8230 no Laboratório de Microscopia e Microanálises (LMic) da Universidade Federal de Ouro Preto (UFOP), Brasil. Análises pontuais quantitativas ao longo de transectos em linha foram feitas usando o modo de dispersão de comprimento de onda, operado com uma voltagem de aceleração de 20 kV e corrente e diâmetro do feixe de 40 nA e 5 nm, respectivamente. Os seguintes padrões, linhas de raios-X e cristais foram usados para todas as análises de EPMA, exceto para as amostras SOS-315/235,4 e SEQ-99/291,2 em que a fluorapatita foi substituída por calcita para efetuar a calibração do Ca: anortoclásio, NaKα, TAPH; CaF_2, FKα, TAPH; quartzo, SiKα, TAP; anortita, AlKα, TAP; olivina, MgKα, TAP; $BaSO_4$, BaLα, PETH; fluorapatita, CaKα e PKα, PETH; magnetita, FeKα, LIFH; escapolita (meionita), ClKα, PETH; pirita, SKα, PETH; rutilo, TiKα, PETL; microclínio, KKα, PETL; Mn, MnKα, LIFL; $NdPO_4$, NdLβ, LIFL; $PrPO_4$, PrLβ, LIFL; $CePO_4$, CeLα, LIFL; $LaPO_4$, LaLα, LIFL; estroncianita, SrLα, PETL. Os tempos de contagem de pico e de fundo foram de 10 e 5 s para cada um dos elementos analisados, respectivamente. Para mitigar os efeitos da migração durante as análises, F e Na foram invariavelmente medidos no primeiro ciclo.

Tabela 1 Modos de ocorrência da apatita por amostra e depósito

Idade do Depósito (Ba)	Nome do Depósito	Amostra	Modo de ocorrência da apatita	Referências
2,72–2,68	Santa Lúcia	SL-22/76,1	Associada à brecha mineralizada, ocorrendo em paragênese com calcopirita, esfalerita e pirrotita.	Hunger et al. (2021)
	Sequeirinho	SEQ-99/291,2	Intercrescida com magnetita maciça e actinolita em zonas de alteração sódico-cálcicas.	Monteiro et al. (2008a)
		SEQ-99/304	Juntamente com actinolita e magnetita, constitui parte da matriz em zona de brecha sulfetada, representando a assembleia mineral mais jovem.	Monteiro et al. (2008a)
	GT-46	IC-44/340,1	Espacialmente associada a domínios deformados ricos em hornblenda, em protólito supostamente máfico (anfibolito?).	Este estudo; Toledo et al. (2019)
2,57–2,53	Grota Funda	GR-39/339,7	Associada à brecha mineralizada e envolta por uma matriz dominantemente composta por calcopirita e magnetita.	Hunger et al. (2018)
	Igarapé-Bahia	IB-332/235,7	Fase mineral de ganga associada ao corpo de minério brechado com calcopirita-pirita-magnetita.	Melo et al. (2019); Tallarico et al. (2005)
1,90–1,88	Sossego	SOS-315/235,4	Parageneticamente associada com actinolita e magnetita em zonas de alteração sódico-cálcicas.	Monteiro et al. (2008a)
	Alvo 118	ALV-443/196,3	Espacialmente associada com a mineralização de cobre-ouro, embora cortada por calcopirita.	Torresi et al. (2012)

A fórmula estrutural da apatita foi calculada com base em 25 átomos de oxigênio e assumindo que o sítio aniônico monovalente se comportou de forma ideal, de acordo com a "Abordagem 2" de Ketcham (2015). No entanto, é importante ressaltar que, considerando as orientações cristalográficas aleatórias dos grãos de apatita analisados, além das condições de operação escolhidas para este estudo, que são diferentes daquelas consideradas ótimas para medições de halogênios (F e Cl; GOLDOFF; WEBSTER; HARLOV, 2012), acredita-se que os teores de flúor tenham sido superestimados em resposta a um aumento significativo em suas contagens de raios-X. De fato, valores de flúor superiores à concentração máxima teórica estabelecida para a fluorapatita pura (3,77% em peso; PTÁČEK, 2016) predominam nos grãos da maioria dos depósitos estudados. Da mesma forma, uma diminuição nas contagens de raios-X de Cl e uma consequente subestimação de seus valores verdadeiros não podem ser completamente descartadas, especialmente para análises orientadas paralelamente ao eixo c da apatita (GOLDOFF; WEBSTER; HARLOV, 2012). Como resultado dessas imprecisões, os teores de OH determinados estequiometricamente (ou seja, OH = 2 - F - Cl) muitas vezes

produziram valores negativos, sendo então considerados abaixo do limite de detecção. Valores totais corrigidos abaixo de 97,5 wt% foram descartados dos dados.

5.3. Análises de LA-ICP-MS

Anteriormente as análises de LA-ICP-MS, grãos de apatita representativos foram imageados por catodoluminescência microscópica óptica (OM-CL) no *State Key Laboratory of Geological Processes and Mineral Resources* (GPMR), *China University of Geosciences* (Wuhan), usando um microscópio LEICA DM 2700P acoplado a um sistema CITL8200 MK-5. Essas imagens adicionais de CL foram obtidas com um tempo de exposição de 6 s, utilizando um sistema de câmera Leica. As condições operacionais incluíram uma voltagem de aceleração de 10 kV e uma corrente de feixe de 250 μA.

As análises de elementos traços foram realizadas nas instalações da Nanjing FocuMS Technology Co. Ltd, utilizando um sistema de ablação a laser Cetac Excite 193nm acoplado a um ICP-MS Agilent 7700x. A descrição detalhada dos procedimentos analíticos e redução de dados é relatada em Gao *et al.* (2013). As condições operacionais envolveram um feixe de 40 μm de diâmetro e uma taxa de repetição de 7 Hz, com tempo de contagem de 12 e 48 s para aquisição de dados de fundo e amostrais, respectivamente. As concentrações elementares foram calibradas utilizando como base inúmeros materiais de referência, incluindo NIST 610, NIST 612, BIR-1G, BCR-2G, BHVO-2G, GSE-1G, CGSG-1, CGSG-2, CGSG-4 e CGSG-5. Para corrigir o desvio de sensibilidade dependente do tempo e a discriminação de massa, a cada seis ou sete análises de amostras de apatita foi efetuada uma análise do padrão NIST 610 de forma subsequente. A redução de dados *offline*, incluindo a integração e seleção de sinais de fundo e de análise, correção de desvio de tempo e calibração quantitativa, foi realizada usando o software ICPMSDataCal (LIU *et al.*, 2008).

Análises adicionais foram executadas usando um sistema de ablação a laser modelo 213 Nd:YAG (CETAC UP-213 nm) acoplado a um ICP-MS de setor magnético ThermoFisher Element II, no *Applied Isotope Research Lab*, UFOP. Cada análise foi realizada empregando um tamanho de *spot* de 40 μm, uma taxa de repetição de 6 Hz e uma fluência de 6 J/cm^2, considerando 20 s de aquisição de fundo, seguido de 60 s de ablação da amostra. Com base em dados de EPMA obtidos previamente, concentrações médias de CaO entre 53–54,5 wt% foram adotadas como padrões internos para fins de calibração. O vidro NIST612 foi utilizado como principal material de calibração, juntamente com os vidros BHVO e BCR (valores de referência seguiram os de JOCHUM *et al.*, 2016), para garantir o controle de qualidade das análises. Para todos os elementos com concentrações acima de 10

ppm, a precisão relativa (RSD %) referente à múltiplas análises dos padrões de controle de qualidade indicou um desvio melhor do que 20% em relação aos valores de referência. As contagens brutas foram processadas *offline* e seguidas pela redução dos dados e cálculos de concentração utilizando o software Glitter (GRIFFIN *et al.*, 2008).

5.4. Geocronologia U-Pb em LA-ICP-MS

Os dados de geocronologia U/Pb *in-situ* foram adquiridos no mesmo instrumento ICP-MS utilizado para as análises de elementos traços, porém operando no modo *time-resolved*, com transição de picos e contagem de pulso, considerando 25 s de medição de fundo, seguidos por 30 s de ablação da amostra. As análises foram realizadas empregando uma saída de energia nominal de 30%, taxa de repetição de 10 Hz, fluência do laser de ~3,5 J/cm2 e um tamanho de *spot* de 40 μm. Devido a complexidade microtextural dos grãos de apatita analisados, os *spots* analíticos não foram precisamente posicionados nos distintos domínios revelados pelas imagens de catodoluminescência. O *software* Glitter (VAN ACHTERBERG *et al.*, 2001) e um programa interno (Saturn; SILVA, 2020) foram utilizados para redução *offline* dos dados, enquanto os cálculos de idade foram efetuados através do IsoplotR (VERMEESCH, 2018). As idades das amostras calculadas correspondem ao intercepto inferior em um diagrama de Tera-Wasserburg e foram determinadas por meio de linhas de regressão não ancoradas. Análises múltiplas de materiais de referência, incluindo o zircão da Tanzânia (Tanz 1) e as apatitas Madagascar (MAD1 e MAD2; idades ID-TIMS de 486,58 ± 0,85 Ma e 474,25 ± 0,41 Ma, respectivamente; THOMSON *et al.*, 2012), 401 (idade LA-ICP-MS de 506,2 ± 8,1 Ma; THOMPSON *et al.*, 2016) e Sumé (idade ID-TIMS de 568 ± 1,0 Ma; LANA *et al.*, 2022) foram conduzidas para fins de controle de qualidade. Idades concordantes de 603,5 ± 2,3 Ma (MSWD = 1,5) e 599,6 ± 2,0 Ma (MSWD = 1,3) foram calculadas para o zircão Tanz 1 e estão de acordo, considerando a incerteza, com a idade de referência ID-TIMS de 601 ± 1,0 Ma (LANA *et al.*, 2022). As idades de intercepto inferior obtidas para as apatitas MAD1 (481,66 ± 7,84 Ma), MAD2 (469,07 ± 4,51 Ma), 401 (507,51 ± 1,53 Ma) e Sumé (571,67 ± 1,68 Ma) são consistentes com as determinadas por Thomson *et al*. (2012), Thompson *et al*. (2016) e Lana *et al*. (2022), respectivamente, considerando os erros analíticos.

6. DISCUSSÕES GERAIS

6.1. Artigo 1: Apatite cathodoluminescence and trace element geochemistry of Neoarchean and Paleoproterozoic Iron Oxide-Copper-Gold (IOCG) Deposits of the Carajás Domain, Brazil: Implications for fluid evolution and metallogenesis

(Em fase de submissão para a revista *Chemical Geology*)

Com o propósito de determinar possíveis mecanismos de mobilização de elementos traço em cristais de apatita associados a seis depósitos IOCG do DC (i.e., Sequeirinho, GT-46, Grota Funda, Igarapé Bahia/Alemão, Sossego e Alvo 118), bem como melhor compreender a evolução dos fluidos hidrotermais responsáveis pela gênese desses depósitos, realizamos a caracterização textural e química detalhada de amostras de apatita presentes em zonas de alteração hidrotermal e mineralizadas, através do imageamento por catodoluminescência e análises químicas por EPMA e LA-ICP-MS. Os resultados deste trabalho indicam que os cristais de apatita nestes depósitos são texturalmente complexos e demonstram significativas variações composicionais entre si, especialmente no que se refere aos conteúdos de ETR e alguns elementos de transição (e.g., Mn, Sr, Ba, Th, U).

A partir da utilização das concentrações de ETR, Sr e Y nos diferentes domínios dos cristais de apatita estudados, foi possível distinguir petrogeneticamente as amostras de acordo com a classificação proposta por O'Sullivan *et al.* (2020), esta posteriormente modificada por Li *et al.* (2022), que discrimina três categorias principais para a origem da apatita: magmática, metamórfica/granítica e hidrotermal. Em diagramas binários LREE vs. Sr/Y e $(La/Sm)_N$ vs. $(La/Yb)_N$, todas as amostras de apatita analisadas neste estudo mostram dominantemente uma assinatura hidrotermal compatível com mecanismos de dissolução-reprecipitação, exceto a amostra SOS-1 do corpo Sossego, cuja apatita indica ser de origem magmática.

No depósito Sequeirinho, a fluorapatita relacionada à mineralização (SEQ-2) é relativamente mais enriquecida em ETR + Y, apresentando também maiores proporções de Sr/Y, $(La/Yb)_N$ e $(La/Sm)_N$ em relação àquela associada às zonas de alteração Na-Ca (SEQ-1), que é opostamente mais enriquecida em OH em Cl. Portanto, propôs-se que a diminuição progressiva das concentrações de cloro no fluido hidrotermal responsável pela precipitação da hidroxiapatita SEQ-1 poderia ter sido desencadeada pela mistura com fluidos ricos em F durante o estágio de mineralização do depósito, levando, assim, à formação da fluorapatita SEQ-2. Para os depósitos GT-46 e Grota Funda, por outro lado, o evidente enriquecimento em ETR pesados (ETRP) demonstrado pelas fluorapatitas GT-yg e GR-2 provavelmente

estaria refletindo a remobilização hidrotermal de ETR leves (ETRL) dos domínios primários (apatitas GT-bl [?] e GR-1, respectivamente) e sua posterior reincorporação por sobrecrescimentos de allanita.

A fluorapatita hidrotermal do depósito Igarapé Bahia/Alemão, por sua vez, apresentou um padrão de fracionamento ETR + Y marcado por um claro enriquecimento de ETR intermediários (ETRI) e anomalias positivas de Eu. Considerando o fato de que a formação de zonas sericitizadas é particularmente inexpressiva no depósito e, consequentemente, a liberação de ETR a partir da alteração dos feldspatos presentes nas rochas hospedeiras é pouco provável, tal padrão de fracionamento poderia ter sido o resultado da cristalização da apatita a partir de fluidos hidrotermais alcalinas ricos em CO_2. De fato, dados geoquímicos e de inclusões fluidas indicam a participação de fluidos de baixa salinidade e contendo CO_2-CH_4 durante o evento mineralizante no depósito Igarapé Bahia/Alemão (DREHER *et al.*, 2008).

Para o depósito Sossego, as concentrações pronunciadas de ETRL (>37,000 ppm), combinadas com razões elevadas de $(La/Yb)_N$ (até 13,93), apontaram para uma origem magmática para a fluorapatita SOS-1, associada ao estágio de alteração Na-Ca. No depósito, o envolvimento de fluidos magmáticos durante o desenvolvimento das assembleias de alteração hidrotermal iniciais (i.e., sódica, sódica-cálcic, potássica) é relativamente ambígua, embora indicada por dados de isótopos de oxigênio (MONTEIRO et al. 2008a). De qualquer forma, a clara diminuição nos valores de ETRL e $(La/Yb)_N$ demonstradas pela apatita SOS-2 em relação à apatita SOS-1 poderia ser atribuída à mobilização de ETRL devido à alteração hidrotermal sobreposta (e.g., potássica), neste caso provavelmente associada a fluidos ricos em Cl, como sugerido pela química mineral e dados de inclusões fluidas (MONTEIRO *et al.*, 2008b).

As variedades de fluorapatita hidrotermal associadas a mineralização do depósito Alvo 118 (i.e., ALV-1 e ALV-2) exibiram um padrão de fracionamento ETR marcado por enriquecimento em ETRP. Este padrão poderia ser explicado pelo possível envolvimento de fluidos hidrotermais originalmente enriquecidos em ETRP controlando a precipitação de apatita durante a precipitação dos corpos mineralizados. De acordo com dados de inclusões fluidas para a brecha mineralizada do depósito Alvo 118, é sugerido que a interação de salmouras ricas em Cl com um fluido relativamente diluído e mais frio teria desencadeado a precipitação do minério, possivelmente contribuindo para a formação inicial da apatita (TORRESI *et al.*, 2012). Neste cenário, propõe-se que devido à estabilidade relativamente menor dos complexos de ETRP em relação àqueles com ETRL (BROOM-FENDLEY *et al.*,

2017), a sua desestabilização preferencial poderia ter causado a pronta incorporação de ETRP na apatita do depósito Alvo 118.

De forma geral, as variações dos conteúdos de ETR e outros elementos traço observadas para diferentes variedades de apatita em um mesmo depósito foram atribuídas a processos de dissolução-reprecipitação mediados pela ação de fluidos hidrotermais (HARLOV, 2015; MERCER *et al.*, 2020). Como consequência desses processos, domínios originais ricos em ETR que foram afetados pela frente de alteração hidrotermal dão lugar a setores reprecipitados relativamente empobrecidos nestes elementos (HARLOV *et al.*, 2005). Isto pôde ser claramente evidenciado através da comparação das imagens de catodoluminescência e dados de elementos traço entre as apatitas GR-1 e GR-2 do depósito Grota Funda, bem como entre as apatitas SOS-1 e SOS-2 do depósito Sossego. Além disso, os domínios empobrecidos em ETR são normalmente caracterizados por uma rede interconectada de poros nano- a micrométricos que facilitam a infiltração de fluidos através da apatita metassomatizada, auxiliando assim na lixiviação de ETR e outros elementos traço que podem ser facilmente incorporados por fases secundárias (e.g., monazita, allanita; HARLOV *et al.*, 2005). De fato, inúmeras inclusões de monazita são observadas na apatita do depósito Sossego, sendo mais comumente associadas a sítios de nucleação em regiões empobrecidas em ETR presentes na apatita SOS-2. No caso do depósito Sequeirinho, por outro lado, as inclusões de monazita observadas estão aparentemente associadas a zonas excepcionalmente porosas dentro da apatita SEQ-1. Adicionalmente, a formação de sobrecrescimentos de allanita nas bordas das apatitas SEQ-2, GR-2 e GT-yg foi atribuída a desestabilização da monazita na presença de um fluido rico em F e Ca, nos dois primeiros casos, ou a reações envolvendo monazita e silicatos associados (e.g., hornblenda) no último caso.

Por fim, de acordo com as relações Ce/Ce* vs. Eu/Eu* e Ga vs. Eu/Eu* dos cristais de apatita investigados, condições moderadamente reduzidas aparentemente prevaleceram durante a cristalização das apatitas SEQ-1, GT-yg, GR-1 e SOS-1, enquanto uma mudança para condições moderadamente oxidantes provavelmente ocorreu durante a formação das apatitas SEQ-2, GR-2 e SOS-2. No depósito Alvo 118, por outro lado, a apatita ALV-1 supostamente precipitou em um ambiente moderadamente oxidantes enquanto a apatita ALV-2 possivelmente foi originada em condições dominantemente oxidantes. Estes resultados estão de acordo com a tendência geral mostrada por depósitos IOCG em escala mundial cuja mineralização é predominantemente constituída por assembleias ricas em calcopirita e magnetita, que são geralmente categorizados como sistemas Cu-Au de redox intermediário ou relativamente reduzidos (SKIRROW, 2022). Além disso, a perceptível

mudança para condições de fO_2 relativamente mais altas durante a precipitação das apatitas SEQ-2, GR-2, ALV-2 e SOS-2 foi atribuída a participação de fluidos relativamente oxidantes que, por sua vez, teriam sido responsáveis pela precipitação de assembleias hidrotermais tardias e ricas em hematita nos respectivos depósitos (MONTEIRO *et al*. 2008a; TORRESI *et al*. 2012). No caso do depósito Igarapé Bahia/Alemão, por outro lado, as elevadas razões Eu/Eu* demonstradas pela fluorapatita da mineralização não necessariamente estariam refletindo sua precipitação a partir de um fluido altamente oxidante, mas, ao invés disso, a pronta incorporação de Eu^{2+} na estrutura da apatita, apesar de sua preferência pelo Eu^{3+} (RAKOVAN *et al*., 2001).

6.2. Artigo 2: Superimposition of hydrothermal events in the granite-related Santa Lúcia Cu-Au deposit, Carajás Domain (Brazil): Insights from trace element geochemistry and U-Pb geochronology in apatite

(Em fase de submissão para a revista *Precambrian Research*)

O Cinturão Sul do Cobre (CSC), inserido na Província Carajás (Brasil), constitui um distrito mineral extraordinariamente fértil que abriga um número expressivo de depósitos de cobre, incluindo, entre outros, sistemas Cu-Au-(W-Bi-Sn) tipo *granite-related* (XAVIER *et al*., 2017; POLLARD *et al*., 2019). Em Carajás, depósitos associados a esta classe demonstram, de forma geral, baixa concentração ou ausência de óxidos de ferro, assembleias de alteração hidrotermal ricas em quartzo-muscovita (e.g., greisenização) e uma paragênese de minério relativamente reduzida e marcada por uma afinidade geoquímica para elementos granitófilos (e.g., W, Bi, Sn, Li) (TALLARICO *et al*., 2004; GRAINGER *et al*., 2008; POLLARD *et al*., 2019; HUNGER *et al*., 2021). Adicionalmente, os depósitos tipo *granite-related* em Carajás foram predominantemente formados durante o Paleoproterozoico (ca. 1,88 Ga; TALLARICO *et al*., 2004; GRAINGER *et al*., 2008), sendo cronocorrelatos ao extenso evento magmático tipo-A que originou vários *stocks* graníticos na província.

O depósito Santa Lúcia localiza-se na margem sudeste do CSC e constitui o único membro Neoarqueano (ca. 2,68 Ga; HUNGER *et al*., 2021) dos depósitos tipo *granite-related* conhecidos até o momento em Carajás. No entanto, sua evolução paragenética ainda é pouco compreendida no tempo, especialmente pois as características geológicas do depósito sugerem uma história evolutiva mais complexa e não necessariamente restrita ao Neoarqueano. Neste contexto, investigamos as variações composicionais e texturais de cristais de apatita associados a zona de minério do depósito Santa Lúcia, combinando-as com análises de

geocronologia U-Pb *in-situ*, visando melhor definir a história de sobreposição hidrotermal no depósito, com possíveis implicações para a metalogênese do CSC.

A partir da caracterização textural e química da apatita, foi possível realizar a discriminação de três gerações distintas de apatita (i.e., SL-1, SL-2 e SL-3) na zona mineralizada do depósito Santa Lúcia, com composições diferentes de elementos maiores e traço. De forma geral, a apatita SL-1 apresenta catodoluminescência amarronzada e as maiores concentrações de elementos traço e ETR, sendo comumente bordejada pelas variedades SL-2 e SL-3, por sua vez marcadas por catodoluminescência amarelo-esverdeada e esverdeada, respectivamente. Coletivamente, tais características texturais e composicionais indicam que a apatita SL-1 poderia, portanto, ser primária em origem.

Considerando as baixas razões $(La/Yb)_N$ e $(La/Sm)_N$ (<10) apresentadas pela apatita SL-1, sua cristalização estaria provavelmente associada a processos metassomáticos mediados por fluidos (BROOM-FENDLEY *et al.*, 2016; MERCER *et al.*, 2020; LU *et al.*, 2021). Adicionalmente, os conteúdos mais elevados de cloro somados aos valores relativamente baixos de $(Eu/Eu^*)_N$ (<0,4), sugerem que o fluido hidrotermal responsável pela precipitação da apatita SL-1 era presumivelmente rico em Cl e moderadamente reduzido. Assim, é razoável esperar que a interação da apatita SL-1 com fluidos enriquecidos em flúor durante eventos hidrotermais sobrepostos poderia ter contribuído para a precipitação das apatitas SL-2 e SL-3. Tal interação teria sido responsável por promover modificações texturais e químicas na apatita SL-1 que são comumente atribuídas a processos de dissolução-reprecipitação, por sua vez capazes de mobilizar componentes químicos de domínios originários da apatita, deixando os setores reprecipitados do cristal relativamente empobrecidos em certos elementos (e.g., ETR; HARLOV, 2015), como é o caso das apatitas SL-2 e SL-3. Neste caso, os ETRL lixiviados poderiam ter sido prontamente reincorporados por inclusões de monazita que ocorrem preferencialmente envoltas por ou como sobrecrescimentos na apatita SL-3.

A fluorapatita do depósito Santa Lúcia também registrou uma transição de assinaturas ligeiramente empobrecidas em ETRP nas apatitas SL-1 e SL-2, para um padrão marcadamente convexo e enriquecido em ETRI na apatita SL-3. Tal mudança nos padrões normalizados de ETR + Y foi atribuída principalmente a diminuição das condições de pH do fluido hidrotermal responsável pela precipitação da apatita SL-3. Esta diminuição é condizendo com a evolução hidrotermal do depósito Santa Lúcia, que indica a participação contínua de fluidos ácidos nos estágios finais de atividade metassomática (i.e., greisenização seguida pela precipitação da mineralização e formação de veios de sericita; HUNGER *et al.*,

2021). Além disso, vênulas de hematita controladas por fraturas representam o evento mais tardio de atividade hidrotermal reconhecido no depósito Santa Lúcia, indicando que o sistema hidrotermal também se tornou progressivamente mais oxidante no depósito.

Por fim, de acordo com as idades U-Pb obtidas neste estudo, pelo menos três eventos distintos em ca. 2,56 Ga, 2,1 Ga e 1,81 Ga foram registrados pela apatita da zona de minério brechado do depósito. Atualmente, os dados geocronológicos disponíveis para o depósito Santa Lúcia também incluem uma ddade $^{207}Pb/^{206}Pb$ de 2688 ± 27 Ma (MSWD = 0,14), obtida através de datação de cristais hidrotermais de monazita, que atualmente é interpretada como o momento da formação da mineralização do depósito (HUNGER *et al.*, 2021). Neste sentido, a idade de 2,56 Ga foi atribuída ao momento do resfriamento necessário para atingir a temperatura de fechamento para difusão de Pb na apatita, e não ao evento de cristalização da apatita SL-1 em si. As idades mais jovens de 2,1 Ga e 1,81 poderiam, portanto, estar associadas a novos eventos de formação de apatita metassomática (SL-2 e SL-3?) causado pela sobreposição de eventos hidrotermais Paleoproterozoicos.

7. CONCLUSÕES GERAIS

Com base nos resultados obtidos através da investigação química e textural de cristais apatita associados a zonas de alteração hidrotermal e mineralizadas de depósitos IOCG e tipo *granite-related* do DC, foi possível obter as seguintes conclusões:

a. As variações composicionais e morfológicas observadas entre as amostras de apatita investigadas neste estudo refletem a história da interação fluido-apatita e a evolução do sistema hidrotermal em cada depósito estudado. Os processos que controlaram a incorporação de ETR e outros elementos-traço na apatita, bem como sua remobilização interna (e.g., mecanismos de dissolução-reprecipitação), foram predominantemente regulados por atividade metassomática. Tal ativade estaria associada a regimes de fluidos distintos que operaram em escala de depósito, sem relação aparente com épocas metalogenéticas em específico (Neoarqueano vs. Paleoproterozoico).
b. Os valores de Eu/Eu*, Ce/Ce* e Ga sugerem que a apatita se formou sob condições distintas de fO_2 em Carajás, desde condições relativamente reduzidas (depósitos Sequeirinho, GT-46, Grota Funda e Sossego) até condições mais oxidadas (Alvo 118 e Igarapé Bahia/Alemão). Gerações de apatita de formação tardia (i.e., apatitas SEQ-2, GR-2, ALV-2 e SOS-2) refletem a interação progressiva de grãos de apatita primária com fluidos oxidantes nos estágios finais da atividade hidrotermal em alguns dos depósitos estudados.
c. Fases secundárias portadoras de ETR, como monazita e alanita, ocorrem associadas a domínios alterados hidrotermalmente dentro dos grãos de apatita da maioria dos depósitos investigados. Tais fases foram formadas como resultado de processos metassomáticos de dissolução-reprecipitação que promoveram a lixiviação significativa de ETRL das regiões primárias da apatita e sua subsequente reincorporação por minerais secundários ricos em ETR.
d. As variações composicionais observadas entre as diferentes gerações de apatita (Sl-1, Sl-2 e SL-3) associadas a zona mineralizada do depósito Santa Lúcia são provavelmente o resultado de intenso metassomatismo em um sistema hidrotermal que se tornou progressivamente mais ácido e oxidante com o tempo. Nesse sentido, a sobreposição de eventos metassomáticos no depósito foi registrada pela apatita e envolveu pelo menos três pulsos hidrotermais distintos, que ocorreram tanto no Neoarqueano (ca. 2,56 Ba) como no Paleoproterozoico (ca. 2,1 e 1,81 Ba).

REFERÊNCIAS BIBLIOGRÁFICAS

ALMADA, M. do C. O.; VILLAS, R. N. O depósito Bahia: um possível exemplo de depósito de sulfeto vulcanogênico tipo Besshi arqueano em Carajás. Revista Brasileira de Geociências, [s. l.], v. 29, n. 4, p. 579–592, 1999. Disponível em: https://doi.org/10.25249/0375-7536.199929579592.

ALMEIDA, J. A. C. et al. Origin of the Archean leucogranodiorite-granite suites: Evidence from the Rio Maria terrane and implications for granite magmatism in the Archean. Lithos, [s. l.], v. 120, n. 3–4, p. 235–257, 2010. Disponível em: http://dx.doi.org/10.1016/j.lithos.2010.07.026.

ALMEIDA, J. de A. C. de et al. Zircon geochronology, geochemistry and origin of the TTG suites of the Rio Maria granite-greenstone terrane: Implications for the growth of the Archean crust of the Carajás province, Brazil. Precambrian Research, [s. l.], v. 187, n. 1–2, p. 201–221, 2011.

ARAÚJO FILHO, R. C.; NOGUEIRA, A. C. R.; ARAÚJO, R. N. New stratigraphic proposal of a Paleoproterozoic siliciclastic succession: Implications for the evolution of the Carajás Basin, Amazonian craton, Brazil. Journal of South American Earth Sciences, [s. l.], v. 102, n. May, p. 102665, 2020. Disponível em: https://doi.org/10.1016/j.jsames.2020.102665.

ARAÚJO, R.; NOGUEIRA, A. Serra sul diamictite of the carajas basin (Brazil): A paleoproterozoic glaciation on the amazonian craton. Geology, [s. l.], v. 47, n. 12, p. 1166–1170, 2019.

AVELAR, V. G. et al. O magmatismo arqueano da região de Tucumã - Província Mineral De Carajás: Novos resultados geocronológicos. Revista Brasileira de Geociências, [s. l.], v. 29, n. 4, p. 453–460, 1999.

BARROS, C. E. M. et al. Dados isotópicos Pb-Pb em zircão (evaporação) e Sm-Nd do Complexo Granítico Estrela, Província Mineral de Carajás, Brasil: Implicações petrológicas e tectônicas. Revista Brasileira de Geociências, [s. l.], v. 34, n. 4, p. 531–538, 2004.

BARROS, C. E. M. et al. Structure, petrology, geochemistry and zircon U/Pb and Pb/Pb geochronology of the synkinematic archean (2.7 Ga) A-type granites from the Carajás Metallogenetic Province, northern Brazil. The Canadian Mineralogist, [s. l.], v. 47, p. 1423–1440, 2009.

BARTON, M. D. Iron Oxide(-Cu-Au-REE-P-Ag-U-Co) Systems. In: HOLLAND, H.; TURKIAN, K. (org.). Treatise on Geochemistry: Second Edition. [S. l.]: Elsevier Ltd., 2014. v. 13, p. 515–541. Disponível em: http://dx.doi.org/10.1016/B978-0-08-095975-7.01123-2.

BELOUSOVA, E. A. et al. Apatite as an indicator mineral for mineral exploration: Trace-element compositions and their relationship to host rock type. Journal of Geochemical Exploration, [s. l.], v. 76, n. 1, p. 45–69, 2002.

BOUZARI, F. et al. Hydrothermal Alteration Revealed by Apatite Luminescence and Chemistry: A Potential Indicator Mineral for Exploring Covered Porphyry Copper Deposits. Economic Geology, [s. l.], v. 11, p. 1397–1410, 2016.

BROOM-FENDLEY, S. et al. Evidence for dissolution-reprecipitation of apatite and preferential LREE mobility in carbonatite-derived late-stage hydrothermal processes. American Mineralogist, [s. l.], v. 101, n. 3, p. 596–611, 2016.

BROOM-FENDLEY, S. et al. REE minerals at the Songwe Hill carbonatite, Malawi: HREE-enrichment in late-stage apatite. Ore Geology Reviews, v. 81, p. 23–41, 2017. Disponível em: https://doi.org/10.1016/j.oregeorev.2016.10.019

CAO, M. et al. Major and trace element characteristics of apatites in granitoids from central Kazakhstan: Implications for petrogenesis and mineralization. Resource Geology, [s. l.], v. 62, n. 1, p. 63–83, 2012.

COCHRANE, R. et al. High temperature (>350°C) thermochronology and mechanisms of Pb loss in apatite. Geochimica et Cosmochimica Acta, [s. l.], v. 127, p. 39–56, 2014.

COLE, D. R.; CHAKRABORTY, S. Rates and mechanisms of isotopic exchange. Reviews in Mineralogy and Geochemistry, [s. l.], v. 43, p. 83–223, 2001.

CORDANI, U. G.; TEIXEIRA, W. Proterozoic accretionary belts in the Amazonian Craton. Memoir of the Geological Society of America, [s. l.], v. 200, p. 297–320, 2007.

DARDENNE, M. A.; FERREIRA FILHO, C. F.; MEIRELLES, M. R. The role of shoshonitic and calc-alkaline suites in the tectonic evolution of the Carajás District, Brazil. Journal of South American Earth Sciences, [s. l.], v. 1, n. 4, p. 363–372, 1988.

DECRÉE, S. et al. Unravelling the processes controlling apatite formation in the Phalaborwa Complex (South Africa) based on combined cathodoluminescence, LA-ICPMS and in-situ O and Sr isotope analyses. [S. l.]: Springer Berlin Heidelberg, 2020-. ISSN 14320967.v. 175 Disponível em: https://doi.org/10.1007/s00410-020-1671-6.

DINIZ, A. C. et al. Unravelling magmatic-hydrothermal processes at Salobo and GT-46 IOCG deposits, Carajás mineral province, Brazil: Constraints from whole-rock geochemistry and trace elements in apatite. Journal of South American Earth Sciences, [s. l.], v. 125, n. September 2022, p. 104290, 2023. Disponível em: https://doi.org/10.1016/j.jsames.2023.104290.

DOCEGEO. Revisão litoestratigráfica da Província Mineral de Carajás - Litoestratigrafia e principais depósitos minerais. In: , 1988, Belém. XXXV Congresso Brasileiro de Geologia. Belém: SBG, 1988. p. 11–54.

DREHER, A. M. et al. New geologic, fluid inclusion and stable isotope studies on the controversial Igarapé Bahia Cu-Au deposit, Carajás Province, Brazil. Mineralium Deposita, [s. l.], v. 43, n. 2, p. 161–184, 2008.

FEIO, G. R. L. et al. Archean granitoid magmatism in the Canaã dos Carajás area: Implications for crustal evolution of the Carajás province, Amazonian craton, Brazil. Precambrian Research, [s. l.], v. 227, p. 157–185, 2013. Disponível em: http://dx.doi.org/10.1016/j.precamres.2012.04.007.

FEIO, G. R. L. et al. Geochemistry, geochronology, and origin of the Neoarchean Planalto Granite suite, Carajás, Amazonian craton: A-type or hydrated charnockitic granites?. Lithos, [s. l.], v. 151, p. 57–73, 2012. Disponível em: http://dx.doi.org/10.1016/j.lithos.2012.02.020.

FERREIRA FILHO, C. F. Geologia e Mineralizações Sulfetadas do Prospecto Bahia, Província Mineral de Carajás. 1985. - University of Brasilia, [s. l.], 1985.

FERREIRA FILHO, C. F. et al. Mineralizações estratiformes de PGE-Ni associadas a complexos acamadados em Carajás: os exemplos de Luanga e Serra da Onça. In: ROSA-COSTA, L. T.; KLEIN, E. L.; VIGLIO, E. P. (org.). Contribuições à geologia da Amazônia. v. 5ed. Belém: SBG-Núcleo Norte, 2007. p. 1–14.

FIGUEIREDO E SILVA, R. C. et al. Geotectonic signature and hydrothermal alteration of metabasalts under- and overlying the giant Serra Norte iron deposits, Carajás mineral Province. Ore Geology Reviews, [s. l.], v. 120, n. December 2019, 2020.

GAO, J.-F. et al. Sulfide Saturation and Magma Emplacement in the Formation of the Permian Huangshandong Ni-Cu Sulfide Deposit, Xinjiang, Northwestern China. Economic Geology, [s. l.], v. 108, p. 1833–1848, 2013.

GOLDOFF, B.; WEBSTER, J. D.; HARLOV, D. E. Characterization of fluor-chlorapatites by electron probe microanalysis with a focus on time-dependent intensity variation of halogens. American Mineralogist, [s. l.], v. 97, n. 7, p. 1103–1115, 2012.

GRAINGER, C. J. et al. Metallogenesis of the Carajás Mineral Province, Southern Amazon Craton, Brazil: Varying styles of Archean through Paleoproterozoic to Neoproterozoic base- and precious-metal mineralisation. Ore Geology Reviews, [s. l.], v. 33, n. 3–4, p. 451–489, 2008.

GRIFFIN, W. L. et al. Glitter: Data reduction software for laser ablation ICP-MS. In: SYLVESTER, P. (org.). Laser Ablation ICP-MS in the Earth Sciences: Current Practices and Outstanding Issues. Short Course Series, Volume 40. [S. l.]: Mineralogical Association of Canada, 2008. v. 40, p. 308–311.

HARLOV, D. E. Apatite: A fingerprint for metasomatic processes. Elements, [s. l.], v. 11, n. 3, p. 171–176, 2015.

HARLOV, D. E.; WIRTH, R.; FÖRSTER, H. J. An experimental study of dissolution-reprecipitation in fluorapatite: Fluid infiltration and the formation of monazite. Contributions to Mineralogy and Petrology, [s. l.], v. 150, n. 3, p. 268–286, 2005.

HUGHES, J. M.; RAKOVAN, J. F. Structurally robust, chemically diverse: Apatite and apatite supergroup minerals. Elements, [s. l.], v. 11, n. 3, p. 165–170, 2015.

HUHN, S. R. B.; MACAMBIRA, M. J. B.; DALL'AGNOL, R. Geologia e geocronologia Pb-Pb do Granito Alcalino Planalto, Região da Serra do Rabo, Carajás-PA. In: , 1999. VI Simpósio de Geologia da Amazônia. [S. l.]: SBG-Núcleo Norte, 1999. p. 463–466.

HUHN, S. R. B.; NASCIMENTO, J. A. S. São os depósitos cupríferos de Carajás do tipo Cu-Au-U-ETR?. In: COSTA, M. L.; ANGÉLICA, R. S. (org.). Contribuições à Geologia da Amazônia. 1. ed. Belém: SBG, 1997. p. 143–160.

HUNGER, R. B. et al. Hydrothermal Alteration, Fluid Evolution, and Re-Os Geochronology of the Grota Funda Iron Oxide Copper-Gold Deposit, Carajás Province (Pará State), Brazil. Economic Geology, [s. l.], v. 113, n. 8, p. 1769–1794, 2018.

HUNGER, R. B. et al. The Santa Lúcia Cu-Au deposit, Carajás Mineral Province, Brazil: a Neoarchean (2.68 Ga) member of the granite-related copper-gold systems of Carajás. Mineralium Deposita, [s. l.], 2021.

JOCHUM, K. P. et al. Reference Values Following ISO Guidelines for Frequently Requested Rock Reference Materials. Geostandards and Geoanalytical Research, [s. l.], v. 40, n. 3, p. 333–350, 2016.

JUSTO, A. P. et al. Detrital zircon populations in the Neoarchean to Paleoproterozoic sedimentary coverage of Carajás, Amazon Craton, Brazil. In: , 2018, Rio de Janeiro. 49o Congresso Brasileiro de Geologia. Rio de Janeiro: SBG, 2018. p. 1890.

KETCHAM, R. A. Technical Note: Calculation of stoichiometry from EMP data for apatite and other phases with mixing on monovalent anion sites. American Mineralogist, [s. l.], v. 100, n. 7, p. 1620–1623, 2015.

KIRKLAND, C. L. et al. Apatite: a U-Pb thermochronometer or geochronometer?. Lithos, [s. l.], v. 318–319, p. 143–157, 2018. Disponível em: https://doi.org/10.1016/j.lithos.2018.08.007.

LANA, C. et al. Assessing the U-Pb, Sm-Nd and Sr-Sr Isotopic Compositions of the Sumé Apatite as a Reference Material for LA-ICP-MS Analysis. Geostandards and Geoanalytical Research, [s. l.], v. 46, n. 1, p. 71–95, 2022.

LI, J., YE, C., YING, J. In Situ Geochemical and Sr-Nd Isotope Analyses of Apatite from the Shaxiongdong Alkaline-Carbonatite Complex (South Qinling, China): Implications for magma evolution and mantle source. Minerals v. 12, p. 1–19, 2022.

LIU, Y. et al. In situ analysis of major and trace elements of anhydrous minerals by LA-ICP-MS without applying an internal standard. Chemical Geology, [s. l.], v. 257, n. 1–2, p. 34–43, 2008. Disponível em: http://dx.doi.org/10.1016/j.chemgeo.2008.08.004.

LU, J. et al. Apatite texture and trace element chemistry of carbonatite-related REE deposits in China: Implications for petrogenesis. Lithos, [s. l.], v. 398–399, n. June, p. 106276, 2021. Disponível em: https://doi.org/10.1016/j.lithos.2021.106276.

MACAMBIRA, M. J. B. et al. Crustal growth of the central-eastern Paleoproterozoic domain, SW Amazonian craton: Juvenile accretion vs. reworking. Journal of South American Earth Sciences, [s. l.], v. 27, n. 4, p. 235–246, 2009. Disponível em: http://dx.doi.org/10.1016/j.jsames.2009.02.001.

MACHADO, N. et al. U-Pb geochronology of Archean magmatism and basement reactivation in the Carajás area, Amazon shield, Brazil. Precambrian Research, [s. l.], v. 49, n. 3–4, p. 329–354, 1991.

MAO, M. et al. Apatite trace element compositions: A robust new tool for mineral exploration. Economic Geology, [s. l.], v. 111, n. 5, p. 1187–1222, 2016.

MARANGOANHA, B.; OLIVEIRA, D. C. de; DALL'AGNOL, R. The Archean granulite-enderbite complex of the northern Carajás province, Amazonian craton (Brazil): Origin and implications for crustal growth and cratonization. Lithos, [s. l.], v. 350–351, p. 105275, 2019. Disponível em: https://doi.org/10.1016/j.lithos.2019.105275.

MARTINS, P. L. G. et al. Neoarchean magmatism in the southeastern Amazonian Craton, Brazil: Petrography, geochemistry and tectonic significance of basalts from the Carajás Basin. Precambrian Research, [s. l.], v. 302, n. May, p. 340–357, 2017.

MELO, G. H. C. et al. Evolution of the Igarapé Bahia Cu-Au deposit, Carajás Province (Brazil): Early syngenetic chalcopyrite overprinted by IOCG mineralization. Ore Geology Reviews, [s. l.], v. 111, p. 102993, 2019. Disponível em: https://doi.org/10.1016/j.oregeorev.2019.102993.

MELO, G. H. C. et al. Magmatic-hydrothermal fluids leaching older seafloor exhalative rocks to form the IOCG deposits of the Carajás Province, Brazil: Evidence from boron isotopes. Precambrian Research, [s. l.], v. 365, n. August, p. 106412, 2021. Disponível em: https://doi.org/10.1016/j.precamres.2021.106412.

MELO, G. H. C. et al. Temporal evolution of the giant Salobo IOCG deposit, Carajás Province (Brazil): Constraints from paragenesis of hydrothermal alteration and U-Pb

geochronology. Mineralium Deposita, [s. l.], v. 52, n. 5, p. 709–732, 2016. Disponível em: http://dx.doi.org/10.1007/s00126-016-0693-5.

MERCER, C. N.; WATTS, K. E.; GROSS, J. Apatite trace element geochemistry and cathodoluminescent textures—A comparison between regional magmatism and the Pea Ridge IOAREE and Boss IOCG deposits, southeastern Missouri iron metallogenic province, USA. Ore Geology Reviews, [s. l.], v. 116, n. January 2019, p. 103129, 2020. Disponível em: https://doi.org/10.1016/j.oregeorev.2019.103129.

MILES, A. J. et al. Apatite: A new redox proxy for silicic magmas?. Geochimica et Cosmochimica Acta, [s. l.], v. 132, p. 101–119, 2014. Disponível em: http://dx.doi.org/10.1016/j.gca.2014.01.040.

MONTEIRO, L. V. S. et al. Spatial and temporal zoning of hydrothermal alteration and mineralization in the Sossego iron oxide–copper–gold deposit, Carajás Mineral Province, Brazil: paragenesis and stable isotope constraints. Mineralium Deposita, [s. l.], v. 43, n. 2, p. 129–159, 2008a. Disponível em: http://link.springer.com/10.1007/s00126-006-0121-3.

MONTEIRO, L.V.S. et al. Mineral chemistry of ore and hydrothermal alteration at the Sossego iron oxide-copper-gold deposit, Carajás Mineral Province, Brazil. Ore Geology Reviews, v. 34, p. 317–336, 2008b. Disponível em: https://doi.org/10.1016/j.oregeorev.2008.01.003.

MORETO, C. P. N. et al. Mesoarchean (3.0 and 2.86 Ga) host rocks of the iron oxide-Cu-Au Bacaba deposit, Carajás Mineral Province: U-Pb geochronology and metallogenetic implications. Mineralium Deposita, [s. l.], v. 46, n. 7, p. 789–811, 2011.

MORETO, C. P. N. et al. Neoarchean and paleoproterozoic iron oxide-copper-gold events at the Sossego deposit, Carajás Province, Brazil: Re-Os and U-Pb geochronological evidence. Economic Geology, [s. l.], v. 110, n. 3, p. 809–835, 2015.

MORETO, C. P. N. et al. Timing of multiple hydrothermal events in the iron oxide–copper–gold deposits of the Southern Copper Belt, Carajás Province, Brazil. Mineralium Deposita, [s. l.], v. 50, n. 5, p. 517–546, 2015.

MOTTA, J. G. et al. Archean crust and metallogenic zones in the Amazonian Craton sensed by satellite gravity data. Scientific Reports, [s. l.], v. 9, n. 1, p. 1–10, 2019. Disponível em: http://dx.doi.org/10.1038/s41598-019-39171-9.

MOUGEOT, R. et al. Geochronological constraints for the age of the Águas Claras Formation (Carajás Province, Pará, Brazil). In: , 1996, Salvador. XXXIX Congresso Brasileiro de Geologia. Salvador: SBG, 1996. p. 579–581.

NATHWANI, C. L. et al. Multi-stage arc magma evolution recorded by apatite involcanic rocks. Geology, [s. l.], v. 48, n. 4, p. 323–327, 2020.

O'SULLIVAN, G. et al. The trace element composition of apatite and its application to detrital provenance studies. Earth-Science Reviews, [s. l.], v. 201, n. June 2019, p. 103044, 2020. Disponível em: https://doi.org/10.1016/j.earscirev.2019.103044.

OLIVEIRA, R. G. de et al. Levantamento aerogravimétrico Carajás - Contribuição a geotectônica e metalogenia da porção leste do Cráton Amazonas. In: , 2017, Belém. XV Simpósio de Geologia da Amazônia. Belém: SBG, 2017. p. 251–254.

OZ MINERALS. ASX Release - Carajás Hub strategy gains pace. [S. l.: s. n.], 2019. Disponível em: https://www.ozminerals.com/media/carajas-hub-strategy-gains-pace/. .

PAN, L. C. et al. Apatite trace element and halogen compositions as petrogenetic-metallogenic indicators: Examples from four granite plutons in the Sanjiang region, SW China. Lithos, [s. l.], v. 254–255, p. 118–130, 2016.

PAN, Y.; FLEET, M. E. Compositions of the apatite-group minerals: Substitution mechanisms and controlling factors. Reviews in Mineralogy and Geochemistry, [s. l.], v. 48, p. 13–50, 2002.

PEREIRA, R. M. P. et al. Unidade Caninana: sequência clástica Paleoproterozóica revelada por datação U-Pb em zircões detríticos da Província Mineral Carajás. In: , 2009, Manaus. XI Simpósio de Geologia da Amazônia. Manaus: SBG, 2009. p. 376–379.

PICCOLI, P. M.; CANDELA, P. A. Apatite in igneous systems. Reviews in Mineralogy and Geochemistry, [s. l.], v. 48, n. 1, p. 255–292, 2002.

PIDGEON, R. T.; MACAMBIRA, M. J. B.; LAFON, J. M. Th-U-Pb isotopic systems and internal structures of complex zircons from an enderbite from the Pium Complex, Carajás Province, Brazil: Evidence for the ages of granulite facies metamorphism and the protolith of the enderbite. Chemical Geology, [s. l.], v. 166, n. 1–2, p. 159–171, 2000.

PINHEIRO, R. V. L.; HOLDSWORTH, R. E. Evolução tectonoestratigráfica dos sistemas transcorrentes Carajás e Cinzento, Cinturão Itacaiúnas, na borda leste do Cráton Amazônico,Pará. Revista Brasileira de Geociências, [s. l.], v. 30, n. 4, p. 597–606, 2000.

POLLARD, P. J. et al. 40Ar-39Ar dating of Archean iron oxide Cu-Au and Paleoproterozoic granite-related Cu-Au deposits in the Carajás Mineral Province, Brazil: implications for genetic models. Mineralium Deposita, [s. l.], v. 54, n. 3, p. 329–346, 2019.

PREVIATO, M. et al. Evolution of brines and CO2-rich fluids and hydrothermal overprinting in the genesis of the Borrachudo copper deposit, Carajás Province. Ore Geology Reviews, [s. l.], v. 121, n. July 2019, p. 103561, 2020. Disponível em: https://doi.org/10.1016/j.oregeorev.2020.103561.

PTÁČEK, P. Introduction to Apatites. In: APATITES AND THEIR SYNTHETIC ANALOGUES - SYNTHESIS, STRUCTURE, PROPERTIES AND APPLICATIONS. [S. l.: s. n.], 2016. v. 5, p. 1–60.

RAKOVAN, J., NEWVILLE, M., SUTTON, S. Evidence of heterovalent europium in zoned llallgua apatite using wavelength dispersive XANES. American Mineralogist, v. 86, p. 697–700, 2001. Disponível em: https://doi.org/10.2138/am-2001-5-610.

RIGON, J. C. et al. Alvo 118 copper-gold deposit: Geology and mineralization, Serra dos Carajás, Pará, Brazil. In: , 2000, Rio de Janeiro. 31th International Geological Congress. Rio de Janeiro: [s. n.], 2000. p. [CD-ROM].

SALGADO, S. S. et al. Provenance of the Buritirama Formation reveals the Paleoproterozoic assembly of the Bacajá and Carajás blocks (Amazon Craton) and the chronocorrelation of Mn-deposits in the Transamazonian/Birimian system of northern Brazil/West Africa. Journal of South American Earth Sciences, [s. l.], v. 96, n. September, p. 102364, 2019. Disponível em: https://doi.org/10.1016/j.jsames.2019.102364.

SANTOS, R. D. dos; GALARZA, M. A.; OLIVEIRA, D. C. De. Geologia, geoquímica e geocronologia do Diopsídio-Norito Pium, Província Carajás. Boletim do Museu Paraense Emílio Goeldi - Série Ciências Naturais, [s. l.], v. 8, n. April 2017, p. 355–382, 2013.

SARDINHA, A. S.; BARROS, C. E. M.; KRYMSKY, R. Geology, geochemistry, and U-Pb geochronology of the Archean (2.74 Ga) Serra do Rabo granite stocks, Carajás Metallogenetic Province, northern Brazil. Journal of South American Earth Sciences, [s. l.], v. 20, n. 4, p. 327–339, 2006.

SHA, L. K.; CHAPPELL, B. W. Apatite chemical composition, determined by electron microprobe and laser-ablation inductively coupled plasma mass spectrometry, as a probe into granite petrogenesis. Geochimica et Cosmochimica Acta, [s. l.], v. 63, n. 22, p. 3861–3881, 1999.

SIEPIERSKI, L.; FERREIRA FILHO, C. F. Spinifex-textured komatiites in the south border of the Carajas ridge, Selva Greenstone belt, Carajás Province, Brazil. Journal of South American Earth Sciences, [s. l.], v. 66, p. 41–55, 2016. Disponível em: http://dx.doi.org/10.1016/j.jsames.2015.12.011.

SILVA, M. G. et al. Geologia e mineralizações de Fe-Cu-Au do Alvo GT46 (Igarapé Cinzento), Carajás. In: MARINI, O. J.; QUEIROZ, E. T.; RAMOS, B. W. (org.). Caracterização de depósitos minerais em distritos mineiros da Amazônia. Brasília: DNPM/CT-Mineral/ADIMB, 2005. p. 94–151.

SILVA, J. P. A. Saturn – Uma nova ferramenta de correção de dados U-Pb para LA-ICP-MS. 2020. 79 f. - Federal University of Ouro Preto, [s. l.], 2020.

SKIRROW, R. G. Iron oxide copper-gold (IOCG) deposits – A review (part 1): Settings, mineralogy, ore geochemistry and classification. Ore Geology Reviews, [s. l.], v. 140, n. December 2021, p. 104569, 2022. Disponível em: https://doi.org/10.1016/j.oregeorev.2021.104569.

SOUZA, S. R. B.; MACAMBIRA, M. J. B.; SHELLER, T. Novos dados geocronológicos para os granitos deformados do Rio Itacaiúnas (Serra dos Carajás, PΛ): implicações estratigráficas. In: , 1996, Belém. V Simpósio de Geologia da Amazônia. Belém: SBG, 1996. p. 380–383.

TALLARICO, F. H. B. et al. Geological and SHRIMP II U-Pb constraints on the age and origin of the Breves Cu-Au-(W-Bi-Sn) deposit, Carajás, Brazil. Mineralium Deposita, [s. l.], v. 39, n. 1, p. 68–86, 2004.

TALLARICO, F. H. B. et al. Geology and SHRIMP U-Pb geochronology of the Igarapé Bahia deposit, Carajás copper-gold belt, Brazil: An Archean (2.57 Ga) example of Iron-Oxide Cu-Au-(U-REE) mineralization. Economic Geology, [s. l.], v. 100, n. 1, p. 7–28, 2005.

TALLARICO, F. H. B. O cinturão cupro-aurífero de Carajás, Brasil. 2003. 229 f. - Universidade Estadual de Campinas, [s. l.], 2003.

TASSINARI, C. C. G.; MACAMBIRA, M. J. B. Geochronological provinces of the Amazonian Craton. Episodes, [s. l.], v. 22, n. 3, p. 174–182, 1999. Disponível em: papers2://publication/uuid/6E450BB6-FA41-4C83-9140-D6B6891E16B8.

TAVARES, F. M. et al. The multistage tectonic evolution of the northeastern Carajás Province, Amazonian Craton, Brazil: Revealing complex structural patterns. Journal of South American Earth Sciences, [s. l.], v. 88, p. 238–252, 2018. Disponível em: https://doi.org/10.1016/j.jsames.2018.08.024.

TΛZΛVΛ, E.; OLIVEIRΛ, C. G. de. The Igarapé Bahia Λu-Cu-(REE-U) deposit, Carajás Mineral Province, northern Brazil. In: PORTER, T. M. (org.). Hydrothermal Iron Oxide

Copper-Gold & Related Deposits: A Global Perspective, Volume 1. Adelaide: PGC Publishing, 2000. p. 203–212.

THOMPSON, J. et al. Matrix effects in Pb/U measurements during LA-ICP-MS analysis of the mineral apatite. Journal of Analytical Atomic Spectrometry, [s. l.], v. 31, n. 6, p. 1206–1215, 2016.

THOMSON, S. N. et al. Routine low-damage apatite U-Pb dating using laser ablation-multicollector-ICPMS. Geochemistry, Geophysics, Geosystems, [s. l.], v. 13, n. 1, 2012.

TOLEDO, P. I. de F. et al. Multistage Evolution of the Neoarchean (ca. 2.7 Ga) Igarapé Cinzento (GT-46) Iron Oxide Copper-Gold Deposit, Cinzento Shear Zone, Carajás Province, Brazil. Economic Geology, [s. l.], v. 114, n. 1, p. 1–34, 2019.

TORRESI, I. et al. Hydrothermal alteration, fluid inclusions and stable isotope systematics of the Alvo 118 iron oxide-copper-gold deposit, Carajás Mineral Province (Brazil): Implications for ore genesis. Mineralium Deposita, [s. l.], v. 47, n. 3, p. 299–323, 2012.

TRENDALL, A. F. et al. SHRIMP zircon U-Pb constraints on the age of the Carajás formation, Grão Pará Group, Amazon Craton. Journal of South American Earth Sciences, [s. l.], v. 11, n. 3, p. 265–277, 1998.

VALE. Form 20-F. [S. l.: s. n.], 2021. Disponível em: http://www.vale.com/EN/investors/information-market/annual-reports/20f/Pages/default.aspx.

VAN ACHTERBERG, E. et al. Data reduction software for LA-ICP-MS. Laser Ablation ICP-MS in the Earth Sciences, [s. l.], v. 29, p. 239–243, 2001.

VASQUEZ, M. L. et al. Geologia e Recursos Minerais do Estado do Pará: Sistema de Informações Geográficas - SIG: texto explicativo dos mapas Geológico e Tectônico e de Recursos Minerais do Estado do Pará. Escala 1:1.000.000. Belém: CPRM, 2008.

VASQUEZ, M. L.; MACAMBIRA, M. J. B.; ARMSTRONG, R. A. Zircon geochronology of granitoids from the western Bacajá domain, southeastern Amazonian craton, Brazil: Neoarchean to Orosirian evolution. Precambrian Research, [s. l.], v. 161, n. 3–4, p. 279–302, 2008.

VERMEESCH, P. IsoplotR: A free and open toolbox for geochronology. Geoscience Frontiers, [s. l.], v. 9, n. 5, p. 1479–1493, 2018. Disponível em: https://doi.org/10.1016/j.gsf.2018.04.001.

VILLAS, R. N.; SANTOS, M. D. Gold deposits of the Carajás mineral province: Deposit types and metallogenesis. Mineralium Deposita, [s. l.], v. 36, n. 3–4, p. 300–331, 2001.

WIRTH, K. R.; GIBBS, A. K.; OLSZEWSKI JR., W. J. U-Pb ages of zircons from the Grão-Pará Group and Serra dos Carajás Granites, Pará, Brazil. Revista Brasileira de Geociências, [s. l.], v. 16, n. 2, p. 195–200, 1986.

XAVIER, R. P. et al. Comparing Iron Oxide Copper-Gold systems of the Carajás Mineral Province (Brazil) using apatite and magnetite trace elements: implications on genesis and exploration. In: , 2011. 11th SGA Biennial Meeting. [S. l.: s. n.], 2011. p. 461–463.

XAVIER, R. P. et al. Geology and Metallogeny of Neoarchean and Paleoproterozoic Copper Systems of the Carajás Domain, Amazonian Craton, Brazil. In: , 2017, Quebéc. 14th SGA Biennial Meeting. Quebéc: SGA, 2017. p. 899–902.

XAVIER, R. P. et al. The iron oxide copper-gold systems of the Carajás mineral province. Economic Geology, [s. l.], v. 16, n. Special Publication, p. 433–454, 2012.

ZIRNER, A. L. K. et al. Rare earth elements in apatite as a monitor of magmatic and metasomatic processes: The Ilímaussaq complex, South Greenland. Lithos, [s. l.], 2015. Disponível em: http://dx.doi.org/10.1016/j.lithos.2015.04.013.

ANEXO A: Apatite cathodoluminescence and trace element geochemistry of Neoarchean and Paleoproterozoic Iron Oxide-Copper-Gold (IOCG) Deposits of the Carajás Domain, Brazil: Implications for fluid evolution and metallogenesis

Raphael B. Hunger [a,*], Carolina P. N. Moreto [a], Roberto P. Xavier [a], Gláucia N. Queiroga [b], Cristiano de C. Lana [b], Wang Liao [c], Xin-Fu Zhao [c], Gustavo H. C. de Melo [b], Poliana I. de F. Toledo [d]

[a] Institute of Geosciences, University of Campinas, 250 Carlos Gomes, Campinas, São Paulo 13083-855, Brazil

[b] Department of Geology - Morro do Cruzeiro Campus, Federal University of Ouro Preto, Nove Street, Ouro Preto 35400-000, Brazil

[c] State Key Laboratory of Geological Processes and Mineral Resources, and Faculty of Earth Resources, China University of Geosciences, 388 Lumo Road, Wuhan 430074, China

[d] Department of Geology, Federal University of Rio Grande do Norte, s/n Engenharias Street, Natal 59078-970, Brazil

* Corresponding author: raphael.hunger@gmail.com; ORCID ID: 0000-0003-3712-8406

Abstract

The Meso- to Neoarchean (3.0–2.55 Ga) Carajás Domain, in the southeastern portion of the Amazonian Craton, contains a remarkable number of iron-oxide copper gold deposits formed at distinct metallogenic epochs that span from the Neoarchean (ca. 2.7 and 2.5 Ga) to the Paleoproterozoic (ca. 1.88 Ga). Apatite is a ubiquitous accessory mineral in these deposits, generally occurring associated with early sodic-calcic alteration assemblages or in paragenesis with sulfide-rich ore zones. Based on *in-situ* LA-ICP-MS and EPMA data of apatite, combined with cathodoluminescence imaging, we investigate morphological and compositional variations among samples from six IOCG deposits of the Carajás Domain, including the Sequeirinho, GT-46, Grota Funda, and Igarapé Bahia deposits, and the Paleoproterozoic Sossego and Alvo 118 deposits. The results of this study demonstrate that apatite grains in these systems are texturally complex and normally exhibit different domains under cathodoluminescence imaging, which are marked by distinctive trace element compositions and rare earth element (REE) patterns. Such compositional and morphological variations are here interpreted to reflect the history of fluid-apatite interaction at a deposit scale, which involved distinct fluid regimes that had no specific connection with metallogenic

epochs in particular (Neoarchean vs. Paleoproterozoic). Dissolution-reprecipitation processes mediated by metasomatic activity were, therefore, the main responsible for REE internal remobilization within apatite and the precipitation of secondary REE-bearing phases (e.g., monazite, allanite, xenotime) associated with altered domains in the analysed grains. Lastly, redox conditions operating during the course of hydrothermal processes that affected apatite in the studied deposits vary from relatively reduced (Sequeirinho, GT-46, Grota Funda, and Sossego) to more oxidized states (Alvo 118 and Igarapé Bahia/Alemão).

Keywords: Carajás Domain; Iron-oxide copper gold deposits; Apatite; Cathodoluminescence; Fluid evolution.

1. Introduction

The copper metallogeny of the Carajás Domain (CD), an Archean segment of the Carajás Province in the southeastern margin of the Brazilian Amazonian Craton (**Fig. 1a**), is considerably complex, counting with multiple ore-forming events in time. These events were the main causes that led to the formation of an ample variety of copper deposits in the CD, including, among others, world-class iron oxide-copper-gold (IOCG) systems (Xavier et al., 2017, 2012). The timing of IOCG formation at Carajás has been assigned to at least three major hydrothermal-mineralizing episodes (Hunger et al., 2018; Melo et al., 2016; Moreto et al., 2015b, 2015a; Toledo et al., 2019; Xavier et al., 2017) that took place in a broad time interval between the early Neoarchean (ca. 2.72–2.68 Ga and ca. 2.57 Ga) and the Paleoproterozoic (ca. 1.90–1.87 Ga). However, recent studies have demonstrated that the evolution of these IOCG deposits in the CD is not necessarily restrict to one of these major metallogenic epochs, but, instead, would have involved numerous hydrothermal pulses that caused, among other things, the overprint of alteration assemblages, metal input and remobilization, and the superposition of ages even at a deposit scale (Melo et al., 2021; Moreto et al., 2015b, 2015a; Previato et al., 2020; Toledo et al., 2019). In this sense, comprehending how these deposits evolved on a timescale has been proven to be a challenging task at Carajás, making it necessary the use of new approaches to better constrain the hydrothermal processes that led to their formation in the CD.

Trace element compositions of apatite have been largely utilized as a robust tool to track magmatic-hydrothermal processes in a variety of ore systems (Bouzari et al., 2016; Harlov, 2015; Mao et al., 2016; Mercer et al., 2020). Indeed, apatite is one of the most common accessory phosphates in igneous rocks (Piccoli and Candela, 2002) and a ubiquitous mineral phase in either hydrothermally altered or mineralized zones of several ore deposits

worldwide (Barton, 2014; Broom-Fendley et al., 2016; Decrée et al., 2020; Jia et al., 2020; Skirrow, 2022). Due to its capacity to structurally incorporate a significant amount of elements, including halogens (F and Cl), REE, and other important transition metals (Hughes and Rakovan, 2015; Pan and Fleet, 2002), apatite has been broadly used as a proxy for oxygen fugacity (fO_2) in magmatic systems (Cao et al., 2012; Miles et al., 2014), a detrital tracer for provenance studies (O'Sullivan et al., 2020), and a powerful petrogenic-metallogenic indicator (Belousova et al., 2002; Mao et al., 2016; Nathwani et al., 2020; Pan et al., 2016; Sha and Chappell, 1999).

Although relatively resistant to weathering and efficiently closed to isotopic diffusion below 550 °C (Cole and Chakraborty, 2001), apatite is particularly sensitive to fluid-induced, dissolution-reprecipitation processes, which are generally fingerprinted by compositional and textural/morphological changes (Harlov, 2015; Harlov et al., 2005). Through these changes, apatite is capable of recording crucial information about metasomatic overprints that are normally responsible for producing zoning patterns in crystals, which, in turn, could indicate multiple stages of apatite growth in time (Bouzari et al., 2016; Zirner et al., 2015). Thus, the integrated use of chemical information and textural evidence, the latter usually accessed by cathodoluminescence (CL) or back-scattered electron (BSE) imaging, allows apatite to serve as an excellent tool to investigate the geochemical history of complex magmatic-hydrothermal systems (Bouzari et al., 2016; Decrée et al., 2020; Lu et al., 2021; Mercer et al., 2020).

At Carajás, apatite represents an important accessory mineral that is typically identified within sulfide-rich ore zones or as a component of early sodic-calcic alteration assemblages in the IOCG deposits (Hunger et al., 2021; Monteiro et al., 2008a; Xavier et al., 2012). Despite its common occurrence, however, previous studies using apatite to trace magmatic-hydrothermal processes in these deposits are still scarce an essentially concentrated in a few study cases (Diniz et al., 2023; Xavier et al., 2011). In this sense, this study combines CL imaging with *in-situ* laser ablation inductively coupled plasma mass spectrometry (LA-ICP-MS) and electron microprobe (EPMA) data to investigate morphological and compositional variations among apatite from six IOCG deposits of the CD, formed at distinct metallogenic epochs and contrasting geological contexts. The purpose of this work is to: i) determine possible mechanisms of hydrothermal trace element mobilization and overprinting linked to apatite formation, aiming to better constrain the fluid evolution in these IOCG deposits; and (ii) identify geochemical contrasts and similarities among the studied deposits, which could have potential implications for the metallogenesis of the CD.

2. Regional geologic setting of the Carajás Domain

The CD (**Fig. 1b–c**), in the northern portion of the Carajás Province, is limited to the south by the Rio Maria Domain (RMD) and, to the north, by the Bacajá Domain (BD). The RMD constitutes a Mesoarchean (3.0–2.86 Ga; Almeida et al., 2010) granite-greenstone terrane composed of tonalite-trondhjemite-granodiorite (TTG) granitoids, sanukitoids, potassic leucogranites, and metavolcano-sedimentary sequences (Almeida et al., 2011), whereas the BD consists dominantly of Paleoproterozoic granitoids (2.3–2.05 Ga; Macambira et al., 2009; Vasquez et al., 2008a). According to Motta et al. (2019), the Carajás and Bacajá domains share a close and protracted evolution prior to the Transamazonian Orogeny (2.26–1.86 Ga; Cordani and Teixeira, 2007; Tassinari and Macambira, 1999; Vasquez et al., 2008b), which involved a similar Archean crust, although modified lithospheric settings when compared to the deeper lithosphere that resides under the RMD, whose crustal evolution was relatively stable and older. An inferred suture zone (Buritirama Shear Zone; Costa et al., 2016) separates the CD from the Bacajá block and is partially composed of platform depositional sequences of the Buritirama Formation (Oliveira et al., 2017; Salgado et al., 2019). Conversely, the approximate limit between the Carajás and Rio Maria domains is defined by a geophysically constrained, E-W lineament (Feio et al., 2013; Motta et al., 2019).

Migmatitic orthogneisses of the Xingu Complex (2.97–2.86 Ga; Avelar et al., 1999; Machado et al., 1991), the Chicrim-Cateté Orthogranulite (3.0–2.86 Ga; Pidgeon et al., 2000), and greenstone belt sequences (ca. 2.97 Ga; Moreto et al., 2015b; Siepierski and Ferreira Filho, 2016) comprise the main Mesoarchean basement rocks of the CD. Additionally, a distinct set of metagranitoids, including the Bacaba (ca. 3.0 Ga; Moreto et al., 2011) and Campina Verde (2.87–2.85 Ga; Feio et al., 2013) tonalites, the Ouro Verde felsic granulite (3.05 – 2.93 Ga; Marangoanha et al., 2019), and the Canaã dos Carajás (ca. 2.96 Ga; Feio et al., 2013), Bom Jesus (ca. 2.83 Ga; Feio et al., 2013) and Serra Dourada (ca. 2.86 Ga; Moreto et al., 2011) granites, are also considered part of the basement assemblage.

Metavolcano-sedimentary sequences correlated with the Neoarchean (ca. 2.76–2.73 Ga; Martins et al., 2017; Tallarico et al., 2005; Trendall et al., 1998) Itacaiúnas Supergroup (DOCEGEO, 1988; Machado et al., 1991; Wirth et al., 1986) overlie the basement rocks. The Itacaiúnas Supergroup was originally subdivided into the Igarapé Salobo, Grão Pará, Igarapé Bahia, and Igarapé Pojuca groups (DOCEGEO, 1988), which according to Tavares et al. (2018) are mostly represented, from bottom to top, by volcanic rocks, banded iron formation, and a clastic-sedimentary association. Alternatively, Araújo and

Nogueira (2019) and Araújo Filho et al. (2020) reinterpreted the stratigraphy of the metavolcano-sedimentary sequences of the Carajás Basin and proposed the following upward succession: Grão Pará Group (Parauapebas, Carajás, and Igarapé Bahia formations), overlapped by the Serra Sul, Azul, Águas Claras and Gorotire formations.

The Serra Sul Formation represents a ~600 m thick siliciclastic succession composed of subglacial and marine diamictites, interbedded with mudstone and black shale strata (ca. 2.58–2.06 Ga; Araújo and Nogueira, 2019), that covers the metavolcano-sedimentary sequences of the Grão Pará Group. Overlaying these glaciogenic deposits, the Azul, Águas Claras, and Gorotire formations are predominantly characterized by a broad set of conglomerate, sandstone, siltstone, and mudstone deposited in an offshore marine and coastal-fluvial to alluvial environments, between ca. 2.37 and 2.0 Ga (Araújo Filho et al., 2020; Araújo and Nogueira, 2019; Justo et al., 2018; Mougeot et al., 1996). Finally, orosirian sedimentary successions of the Paredão Group (ca. 2.0 Ga; Pereira et al., 2009) cover portions of the CD and BD, and comprise sedimentary breccias, polymictic to oligomictic conglomerates, and immature sandstones originated at continental alluvial fans and braided fluvial environments (Tavares et al., 2018).

Syntectonic A_2-type alkaline granites comprising the ca. 2.76–2.73 Ga Plaquê, Planalto, Estrela, Serra do Rabo, Igarapé-Gelado, and Pedra Branca suites (Avelar et al., 1999; Barros et al., 2009, 2004; Feio et al., 2013, 2012; Huhn et al., 1999; Sardinha et al., 2006), and ca. 2.57 Ga peralkaline to metaluminous granites, represented by the Old Salobo, Itacaiúnas, and the GT-46 granitic bodies (Machado et al., 1991; Souza et al., 1996; Toledo et al., 2019), define two major Neoarchean episodes of granitic magmatism recognized in the CD. Additionally, alkaline to subalkaline and metaluminous to slightly peraluminous granites of the ca. 1.88 Ga Serra dos Carajás Intrusive Suite (Central de Carajás, Young Salobo, Cigano, Pojuca, Breves, and Rio Branco granites; Machado et al., 1991; Tallarico et al., 2004), mark a widespread Paleoproterozoic granitic event at Carajás. Conversely, mafic-ultramafic magmatism in the CD (ca. 2.76–2.74 Ga) is chiefly represented by the Luanga layered complex, the Cateté Intrusive Suite, and the Pium Diopside-Norite (Ferreira Filho et al., 2007; Machado et al., 1991; Santos et al., 2013).

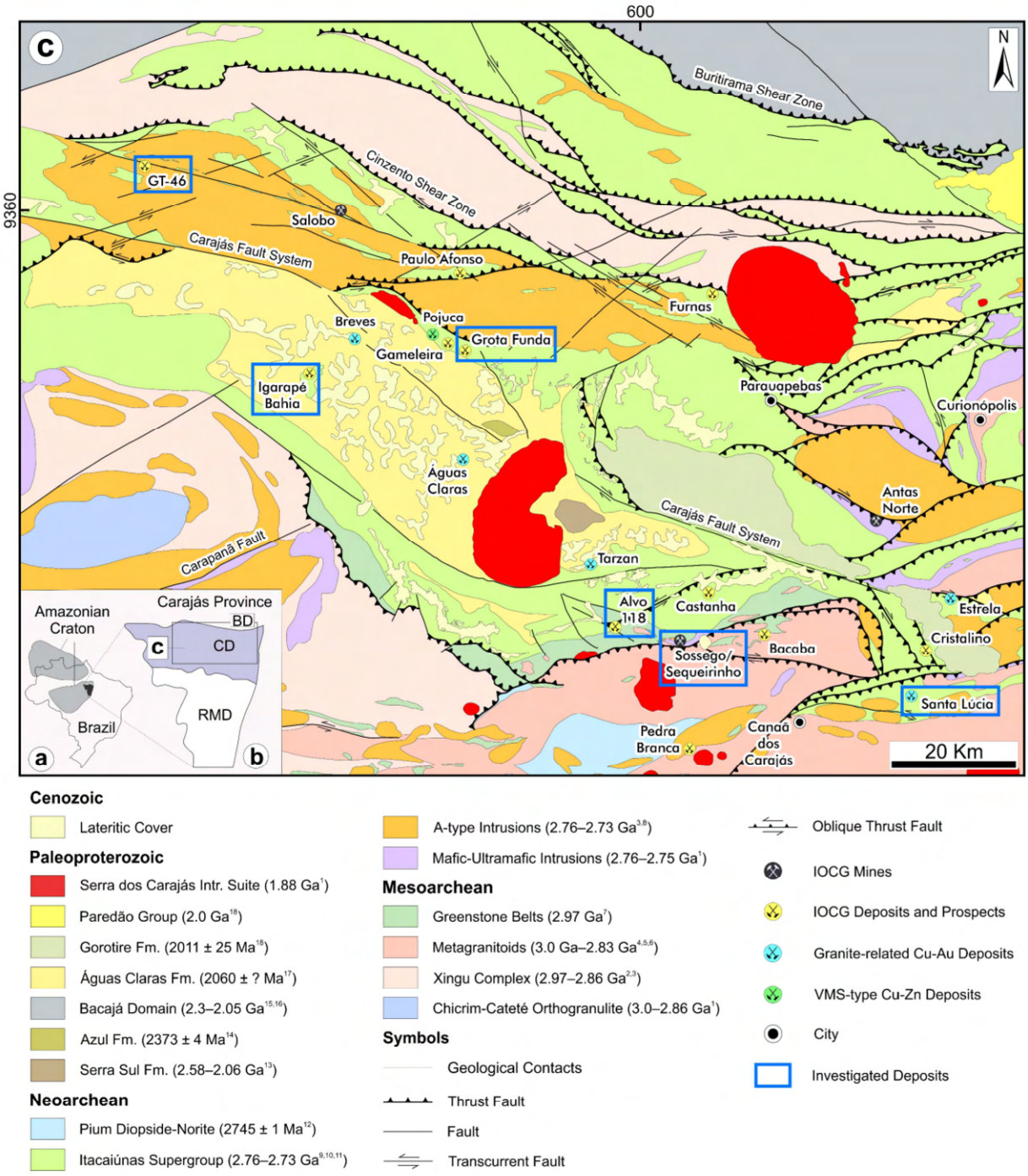

Fig. 1. (a) Location of the Carajás Province (black) in the northeastern portion of the Amazonian Craton (light grey), Brazil. (b) Segmentation of the Carajás Province into the Rio Maria Domain (south) and the Carajás Domain (north), this separated from the Bacajá Domain by the Buritirama Shear Zone. (c) Simplified geological map of the Carajás Domain, evidencing the spatial distribution of critical cupriferous deposits and the main Cu mines presently in operation, along with the major regional structures. The blue boxes indicate the approximate location of the investigated deposits (modified from Costa et al., 2016). Geochronological data compiled from: 1–Pidgeon et al. (2000); 2–Machado et al. (1991); 3–

Avelar et al. (1999); 4–Moreto et al. (2011); 5–Feio et al. (2013); 6–Marangoanha et al. (2019); 7–(Moreto et al. (2015b); 8–Feio et al. (2012); 9–Trendall et al. (1998); 10–Tallarico et al. (2005); 11–Martins et al. (2017); 12–Santos et al. (2013); 13–Araújo and Nogueira (2019); 14–Justo et al. (2018); 15–Macambira et al. (2009); 16–Vasquez et al. (2008a); 17–Mougeot et al. (1996); 18–Pereira et al. (2009). Abbreviations: IOCG = iron oxide-copper-gold, VMS = volcanogenic massive sulfide

The formation of the Carajás Basin has been either associated with intracratonic (DOCEGEO, 1988; Tavares et al., 2018) or magmatic, arc-related settings (Dardenne et al., 1988; Figueiredo e Silva et al., 2020). According to Pinheiro and Holdsworth (2000), progressive transtensional and transpressional deformation along regional, E-W- and ESE-NNW-striking shear zones (e.g., Cinzento and Carajás, in the north, and Canaã, in the south) was the main factor responsible for the inversion of the basin and the widespread E-W-trending foliation registered in the CD.

3. Geologic background of the investigated IOCG deposits

3.1. Sossego deposit

The Sossego deposit (98.3 Mt at 0.69% Cu, 0.19 g/t Au; VALE, 2021) lies along the regional WNW-ESE-striking Canaã shear zone, in the Southern Copper Belt (SCB), and comprises two main orebodies named Sequeirinho and Sossego (**Fig. 2a**; Monteiro et al., 2008a). The Sequeirinho orebody (**Fig. 2b**), which is accounted for 85% of the deposit bulk resources (Monteiro et al., 2008a), is mainly hosted by the Mesoarchean Sequeirinho Granite (ca. 3.0 Ga; Moreto et al., 2015b), and, to a lesser extent, by the Pista metadacite and a gabbronorite intrusive body (ca. 2.97 Ga and 2.74 Ga, respectively; Moreto et al., 2015b). All host rocks have undergone conspicuous hydrothermal alteration, including a regional and early sodic stage (albite-hematite), followed by sodic-calcic (actinolite-albite-magnetite-apatite; **Fig. 6a**), potassic (biotite and K-feldspar), and chlorite-rich (chlorite-epidote-allanite) alteration stages (Monteiro et al., 2008a; Moreto et al., 2015b). Steeply dipping breccia bodies concentrate most of the copper-gold mineralization, which is associated with an epidote-dominant, calcic assemblage. In the ore breccias, magnetite-actinolite-apatite-rich fragments constitute the earliest mineral assemblage (**Fig. 6b–d**), which is involved by a matrix containing chalcopyrite, pyrite, siegenite, millerite, cassiterite, sphalerite, and gold (Monteiro et al., 2008a). A monazite U-Pb age of 2712 ± 4.7 Ma is interpreted as the timing of IOCG mineralization for the Sequeirinho orebody (Moreto et al., 2015b).

The Sossego orebody (**Fig. 2c**) is located northeast of the Sequeirinho orebody and is mostly hosted by a Neoarchean granophyric granite intrusion (ca. 2.74 Ga; Moreto et al., 2015b). The sequence of hydrothermal alteration stages at Sossego is similar to that observed at Sequeirinho, encompassing early sodic (albite-calcite) and sodic-calcic (actinolite-albite-magnetite-apatite; **Fig. 6e**) alteration assemblages, which are overprinted by relatively more expressive potassic and chlorite alterations (Monteiro et al., 2008a). Subvertical breccia bodies represent the main style of copper-gold mineralization, which is chiefly characterized by a chalcopyrite-pyrite-quartz-carbonate-apatite-rich paragenesis. A late stage of hydrolytic alteration (sericite-hematite-quartz-chlorite-calcite), dominantly developed under brittle conditions, along with the evidence for open space filling in the breccias, strongly indicate that the Sossego orebody defines a structurally high-level portion of the Sossego deposit ore system (Monteiro et al., 2008a). *In situ* U-Pb dating of monazite yielded an age of 1879 ± 4.1 Ma for the Sossego orebody (Moreto et al., 2015b).

3.2. GT-46 deposit

The GT-46 deposit, also known as Igarapé Cinzento, lies within the WNW-ESE-striking Cinzento shear zone, which defines a major and regional discontinuity that also accommodates the Salobo, Paulo Afonso, and Furnas IOCG deposits, in the northern portion of the CD. Locally, the deposit is situated along with sub-vertical limbs of a fold structure which affects the host amphibolites (2774 ± 19 Ma, U-Pb in zircon) and schist rocks, as well as metamorphosed banded iron formations (BIFs) from the Grão Pará Group (**Fig. 3a**; Silva et al., 2005; Toledo et al., 2019). A regional tectonometamorphic event between 2.77 and 2.72 Ga is interpreted to be the main cause for the spaced S_n foliation observed in the host amphibolite rocks, whose mineral assemblage (i.e., hornblende + plagioclase + diopside + apatite; **Fig. 6f**) indicate an upper amphibolite facies metamorphism. Heterogeneous deformation during the development of the Cinzento shear zone at ca. 2.72 Ga generated a S_{n+1} foliation that transposes the previously established S_n. Intrusive rocks cut this metavolcano-sedimentary sequence and include a foliated tonalite (2560 ± 3.2 Ma), granodiorite, pegmatite (2562 ± 39 Ma, U-Pb in zircon; 2449 ± 44 Ma, Re-Os in molybdenite), undeformed granite (2564 ± 3.6 Ma), and diabase dikes (Toledo et al., 2019).

Widespread sodic-calcic and potassic alteration, along with intense iron metasomatism represent the early alteration sequence that preceded the first stage of disseminated chalcopyrite-bornite-magnetite mineralization in the deposit (mineralization I; **Fig. 3b**). Mineralized veins and breccia bodies with massive magnetite and chalcopyrite

(mineralization II) overprint previous zones of hydrothermal alteration and are intersected by halos of pervasive chloritization, which are directly associated with the emplacement of granitoids (Toledo et al., 2019). According to Toledo et al. (2019), circulation of hydrothermal fluids within the Cinzento shear zone was responsible for the development of the first stage of mineralization at GT-46 (2718 ± 56 Ma, Re-Os in molybdenite). A superimposed hydrothermal ore-forming event between ca. 2.72 and 2.5 Ga would have triggered the formation of mineralization II in the deposit (Toledo et al., 2019).

3.3. Grota Funda deposit

The Grota Funda deposit (15–40 Mt at 0.8–1.2% Cu; Hunger et al., 2018) in the northern sector of the CD, along with the Pojuca VHMS and Gameleira Cu polymetallic deposits, within the WNW-ESE-striking Pojuca fault system. The deposit is primarily hosted by mafic igneous rocks (basalt and diabase) attributed to the Igarapé Pojuca Group and, to a lesser extent, by a gabbroic unit, BIF, and a felsic subvolcanic rock (**Fig. 3c–d**). The mafic host rocks had been intensively affected by hydrothermal sodic-calcic, ferric, potassic and chlorite-quartz-tourmaline alteration stages. Three stages of copper mineralization were identified at Grota Funda, including massive magnetite-chalcopyrite bodies (I), brecciated chalcopyrite-magnetite-pyrrhotite-sphalerite ore (II), and massive chalcopyrite-chlorite-quartz zones (III), which have been respectively associated with the Fe-enrichment, potassic and chlorite alteration events. Within the ore breccia (mineralization II), apatite (**Fig. 6g**), quartz, and tourmaline represent the main gangue minerals, occurring surrounded by the chalcopyrite-dominant groundmass. Carbonate-quartz veins with open-space filling textures transect all host and wall rocks, as well as previous zones of hydrothermal alteration. A Re-Os molybdenite model age of 2530 ± 60 Ma (σ) is currently interpreted to represent the timing of formation for the mineralization I (Hunger et al., 2018).

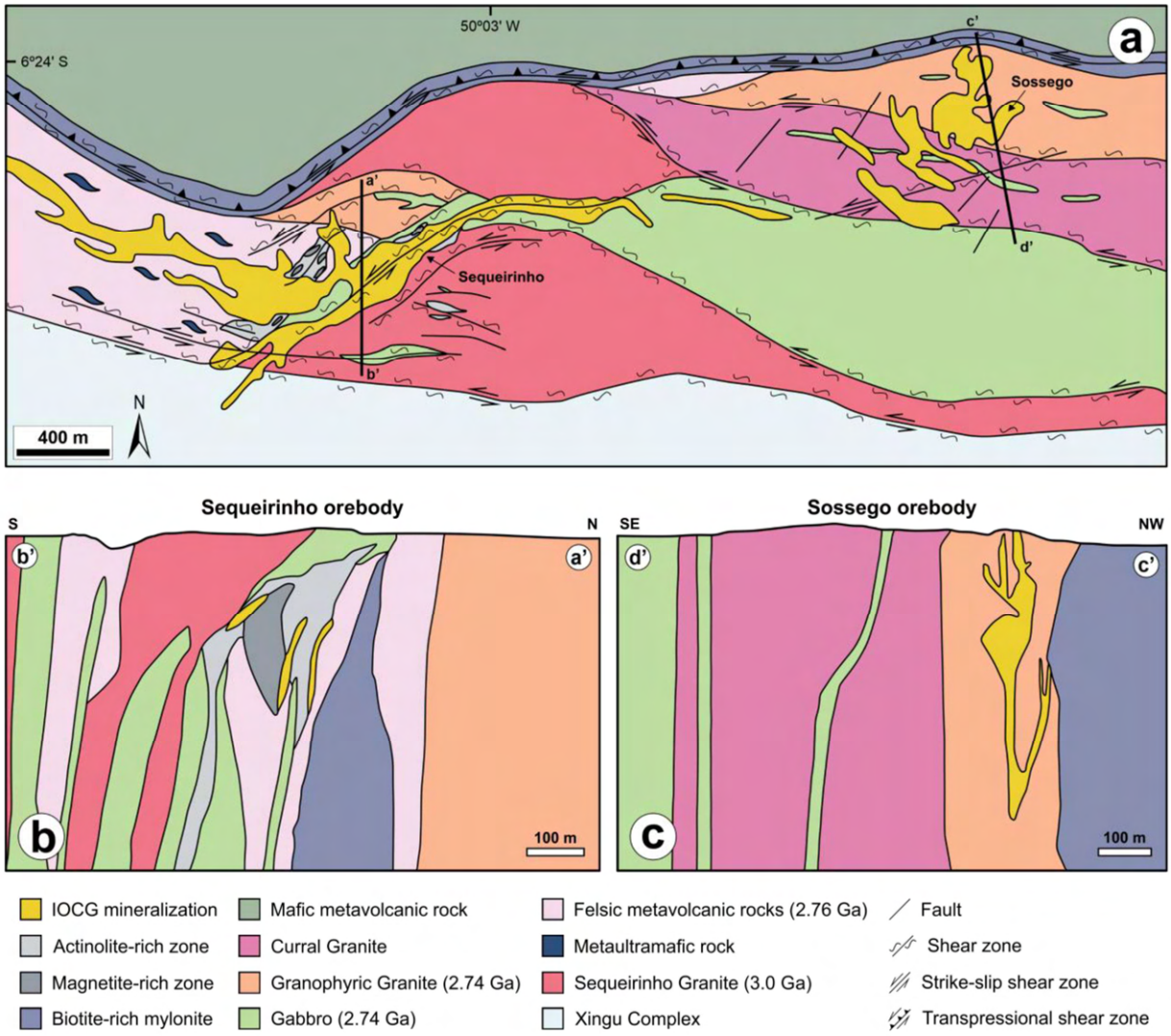

Fig. 2. (a) Geological map of the southern region of the CD indicating the locations of the Sequeirinho and Sossego orebodies. (b) Cross-sections of the Sequeirinho and (c) Sossego orebodies from the Sossego deposit (modified from Moreto et al., 2015b).

3.4. Igarapé Bahia/Alemão deposit

The Igarapé Bahia/Alemão IOCG deposit (219 Mt at 1.4% Cu, 0.86 g/t Au; Tallarico et al., 2005) is located in the northern sector of the CD, close to the regional-scale Carajás shear zone and within an erosional window through the metasedimentary rocks of the Águas Claras Formation (ACF; Melo et al., 2019). The deposit consists of four distinct orebodies denominated Alemão, Acampamento Norte, Acampamento Sul, and Furo 30 (**Fig. 4**), collectively hosted by the metavolcano-sedimentary rocks of the Igarapé Bahia Group, and a metagraywacke from the ACF (Dreher et al., 2008; Melo et al., 2019a; Tallarico et al., 2005). Early studies had described the Igarapé Bahia deposit as a stringer ore formed in the late Archean to the Paleoproterozoic (Ferreira Filho, 1985), which was later interpreted as a

syngenetic copper-gold mineralization related to a volcanic-exhalative system analogous to Besshi-type, volcanic-hosted massive sulfide (VHMS) deposits (Almada and Villas, 1999; Dreher et al., 2008; Villas and Santos, 2001). Conversely, an association with deposits from the IOCG class and, hence, an epigenetic origin for the copper-gold mineralization at Igarapé Bahia, was firstly proposed by Huhn and Nascimento (1997), and later endorsed by Tazava and Oliveira (2000) and Tallarico et al. (2005).

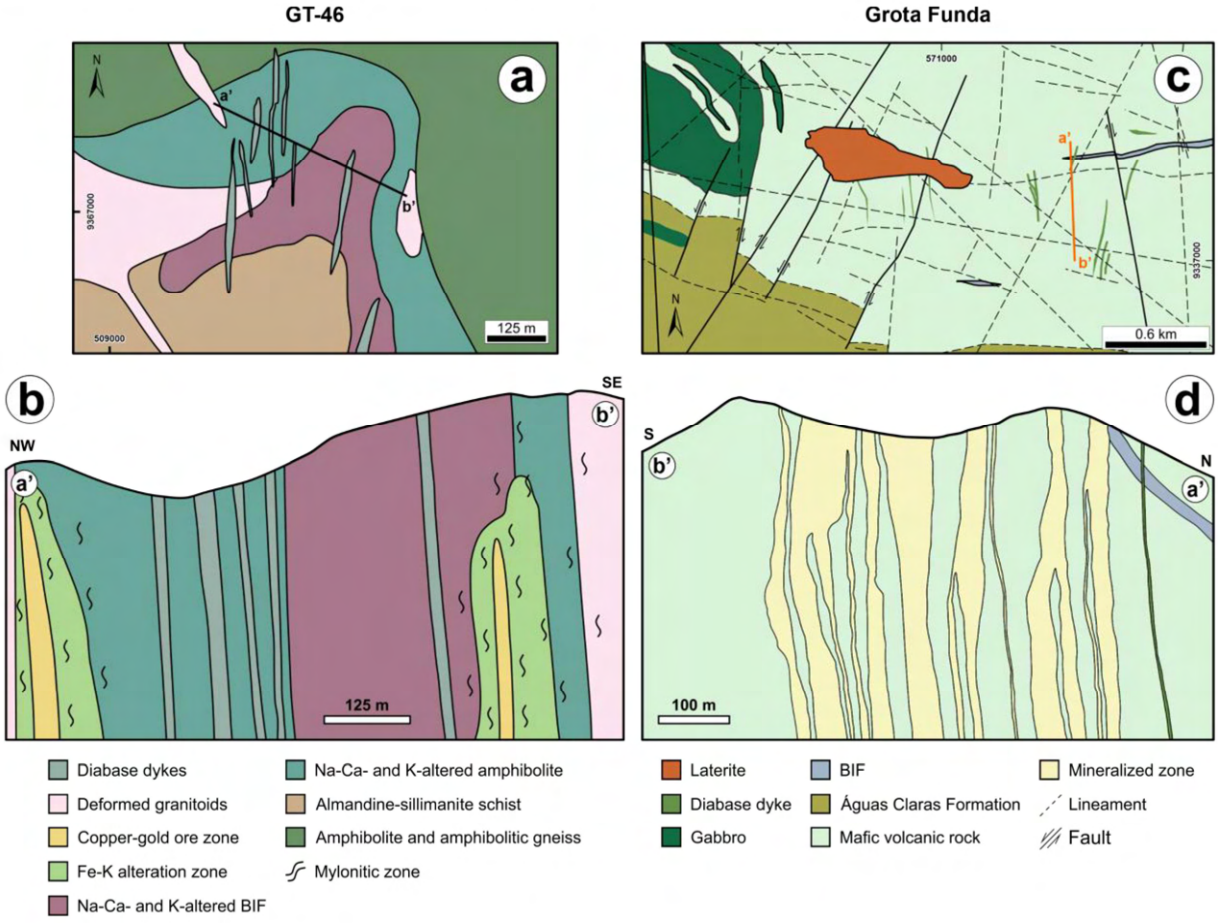

Fig. 3. (a) Simplified geological map and (b) NW-SE cross-section of the GT-46 deposit, showing the main host rocks, hydrothermal alteration zones and copper-gold mineralized bodies (modified from Toledo et al., 2019). (c) Geological map and (d) S-N cross-section of the Grota Funda deposit (modified from Hunger et al., 2018). Abbreviations: BIF = banded iron formation.

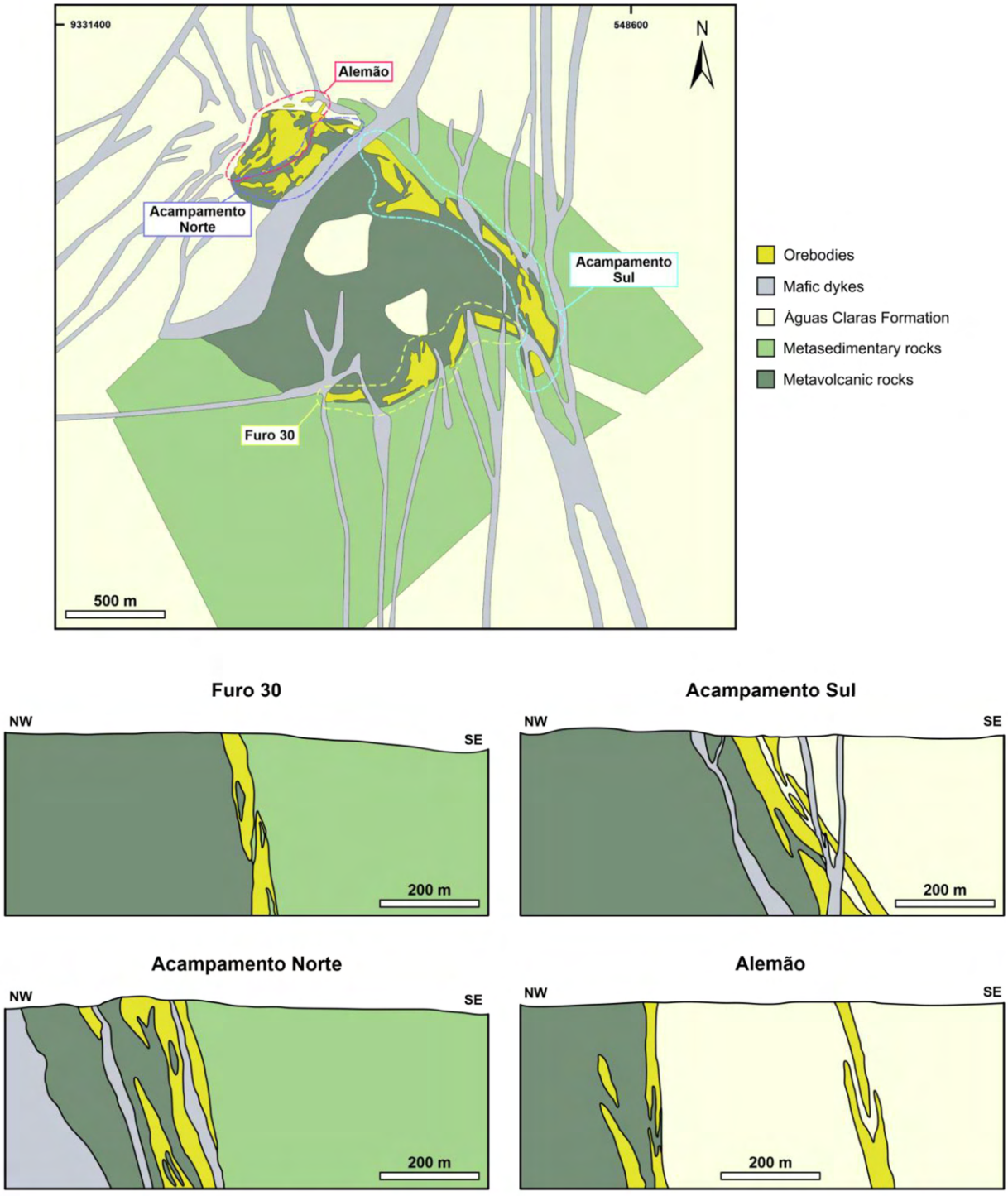

Fig. 4. Representative geological map of the Igarapé Bahia/Alemão deposit area, showing the approximate region covered by the Furo 30, Acampamento Sul, Acampamento Norte and Alemão orebodies (colored dotted curves). Their respective simplified cross-sections are shown below (modified from Melo et al., 2019).

More recently, Melo et al. (2019) suggested that chalcopyrite nodules and layers found within the metasedimentary upper sequence (ca. 2.76–2.73 Ga) of the Igarapé Bahia Group would represent a primary and syngenetic copper mineralization in the deposit,

possibly formed by exhalative processes similar to those described in VHMS systems. This primary mineralization would have been overprinted by an IOCG ore system at ca. 2.55–2.57 Ga (Melo et al., 2019a; Tallarico et al., 2005), which was strictly associated with ductile deformation and hydrothermal brecciation. The IOCG hydrothermal system is characterized by a paragenetic evolution that started with a distal and spatially restricted calcic-sodic alteration, followed by stages of potassic-(ferric), carbonate-(magnetite), and chlorite alteration. Copper-gold mineralization is similar for all orebodies and mostly confined to mylonitic zones and hydrothermal breccias. A striking feature of these orebodies is the abundance of phosphates, including apatite (**Fig. 6h**), cheralite, and autunite, as well as tungstates such as scheelite and wolframite. Late quartz-carbonate-chalcopyrite veins crosscut all previous zones of hydrothermal alteration and the orebodies (Melo et al., 2019a).

3.5. Alvo 118 deposit

The Alvo 118 deposit (170 Mt at 1.0 wt.% Cu, 0.3 g/t Au; Rigon et al., 2000) is situated approximately 12 km west of the Sossego deposit, adjacent to the contact between the Mesoarchean basement and the metavolcano-sedimentary units of the Itacaiúnas Supergroup (ca. 2.76 Ga). Within the Canaã shear zone, the deposit comprises two main tabular and sub-vertical orebodies named Principal Trend and Trend 2, which are primarily hosted by mafic to intermediate metavolcanic rocks associated with the Grão Pará Group, and, to a lesser extent, by granite, gabbro, and quartz porphyry dyke intrusions (**Fig. 5**; Rigon et al., 2000; Tallarico, 2003; Torresi et al., 2012). Crystallization ages for the granite (2743 ± 3 Ma) and porphyry dykes (2654 ± 9 Ma) were estimated by SHRIMP II ^{207}Pb-^{206}Pb zircon dating (Tallarico, 2003). Except for the dykes, all lithotypes have been extensively affected by structurally controlled hydrothermal alteration, this marked by a penetrative mylonitic foliation, and characterized by the following zonal sequence: (i) distal and poorly developed sodic alteration with scapolite and albite; (ii) potassic alteration with biotite development in the mafic metavolcanic rocks and gabbro, or plagioclase replacement by K-feldspar in the felsic host rocks, this usually associated with silicification and magnetite formation towards the ore zones; (iii) widespread and pervasive chlorite alteration, represented either by proximal halos around the copper-gold orebodies or a complex network of crosscutting veinlets in the host rocks and; (iv) post-ore quartz-sericite alteration and calcite-fluorite veining (Torresi et al., 2012).

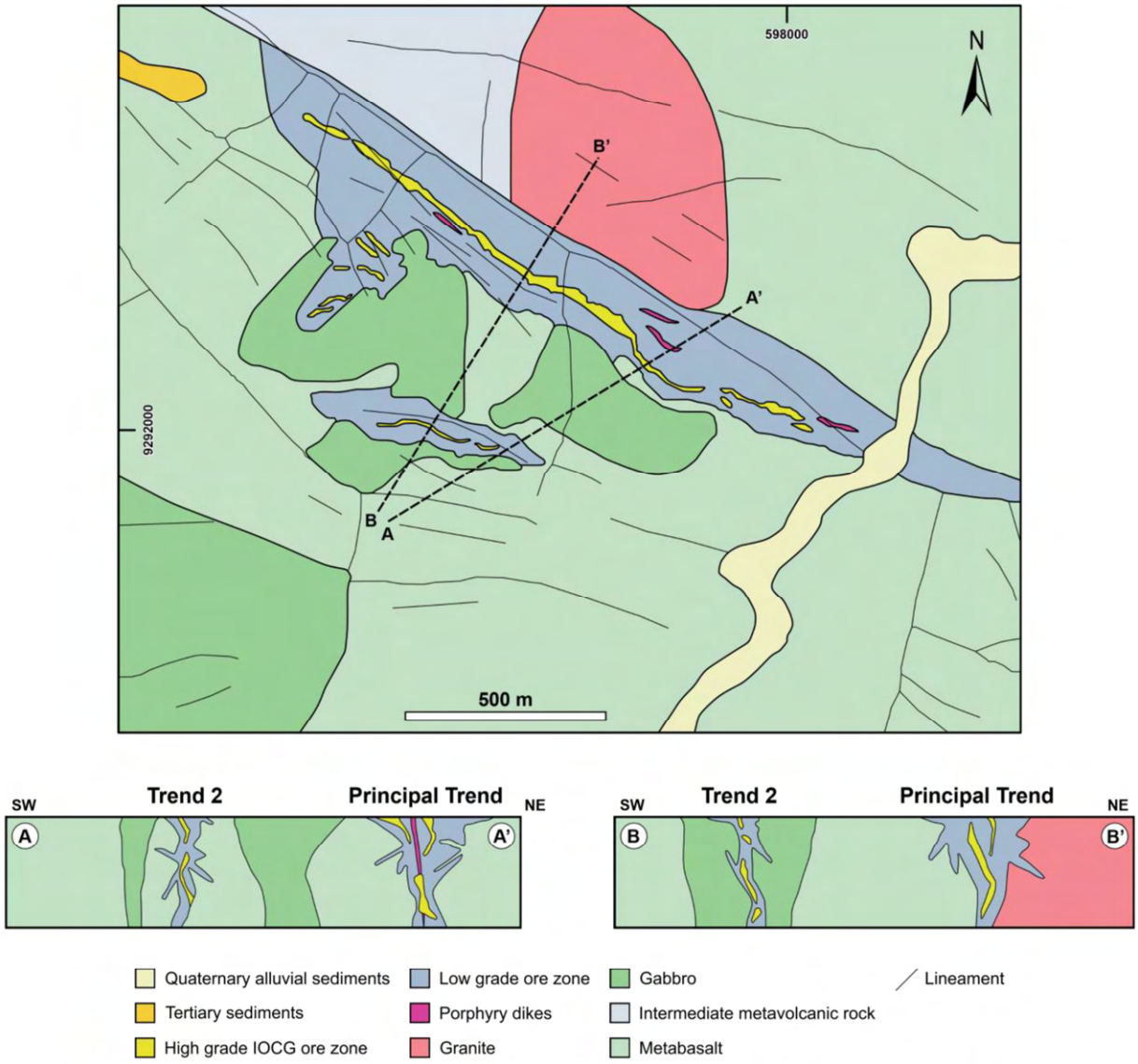

Fig. 5. Simplified geological map and cross-sections of the Alvo 118 IOCG deposit, displaying the geometry of the Trend 2 and Principal Trend orebodies (modified from Torresi et al., 2012).

Copper-gold mineralization in both Principal Trend and Trend 2 orebodies is chiefly characterized by matrix-supported, chalcopyrite-rich (up to 60 vol.%) breccia bodies and vein stockworks developed under brittle deformation. The ore assemblage consists of chalcopyrite, hematite, bornite, magnetite, and minor pyrite, which occur in association with calcite, quartz, chlorite, and apatite (**Fig. 6i;** Torresi et al., 2012). SHRIMP II U-Pb ages of 1869 ± 7 Ma and 1868 ± 7 Ma, obtained through dating of xenotime from massive and vein-type mineralization, respectively, constrain the timing of ore formation at Alvo 118 to the Paleoproterozoic (Tallarico, 2003).

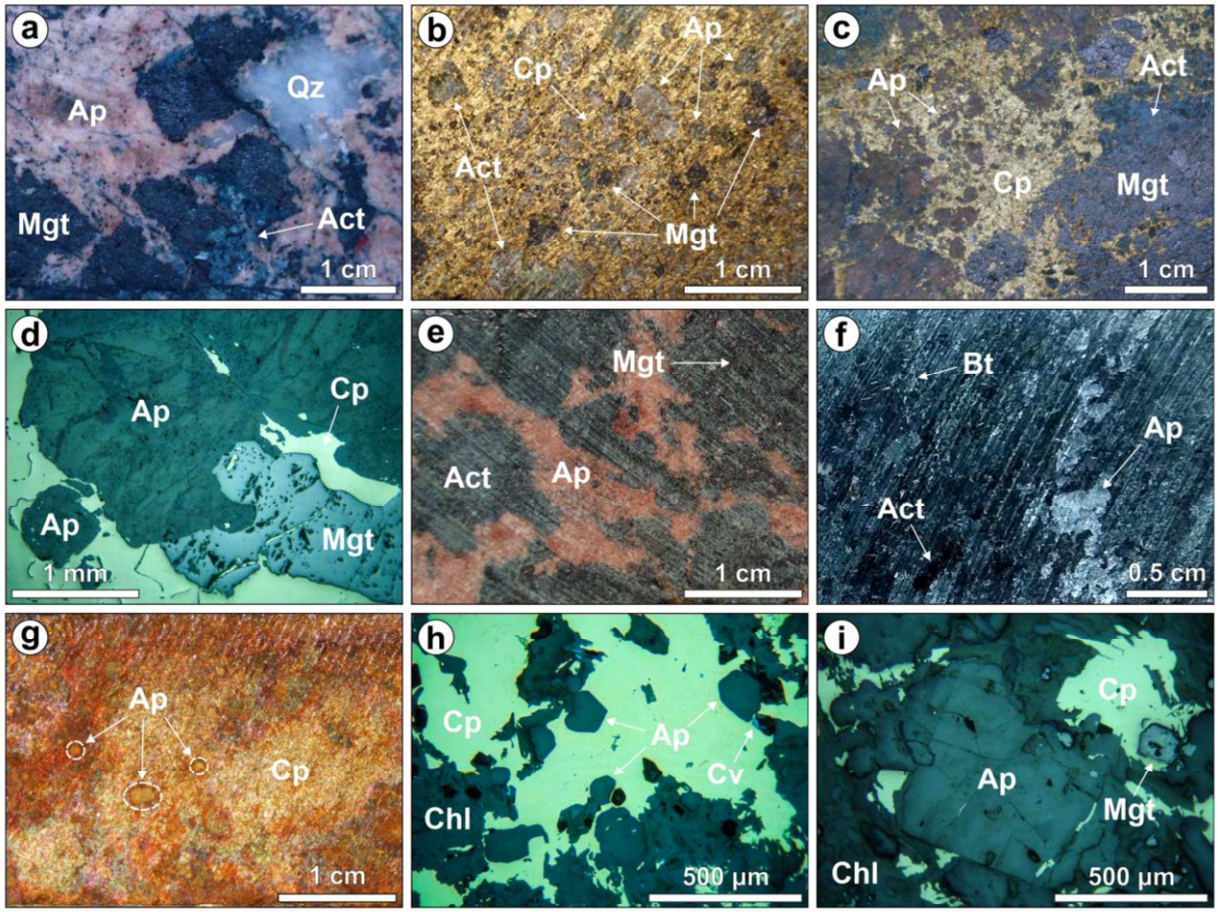

Fig. 6. Apatite general modes of occurrence for all the deposits investigated in this study. (a), (b), (c), (e), (f), and (g) are drill core samples, whereas (d), (h), and (i) are photomicrographs under reflected light/plane-polarized light (RL/PPL). (a) Na-Ca alteration assemblage of the Sequeirinho IOCG orebody with apatite, actinolite, magnetite and quartz. (b) and (c) Sequeirinho breccia ore zone evidencing actinolite, magnetite and apatite crystals/aggregates surrounded by a chalcopyrite-dominant groundmass. (d) Sequeirinho ore breccia displaying a chalcopyrite-magnetite-actinolite-apatite association. (e) Na-Ca alteration zone of the Sossego IOCG orebody, showing apatite intergrown with actinolite and magnetite. (f) Apatite from the GT-46 IOCG deposit in deformed hornblende-rich, mafic protolith (i.e., amphibolite). Note the presence of biotite flakes overprinting the hornblende crystals. (g) Brecciated ore body of the Grota Funda IOCG deposit, with massive chalcopyrite involving apatite crystals. (h) Igarapé Bahia/Alemão IOCG mineralization showing fine-grained apatite grains in association with chalcopyrite, chlorite and covellite. (i) Apatite associated with chalcopyrite and chlorite within the Alvo 118 IOCG orebody. Abbreviations: Act = actinolite, Ap = apatite, Chl = chlorite, Cp = chalcopyrite, Cv = covellite, Hbl = hornblende, Mgt = magnetite, Qz = quartz.

4. Analytical methods

4.1. Sample selection and petrography

Detailed petrographic studies of thin sections containing apatite from the Sequeirinho (samples SEQ-99/291.2 and SEQ-99/304), GT-46 (sample IC-44/340.1), Grota Funda (sample GR-39/339.7), Igarapé Bahia (sample IB-332/235.7), Sossego (sample SOS-315/235.4), and Alvo 118 (sample ALV-443/196.3) IOCG deposits were primarily undertaken to establish paragenetic relationships. A descriptive summary of the apatite modes of occurrence for each of the investigated deposits, according to the general context from which samples were respectively selected, is shown in **Table 1**. Representative apatite crystals were then investigated by BSE and CL imaging using a LEO 430i (Zeiss Company) scanning electron microscope (SEM), equipped with a Gatan Chroma CL detector, to determine complex textural domains. The CL images were acquired under a 15 kV accelerating voltage, working distance of 16 mm, and probe current between 6 and 10 nA. Whereas most apatite grains have evidenced notable zoning under CL light, no significant textural variations were observed in BSE images. Inclusions were identified using an Oxford energy dispersive spectroscopy (EDS) system coupled to the same SEM equipment. All these analytical steps were executed at the Institute of Geosciences, University of Campinas (UNICAMP), Brazil.

4.2. Electron probe microanalysis (EPMA)

EPMA analyses were conducted on a JEOL JXA-8230 instrument at the Laboratory of Microscopy and Microanalyses (LMic), Federal University of Ouro Preto (UFOP), Brazil. Quantitative spot analyses along line transects were done using the wavelength-dispersion mode, operated with a 20 kV accelerating voltage, 40 nA beam current, and 5 nm beam diameter. The following standards, X-ray lines, and crystals were used for all EMP analyses, except for samples SOS-315/235.4 and SEQ-99/291.2 in which fluorapatite was replaced by calcite to calibrate Ca: anorthoclase, Na$K\alpha$, TAPH; CaF_2, F$K\alpha$, TAPH; quartz, Si$K\alpha$, TAP; anorthite, Al$K\alpha$, TAP; olivine, Mg$K\alpha$, TAP; $BaSO_4$, Ba$L\alpha$, PETH; fluorapatite, Ca$K\alpha$ and P$K\alpha$, PETH; magnetite, Fe$K\alpha$, LIFH; scapolite (meionite), Cl$K\alpha$, PETH; pyrite, S$K\alpha$, PETH; rutile, Ti$K\alpha$, PETL; microcline, K$K\alpha$, PETL; Mn, Mn$K\alpha$, LIFL; $NdPO_4$, Nd$L\beta$, LIFL; $PrPO_4$, Pr$L\beta$, LIFL; $CePO_4$, Ce$L\alpha$, LIFL; $LaPO_4$, La$L\alpha$, LIFL; strontianite, Sr$L\alpha$, PETL. Peak and background counting times were 10 and 5 s for each of the analyzed elements, respectively. To mitigate the effects of migration during analysis, fluorine and sodium were invariably measured on the first cycle.

Table 1 Summary of apatite modes of occurrence by sample and deposit/orebody

Deposit Age (Ga)	Deposit / Orebody name	Sample name	Apatite mode of occurrence	References
2.72–2.68	Sequeirinho	SEQ-99/291.2	Intergrown with massive magnetite and actinolite in sodic-calcic altered domains	Monteiro et al. (2008a)
		SEQ-99/304	Constituent of the sulfide breccia matrix, representing the earliest mineral assemblage along with actinolite and magnetite	Monteiro et al. (2008a)
	GT-46	IC-44/340.1	Spatially associated with deformed hornblende-rich domains in supposedly mafic protolith (amphibolite?)	This study; Toledo et al. (2019)
2.57–2.53	Grota Funda	GR-39/339.7	Enclosed by chalcopyrite-magnetite-dominant groundmass in ore breccia	Hunger et al. (2018)
	Igarapé-Bahia	IB-332/235.7	Gangue mineral phase within chalcopyrite-pyrite-magnetite ore breccia	Melo et al. (2019); Tallarico et al. (2005)
1.90–1.88	Sossego	SOS-315/235.4	Paragenetically associated with actinolite and magnetite in early sodic-calcic alteration assemblages	Monteiro et al. (2008a)
	Alvo 118	ALV-443/196.3	Spatially associated with copper-gold mineralization, although crosscutted by chalcopyrite	Torresi et al. (2012)

Apatite structural formulae were calculated on the basis of 25 oxygen atoms and assuming that the monovalent anion site behaved ideally, according to "Approach 2" of Ketcham (2015). However, it is important to point out that, considering the random crystallographic orientations of the analyzed apatite grains, in addition to the operating conditions chosen for this study, which are different from those considered optimal for halogen (F and Cl) measurements (Goldoff et al., 2012), fluorine contents are believed to be overestimated in response to a significant increase in F X-ray counts. Indeed, fluorine values greater than the theoretical maximum concentration established for pure, end-member fluorapatite (3.77 wt%; Ptáček, 2016) predominate in grains from the majority of the studied deposits. Similarly, a decrease in Cl X-ray counts and a consequent underestimation of its true values cannot be completed ruled out, especially for analyses oriented near parallel to the apatite c-axis (Goldoff et al., 2012). As a result of these inaccuracies, the stoichiometrically determined OH contents (i.e., OH = 2 – F – Cl) have often yielded negative values, which were then considered below detection limit. Nevertheless, F and Cl data are here reported because they are essential for calculations and graphical representations since they indicate the basic compositional variability among apatite grains from each deposit. Net corrected total values below 97.5% were discarded from the data.

4.3. Laser ablation-ICP-MS analysis

Prior to LA-ICP-MS analyses, selected apatite grains were imaged by optical microscopic cathodoluminescence (OM-CL) at the State Key Laboratory of Geological Processes and Mineral Resources (GPMR), China University of Geosciences (Wuhan), using a LEICA DM 2700P microscope, coupled to a CITL8200 MK-5 CL system. These additional CL images were obtained with an exposure time of 6 s, utilizing a Leica camera system. Operating conditions included an accelerating voltage of 10 kV and a beam current of 250 μA.

Trace element analyses were performed at the Nanjing FocuMS Technology Co. Ltd facilities, utilizing a Cetac Excite 193nm laser ablation system coupled to an Agilent 7700x ICP-MS. A detailed description of the analytical procedures and data reduction is reported in Gao et al. (2013). The operating conditions for this study involved a 40 μm diameter beam and a 7 Hz repetition rate, with a counting time of 12 and 48 s for background and sample data acquisition, respectively. Element contents were calibrated against multiple reference materials, including NIST 610, NIST 612, BIR-1G, BCR-2G, BHVO-2G, GSE-1G, CGSG-1, CGSG-2, CGSG-4, and CGSG-5. To correct the time-dependent sensitivity drift and mass discrimination, every six to seven analyses of apatite were followed by one analysis of the NIST 610 standard. Offline data reduction, including the integration and selection of background and analysis signals, time drift correction, and quantitative calibration, was performed using the ICPMSDataCal software (Liu et al., 2008).

Additional analyses were executed using a 213 Nd:YAG (CETAC UP-213 nm) laser ablation system attached to a ThermoFisher Element II sector field ICP-MS, at the Applied Isotope Research Lab, UFOP. Each analysis was undertaken employing a spot size of 40 μm, a repetition rate of 6 Hz, and a 6 J/cm^2 fluence, considering 20 s of background acquisition, followed by 60 s of sample ablation. To minimize aerosol deposition around the ablation site, helium gas was flushed and mixed with argon gas downstream of the ablation cell. Based on previously obtained EPMA data, average CaO concentrations between 53-54.5 wt% were adopted as internal standards for calibration purposes. The NIST612 glass was used as the main calibration material, along with the BHVO and BCR glasses (reference values followed those of Jochum et al., 2016), to guarantee quality control. For all elements with concentrations above 10 ppm, the relative precision (RSD %) for multiple analyses of the quality control standards and deviation from the reference values were better than 20%. Raw

counts were processed offline and ensued by data reduction and concentration calculations using the Glitter software (Griffin et al., 2008).

5. Results

5.1. Apatite occurrences and textures

A summary of apatite petrographic characteristics from all deposits chosen for this study is reported in **Table 2**. General textural aspects of the investigated apatite crystals, including distinctive features between their internal domains, are based on conventional microscopy, as well as evidence from CL and BSE images.

5.1.1. Neoarchean (2.72–2.68 Ga) IOCG deposits

Apatite associated with actinolite-magnetite-dominant, Na-Ca alteration zones of the Sequeirinho orebody is medium- to coarse-grained (**Fig. 7a**), BSE-monotone and occurs in two distinct ways: (i) coarse (up to 0.5 cm in size), angular-shaped and porous apatite grain remnants (SEQ–1), which are riddled with nanometer-size monazite inclusions (**Fig. 7b**) and surrounded by a; (ii) relatively finer, limpid, and recrystallized mass of apatite subgrains. Both apatite varieties display orange luminescence, although non-recrystallized grains are more commonly dark brownish under CL light (**Fig. 7c**). In the brecciated ore zone of the Sequeirinho deposit, apatite grains are mostly medium-grained (<0.3 mm in size), subhedral to euhedral, and occur immersed in a matrix of chalcopyrite, locally forming granular aggregates with associated actinolite (SEQ–2; **Fig. 7d**). Fractures in these grains are chiefly filled with chalcopyrite. Relatively smaller apatite crystals usually display pseudo-hexagonal or prismatic habits, are BSE-monotone, and, similarly to apatite at Na-Ca-altered zones, also demonstrate dark brownish to orange luminescence (**Fig. 7e**). Monazite micro inclusions are identified within grains with higher porosity and tend to be coarser towards rim areas. Allanite overgrowths on apatite are also observed in places, generally evidencing reaction textures with both apatite and monazite (**Fig. 7f**).

At GT-46, apatite is medium- to coarse-grained (up to 0.6 cm in size), anhedral to euhedral, and occurs in apparent association with hornblende-rich domains (**Fig. 8a**). Both minerals are typically aligned along foliation planes that could possibly have been developed during the deformation of a mafic protolith, which was posteriorly affected by potassic (i.e., biotite formation) and carbonate alteration. Due to the deformational process, stretched prismatic and polycrystalline apatite grains are broadly found within the rock foliation (**Fig. 8b**). In any case, apatite crystals in GT-46 samples are BSE-monotone and yellowish-green

under CL imaging (GT–yg), locally displaying circular bluish spots of random internal distribution (GT-bl; **Fig. 8c**). Microfractures within apatite are usually filled with monazite, whereas allanite overgrowths are normally identified bordering the majority of the grains (**Fig. 8d**).

5.1.2. Neoarchean (2.57 Ga) IOCG deposits

In the Grota Funda deposit, ore-related apatite is medium- to coarse-grained (up to a few millimeters in size), anhedral to euhedral, and commonly forms prismatic crystals associated with chalcopyrite-magnetite-pyrrhotite (**Fig. 9a**). Some grains can exhibit corroded rims due to incipient chlorite alteration. Under CL light apatite crystals are dominantly yellowish-green (GF–2), although sectorized purplish CL domains (GF–1) are locally recognized (**Fig. 9b–c**). Chalcopyrite inclusions are generally abundant within relatively coarser grains and impart a "cheese-like" aspect to the apatite (**Fig. 9d**), which can also host subordinate pyrrhotite, quartz, allanite, monazite, and allanite crystals. Overgrowths of allanite are also characteristic of apatite at Grota Funda and apparently show reaction textures with chalcopyrite (**Fig. 9e**).

Ore-related apatite from the Igarapé Bahia/Alemão deposit is dominantly fine-grained (<800 μm in size) and forms subhedral to euhedral (prismatic) grains, or small aggregates, that occur dispersed in a matrix of chalcopyrite and generally intergrown with Mg-rich chlorite (**Fig. 9f**). Individual grains are essentially BSE-monotone (**Fig. 9g**) and most commonly inclusion free, although tiny carbonate, biotite, and ilmenite inclusions are recognized in places. Coarser grains can exhibit randomly oriented fractures that are usually filled by chalcopyrite. Under CL light, apatite at Igarapé Bahia evidence clear oscillatory zoning marked by relatively darker, brownish cores (IG–br) and thin yellowish-green rims (**Fig. 9h–i**).

5.1.3. Paleoproterozoic (1.90–1.87 Ga) IOCG deposits

Apatite associated with the Na-Ca alteration assemblage of the Sossego orebody is medium- to coarse-grained (up to 1 cm in size), subhedral to euhedral, and commonly forms hexagonally to rounded shaped crystals or elongated prisms that occur in paragenesis with actinolite and magnetite (**Fig. 10a**). All apatite grains have been intensively affected by hydrothermal alteration with biotite and, more pervasively, with carbonate (**Fig. 10a**). Under CL imaging, they are usually sector zoned and exhibit purplish CL domains (SOS–1) that are involved by brownish-yellow CL zones (SOS–2; **Fig. 10b**). Monazite inclusions are

remarkably abundant within apatite at Sossego and tend to be coarser (up to 100 µm) when within brownish-yellow CL zones (**Fig. 10c**).

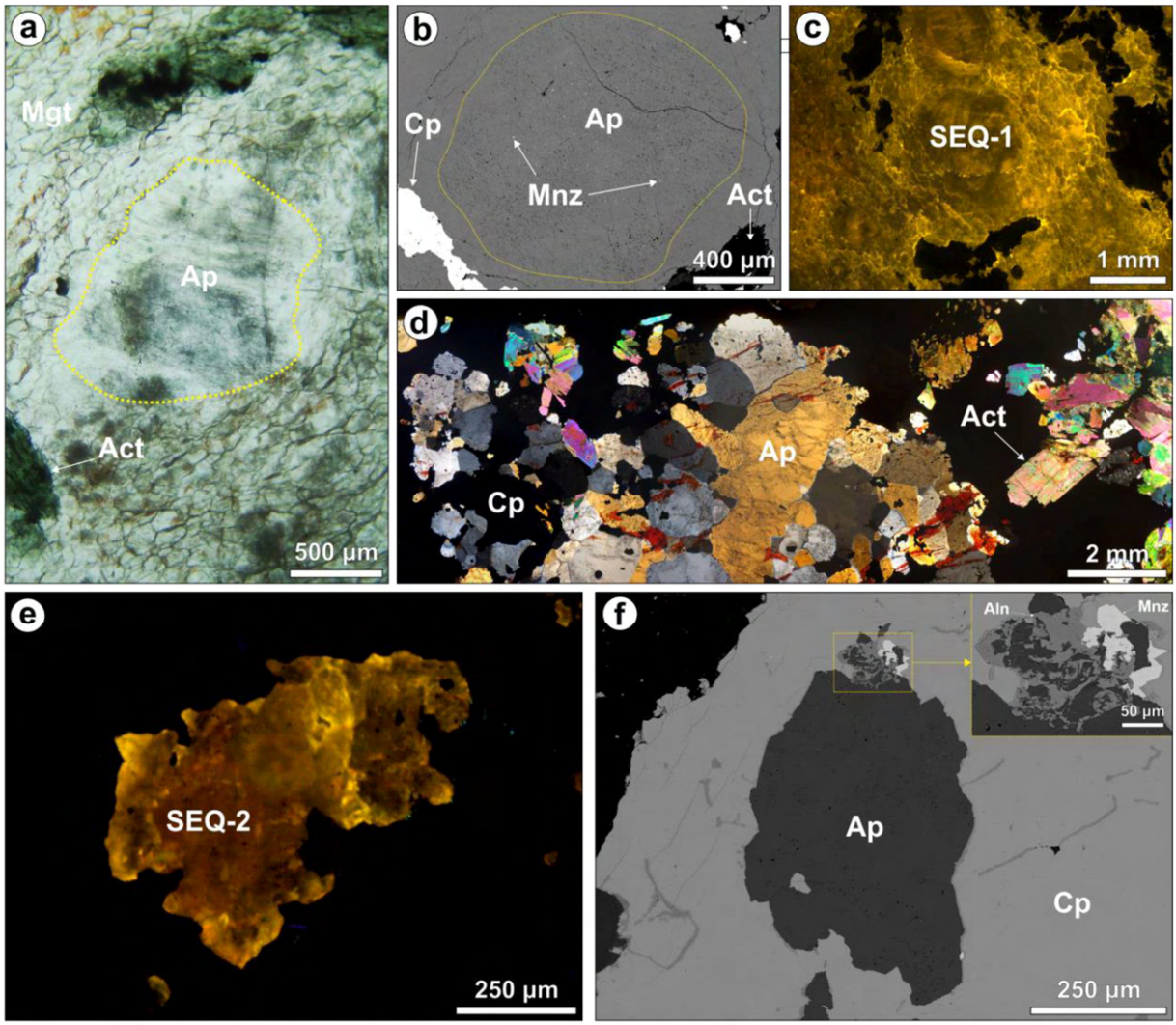

Fig. 7. Photomicrographs showing essential features of apatite grains from the Na-Ca alteration zone (SEQ–1) and ore breccia (SEQ–2) of the Sequeirinho deposit. (a) Angular-shaped apatite grain remnant associated with actinolite and surrounded by a recrystallized mass of apatite subgrains at Sequeirinho Na-Ca-altered domains (TL/PPL). (b) BSE image showing a porous apatite grain from the Sequeirinho Na-Ca alteration zone hosting several monazite nanoinclusions. (c) CL image of apatite from Na-Ca alteration zones of the Sequeirinho orebody displaying orange to brownish luminescent domains (SEQ–1). (d) Apatite aggregates associated with actinolite and within the chalcopyrite-rich breccia ore zone at Sequeirinho (TL/XPL). (e) Ore-related apatite crystal from the Sequeirinho deposit exhibiting dark brownish to orange luminescence (SEQ–2). (f) BSE image of an anhedral apatite grain surrounded by chalcopyrite and showing monazite and allanite overgrowths.

Abbreviations: Act = actinolite, Allanite = Aln, Ap = apatite, Cp = chalcopyrite, Mgt = magnetite, Mnz = monazite.

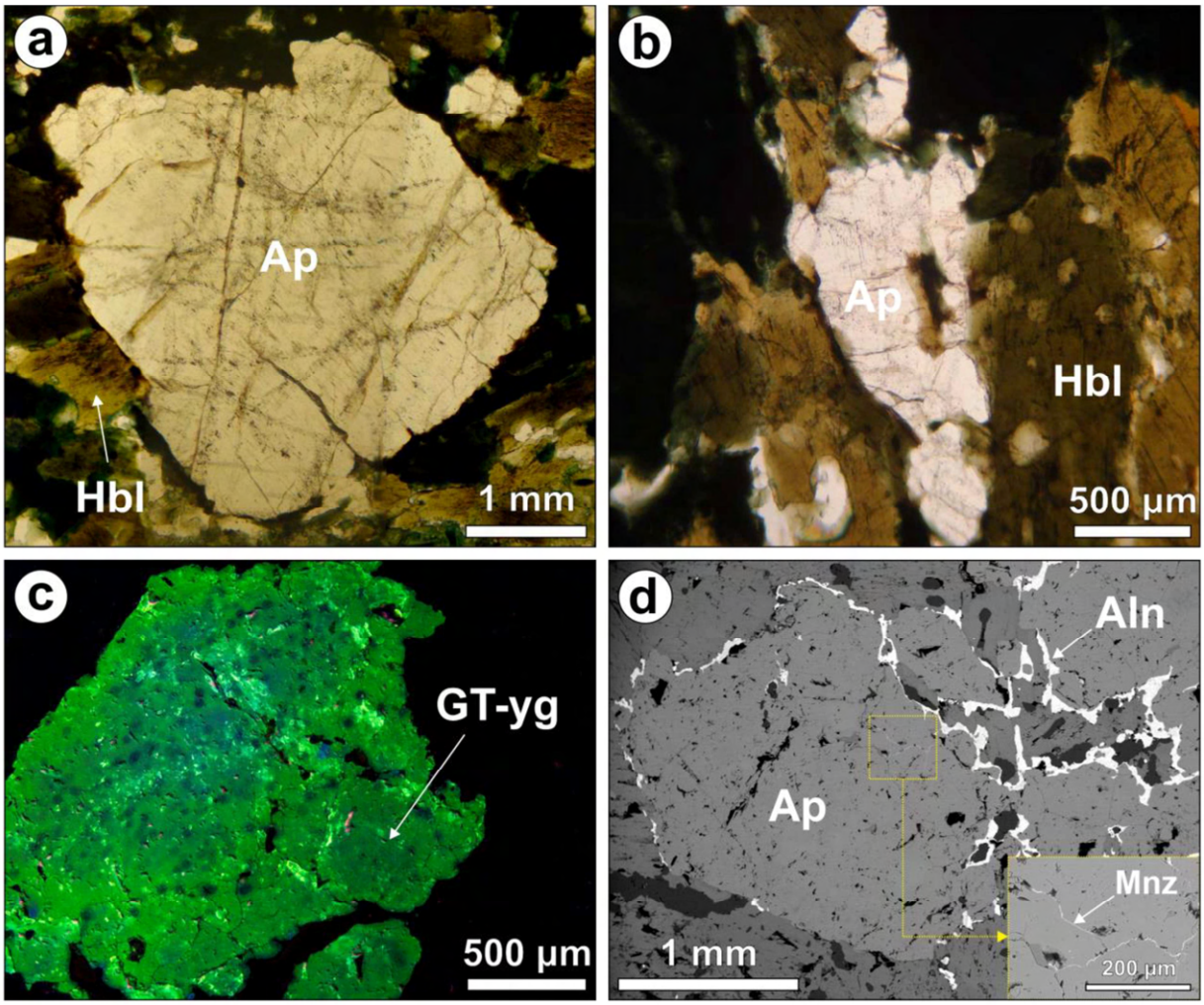

Fig. 8. Photomicrographs showing the main aspects of apatite grains from the GT-46 deposit. (a) Angular-shaped and (b) stretched apatite grains associated with hornblende (TL/PPL). (c) CL image of yellowish-green luminescent apatite crystal (GT–yg), showing randomly distributed circular bluish spots. (d) BSE image of apatite grains rimmed by allanite overgrowths. Note the presence of monazite fracture infills within apatite. Abbreviations: Aln = allanite, Ap = apatite, Hbl = hornblende, Mnz = monazite.

In ore samples of the Alvo 118 deposit, apatite occurs as fine-grained (hundreds of µm to few mm), anhedral to euhedral grains associated with chalcopyrite-chlorite-quartz-magnetite-rich zones (**Fig. 10d–e**). These apatite grains are BSE-monotone (**Fig. 10e–f**) and usually inclusion free, however, intensively fractured. In this case, fractures are predominantly filled with chalcopyrite, carbonate, chlorite, and, less frequently, with xenotime (**Fig. 10f**). CL microscopy reveals that ore-related apatite from the Alvo 118 deposit

is sectorized and displays dull greyish CL zones (ALV–2) that apparently surround bluish CL domains (ALV–1; **Fig. 10g–h**).

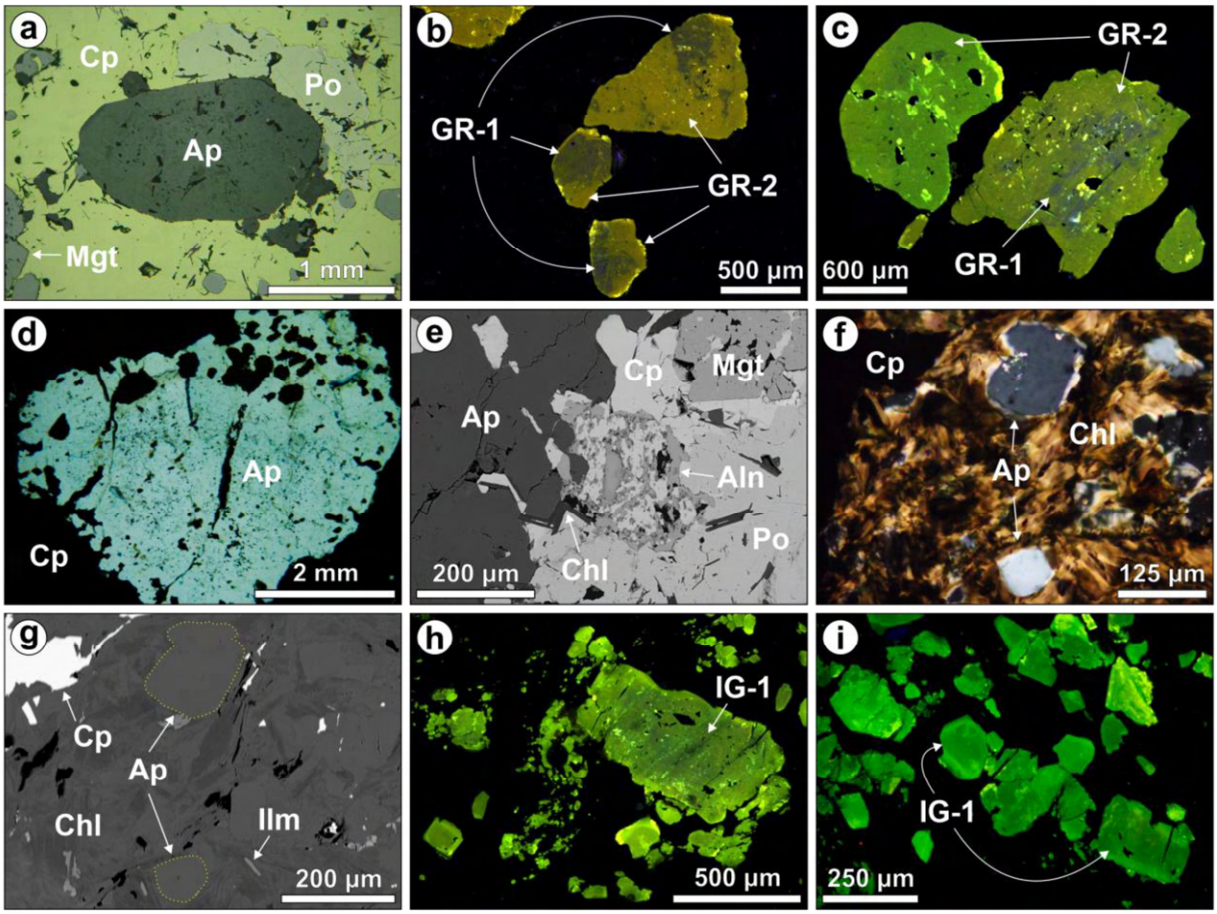

Fig. 9. Photomicrographs showing marked attributes of ore-associated apatite grains from the Grota Funda and Igarapé Bahia/Alemão IOCG deposits. (a) Prismatic apatite grain associated with chalcopyrite, pyrrhotite and magnetite in the main breccia ore zone of the Grota Funda deposit (RL/PPL). (b) Apatite grains at Grota Funda showing purplish CL domains (GF–1) involved by yellowish-green CL regions (GF–2). (c) "Cheese-like" aspect of apatite grain in association with chalcopyrite at Grota Funda. (d) BSE image of apatite grain within the ore breccia of the Grota Funda deposit rimmed by allanite overgrowths, which apparently exhibit reaction textures with chalcopyrite. (e) TL/XPL and (f) BSE images of fluorapatite crystals associated with chlorite and chalcopyrite in the ore zone of the Igarapé Bahia deposit. (g) and (h) CL images of ore-related apatite at Igarapé Bahia showing notably oscillatory zoning marked by relatively darker, brownish cores (IB–1) and thin yellowish-green rims. Abbreviations: Aln = allanite, Ap = apatite, Chl = chlorite, Cp = chalcopyrite, Ilm = ilmenite, Mgt = magnetite, Po = pyrrhotite.

Table 2 Apatite general petrographic characteristics by sample and deposit/orebody

Deposit / Orebody name	Sample name	Petrographic characteristics
Sequeirinho	SEQ-99/291.2	Coarse-grained (up to 0.5 cm in size), angular-shaped, porous crystals; riddled with monazite inclusions
	SEQ-99/304	Medium-grained (<0.3 mm in size), subhedral to euhedral crystals; forms granular aggregates in places
GT-46	IC-44/340.1	Medium- to coarse-grained (up to 0.6 cm in size), anhedral to euhedral crystals; locally polycrystalline and/or deformed (i.e., stretched)
Grota Funda	GR-39/339.7	Medium- to coarse-grained (up to a few mm in size), anhedral to euhedral crystals, with "cheese-like" aspect due to chalcopyrite inclusions
Igarapé-Bahia/Alemão	IB-332/235.7	Fine-grained (<800 μm in size), subhedral to euhedral (prismatic) crystals; locally forms small aggregates
Sossego	SOS-315/235.4	Medium- to coarse-grained (up to 1 cm in size), hexagonally to rounded shaped crystals; abundant in monazite inclusions
Alvo 118	ALV-443/196.3	Fine-grained (up to a few mm in size), anhedral to euhedral, and intensively fractured crystals; Fractures may be filled with chalcopyrite or xenotime

5.2. Chemical compositions of apatite

Compositional data for all apatite grains analysed in this study are reported in **Supplementary Tables S1** and **S2**, and representative results for each of the investigated deposits are shown in **Tables 3** and **4**. A summary of the main chemical attributes for each of the apatite varieties is presented in **Table 5**. A total of 910 and 189 spot analyses were performed by EPMA and LA-ICP-MS, respectively.

5.2.1. Major element data

Apatite from the majority of the deposits plot essentially within the fluorapatite field in a ternary F-Cl-OH diagram (**Fig. 11**), although the SEQ-1 apatite from the Na-Ca alteration zone of the Sequeirinho orebody indicates a hydroxyapatite composition, displaying estimated OH contents ranging from 1.32 to 2.15 wt% and the highest overall Cl concentrations among all samples considered in this study (1.76 wt% on average; **Fig. 12a**). Similarly, the ore-related SEQ-2 apatite at Sequeirinho also plots within the hydroxyapatite field in the ternary F-Cl-OH diagram, but has a relatively more variable halogen composition that reveals a clear trend towards lower chlorine and higher fluorine contents (**Fig. 11**). In this case, estimated OH, Cl, and F contents range from 0.03 to 1.94 wt%, 0.28 to 2.67 wt%, and 0.96 to 3.84 wt%, respectively (**Fig. 12a**). Considerably high F contents (above 6.0 wt%; see Analytical Methods 4.2 for considerations on F overestimations) are found in apatite from the

GT-46 (GT-yg), Grota Funda (GR-1 and GR-2 combined), and Igarapé-Bahia/Alemão (IG-br) deposits (**Fig. 12a–b**). Fluorapatite samples from the Sossego orebody (SOS-1 and SOS-2 combined) and Alvo 118 deposit (ALV-1 and ALV-2 combined) exhibit a significant variation in both estimated OH (0.003–0.93 wt% and 0.06–1.48 wt%, respectively) and F (2.44–5.23 wt% and 2.07–7.18 wt%, respectively) concentrations (**Fig. 11** and **12c**). Additionally, these fluorapatite also show a moderate variation in Cl contents, which span from 0.03 to 1.50 wt% at Sossego and from 0.002 to 0.11 wt% for the Alvo 118 samples (**Fig. 12c**).

Concentrations of CaO (46.71–56.44 wt%) and P_2O_5 (36.66–43.60 wt%) vary significantly among samples, whereas Na_2O contents are remarkably low (≤0.11 wt% on average), but most commonly below detection limit (BDL) in all apatite types. Similarly, MnO (≤0.08 wt%), BaO (≤0.05 wt%), TiO_2 (≤0.03 wt%), SO_3 (≤0.03 wt% on average), and SiO_2 (≤0.15 wt% on average) are consistently low among all the analysed apatite grains. Overall low to moderate concentrations are observed for FeO (≤0.29 wt% on average), with the highest values attained by the IG-br apatite (up to 4.18 wt %). Notably, correlations between Si + Na and S^{6+} + ∑REE (**Fig. 12d–f**) contents in apatite from all of the studied deposits do not show a strong degree of positive linearity.

5.2.2. Trace element data

The SEQ-1 apatite is relatively less enriched in Mg (2.80–155.49 ppm), Mn (80.77–126.29 ppm), Sr (107.13–379.66 ppm), and Y (91.60–150.78 ppm) when compared to the SEQ-2 apatite (7.02–1361.34, 112.88–234.88, 66.67–389.28, and 132.79–263.63 ppm, respectively). Conversely, the SEQ-2 apatite is characterized by lower Ga (0.04–0.50 ppm), Ba (0.31–5.10 ppm), Th (0.09–0.78 ppm), and U (0.09–0.58 ppm) contents relative to the SEQ-1 apatite (4.55–11.37, 3.09–33.18, 0.51–2.39, and 0.24–0.85 ppm, respectively; **Fig. 13a**). At GT-46, the GT-yg apatite is relatively high in Y (718.29–1212.73 ppm) and U (1.72–61.87 ppm), also demonstrating moderate concentrations of Th (0.28–8.71 ppm). Low to moderate Ga (<0.5 ppm) and Ba (<10 ppm) contents are also registered by the GT-yg apatite (**Fig. 13b**).

Within the ore zone of the Grota Funda deposit, Mg, Mn, Sr, and Ba contents are roughly equivalent between the GR-1 (15.7–1185.90, 385.46–475.62, 51.41–92.32, and 0.09–4.79 ppm, respectively) and GR-2 (12.21–214.36, 356.03–523.98, 43.04–82.34, 0.13–37.69 ppm, respectively) apatites, if outlier values are no considered (**Fig. 13c**). Indeed, Mg values above 500 ppm were found in the GR-1 apatite, but are still within the solubility limits for

fluorapatite (~22,000 ppm; Kreidler and Hummel, 1970; Pan and Fleet, 2002). Additionally, the GR-1 apatite has overall higher median Ga (0.07–0.88 ppm), Y (852.97–1649.16 ppm), Th (0.36–11.78 ppm) and U (1.17–7.25 ppm) values compared to the GR-2 apatite (0.03–6.77, 463.01–817.11, 0.03–5.07, and 0.27–1.99 ppm, respectively). At Igarapé-Bahia/Alemão, the IG-br apatite has the highest Sr contents (407.71–524.34 ppm) among the analysed apatite samples, also exhibiting significant Mn (306.95–403.67 ppm) and Y concentrations (229.17–321.7 ppm). In contrast, Ga (0.02–0.66 ppm), Th (0.003–0.76 ppm) and U (0.03–40.52 ppm) values are mostly low if outlier data is disregard in the latter case (**Fig. 13d**).

The SOS-1 apatite has overall higher trace element contents in comparison to the SOS-2 apatite (**Fig. 13e**), including Mg (6.73–593.46 ppm), Ga (0.99–17.97 ppm), Sr (138.66–251.44 ppm), Y (470.71–1174.19 ppm), Ba (3.36–201.20 ppm), Th (9.67–76.27 ppm) and U (4.89–59.68 ppm). Lastly, both ALV-1 and ALV-2 apatites are considerably high in Y (728.55–2246.04 and 657.86–2563.64 ppm, respectively) and display similar ranges of Mn (47.42–86.30 and 42.75–64.25 ppm, respectively) and Sr (81.69–102.93 and 59.09–101.65 ppm, respectively) **(Fig. 13f)**. Additionally, Mg values for the ALV-2 apatite (2.14–97.74 ppm) are mostly higher relative to those found in the ALV-1 apatite (4.63–906.02 ppm), whereas Ga (0.03–0.11 ppm) and Ba (below detection limit) are considerably lower.

5.2.3. Rare earth element (REE) data

The SEQ-1 and SEQ-2 apatites have similar total REE + Y contents (416.32–1423.26 ppm and 410.14–1479.66 ppm, respectively) and are analogously light-REE (LREE)-enriched (La_N/Yb_N = 7.56 and 2.69 on average, respectively) when compared to bulk ore samples from the Sequeirinho orebody (La_N/Yb_N = 22.19–55.14; Carvalho, 2009) (**Fig. 14a**). Conversely, apatite from the GT-46 deposit (GT-yg) shows heavy-REE (HREE) enrichment (La_N/Yb_N = 0.16–0.47; **Fig. 14b**) and negligible positive Y anomalies (Y/Y* = 0.99 on average).

At Grota Funda, the GR-1 apatite is relatively more enriched in total REE + Y contents (1624.91–3607.16 ppm) when compared to the GR-2 apatite (720.82–1514.09 ppm), although both varieties can evidence a HREE enrichment (La_N/Yb_N = 0.31–1.23 and 0.07–0.55, respectively), which is relatively more pronounced in the second case (**Fig. 14c**). In contrast, the IG-br apatite from the Igarapé Bahia/Alemão deposit is middle-REE (MREE)-enriched (La_N/Yb_N = 0.61–2.04; **Fig. 14d**) and has the lowest total REE + Y concentrations among all apatite samples considered in this study (491.86–807.95 ppm).

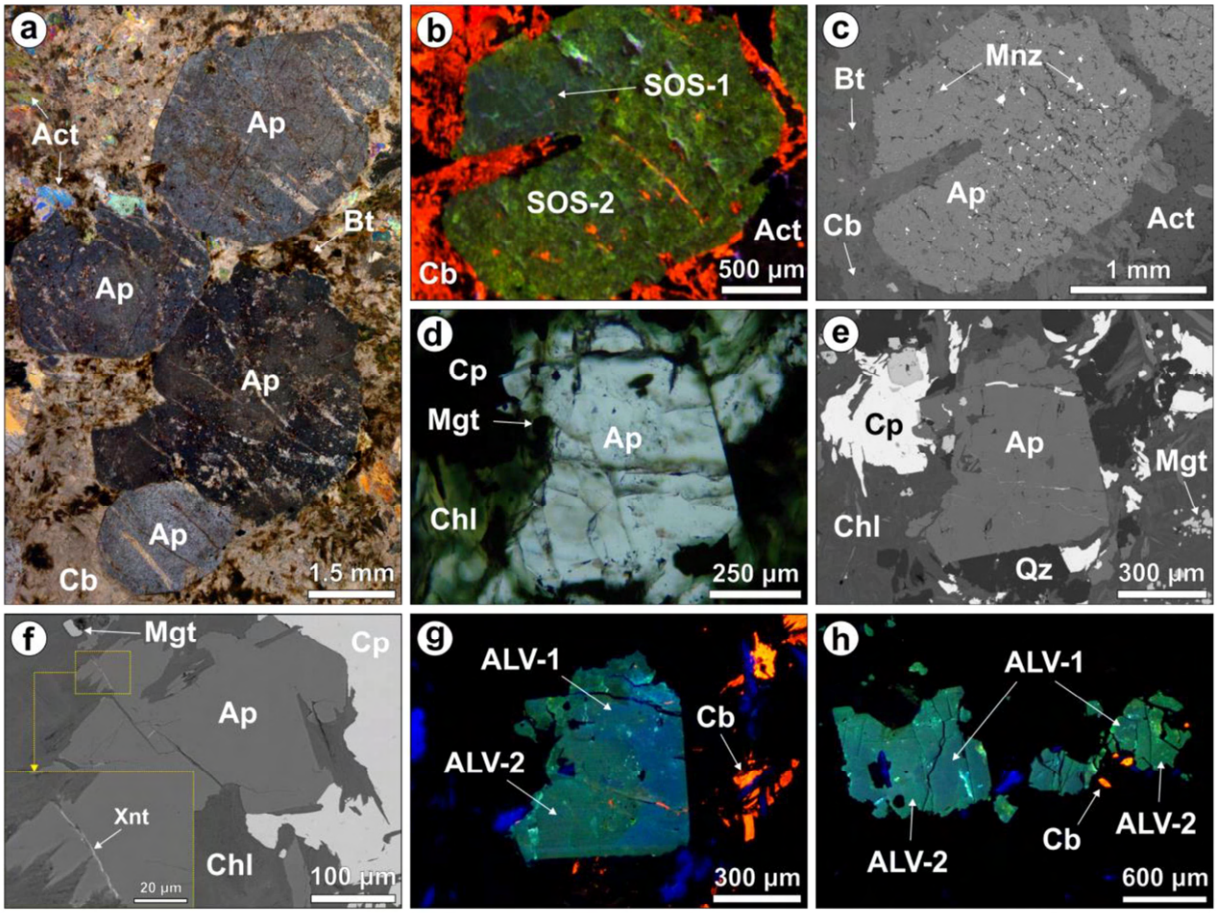

Fig. 10. Photomicrographs displaying the major characteristics of apatite grains associated with the Na-Ca alteration assemblage of the Sossego orebody and ore-related apatite from the Alvo 118 IOCG deposit. (a) Prismatic apatite grains in association with actinolite and affected by hydrothermal alteration with carbonate at Sossego (TL/XPL). (b) Sector zoned apatite grain from the Sossego orebody, showing purplish CL domains (SOS–1) that are involved by brownish-yellow CL zones (SOS–2). (c) BSE image of apatite grain associated with actinolite, both overprinted by hydrothermal alteration with biotite and carbonate at Sossego. Note that apatite is riddled with monazite inclusions of variable sizes. (d) TL/PPL and (e) BSE images of fine-grained apatite from the Alvo 118 deposit, in association with chalcopyrite-chlorite-quartz-magnetite-rich zones. (f) BSE-monotone apatite grain in the chalcopyrite-magnetite-chlorite ore zone of the Alvo 118 deposit exhibiting a xenotime fracture infill. (g) and (h) CL images of apatite at Alvo 118 displaying sector zoning with bluish CL domains (ALV–1) surrounded by dull greyish CL zones (ALV–2). Abbreviations: Act = actinolite, Ap = apatite, Bt = biotite, Cb = carbonate, Chl = chlorite, Cp = chalcopyrite, Mgt = magnetite, Qz = quartz, Xnt = xenotime.

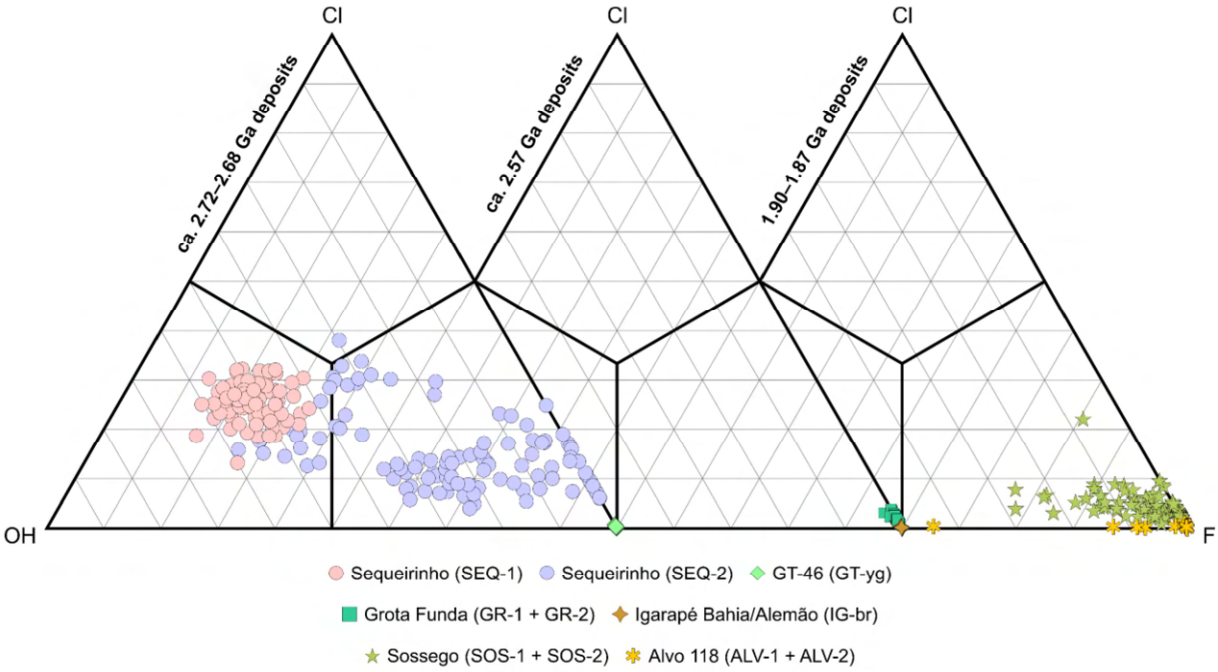

Fig. 11. Ternary F-Cl-OH diagram based on halogen atomic proportions in apatite (Webster and Piccoli, 2015).

The SOS-1 apatite from the Sossego Na-Ca alteration zone has the highest total REE + Y contents among the analysed apatite grains (8364.22–41945.05 ppm) and demonstrates strong LREE enrichment (La_N/Yb_N = 18.45–117.23; **Fig. 14e**). Comparatively, the SOS-2, ore-related apatite is significantly less LREE-enriched (La_N/Yb_N = 0.79–13.93) and exhibits lower total REE + Y concentrations (1189.71–3769.86 ppm). Nevertheless, both apatite types have analogous REE + Y distributions in comparison to bulk ore samples from the Sossego orebody (La_N/Yb_N = 21.17–54.93; Carvalho, 2009). Both ALV-1 (La_N/Yb_N = 0.27–1.06) and ALV-2 (La_N/Yb_N = 0.20–0.72) apatites from the Alvo 118 deposit are dominantly HREE-enriched (**Fig. 14f**) and, similarly to what is observed for the GT-yg apatite, display negligible positive Y anomalies (Y/Y* = 1.06 and 1.16 on average, respectively). Noteworthy, total REE + Y contents are somewhat higher for the ALV-1 apatite (2956.31 ppm on average) relative to the ALV-2 apatite (2804.82 ppm on average).

Strong negative Eu anomalies (Eu/Eu* = 0.27–0.43 on average) are evidenced by the majority of the analysed apatite grains, except for the ALV-1 (Eu/Eu* = 0.71) and ALV-2 Eu/Eu* = 0.75) apatites, which are moderate negative. Contrastingly, moderate positive Eu anomalies (Eu/Eu* = 1.77–2.06) are exclusively shown by the IG-br apatite (**Fig. 14a–f**).

Table 3 Representative EPMA data for apatite

EPMA (wt%)	Neoarchean (ca. 2.72–2.68 Ga) deposits						Neoarchean (ca. 2.57 Ga) deposits			
	Deposit: Sequeirinho Apatite: SEQ-1 (n = 78)		Deposit: Sequeirinho Apatite: SEQ-2 (n = 110)		Deposit: GT-46 Apatite: GT-yg (n = 49)		Deposit: Grota Funda Apatite: GR-1 + GR-2 (n = 131)		Deposit: Igarapé Bahia/Alemão Apatite: IG-br (n = 94)	
	Mean	Range	Mean	Range	Mean	Range	Mean	Range	Mean	Range
CaO	53.15	50.37–54.64	54.43	53.71–55.13	53.89	50.95–55.23	52.96	51.87–53.99	53.98	51.15–55.20
SrO	0.02	0.002–0.08	0.03	0.001–0.14	0.02	0.002–0.04	0.01	0.002–0.04	0.04	0.002–0.10
Na_2O	0.005	0.004–0.01	0.01	0.01–0.01	0.07	0.04–0.10	0.10	0.002–0.20	0.01	0.001–0.02
La_2O_3	0.03	0.002–0.11	0.03	0.002–0.08	0.03	0.002–0.13	0.03	0.002–0.07	0.03	0.002–0.10
Ce_2O_3	0.04	0.002–0.18	0.03	0.001–0.09	0.03	0.01–0.08	0.04	0.001–0.17	0.03	0.001–0.09
Pr_2O_3	0.04	0.003–0.12	0.04	0.001–0.10	0.04	0.001–0.12	0.03	0.001–0.09	0.04	0.001–0.12
Nd_2O_3	0.05	0.001–0.12	0.04	0.001–0.11	0.04	0.001–0.11	0.05	0.002–0.17	0.03	0.001–0.10
MnO	0.02	0.001–0.04	0.02	0.001–0.05	0.01	0.001–0.03	0.04	0.02–0.07	0.04	0.01–0.08
FeO	0.03	0.001–0.29	0.11	0.01–1.00	0.03	0.003–0.10	0.08	0.03–0.61	0.29	0.06–4.18
BaO	0.02	0.001–0.04	0.02	0.001–0.04	0.01	0.002–0.04	0.01	0.001–0.03	0.02	0.001–0.04
K_2O	0.004	0.001–0.04	0.004	0.001–0.02	0.005	0.001–0.06	0.005	0.001–0.08	0.002	0.001–0.01
Al_2O_3	0.14	0.001–4.13	0.01	0.001–0.04	0.17	0.001–5.06	0.02	0.001–0.51	0.02	0.001–0.25
P_2O_5	42.13	40.05–42.81	42.44	41.67–42.99	41.67	39.60–42.38	42.60	41.22–43.48	42.14	39.59–43.23
SiO_2	0.03	0.001–0.14	0.04	0.001–0.57	0.08	0.04–0.48	0.07	0.001–0.78	0.02	0.001–0.20
SO_3	0.01	0.001–0.04	0.03	0.001–0.41	0.01	0.001–0.04	0.01	0.001–0.15	0.01	0.001–0.06
TiO_2	0.005	0.001–0.02	0.004	0.001–0.01	0.004	0.001–0.01	0.004	0.001–0.01	0.01	0.001–0.02
F	0.87	0.49–1.26	2.41	0.96–3.84	5.21	4.45–6.13	4.36	3.52–7.51	5.23	4.55–6.78
Cl	1.76	0.91–2.23	1.05	0.28–2.67	0.04	0.01–0.08	0.18	0.07–0.36	0.02	0.002–0.04
–O = F,Cl	-0.77	-0.41–-1.03	-1.25	-0.47–-2.22	-2.20	-1.88–-2.60	-1.87	-1.50–-3.24	-2.21	-1.92–-2.86
Total	97.46	96.10–98.57	99.40	98.36–100.36	98.95	97.63–100.64	98.54	97.51–100.50	99.66	97.67–101.31
Est. OH	1.69	1.32–2.15	0.84	0.03–1.94	-	BDL	0.04	0.03–0.05	-	BDL
Net Correct. Total	99.15	97.97–100.13	100.11	98.94–101.46	98.95	97.63–100.64	98.54	97.51–100.50	99.66	97.67–101.31

Table 3 (continued)

EPMA (wt%)	Paleoproterozoic (ca. 1.90–1.87 Ga) deposits			
	Deposit: Sossego Apatite: SOS-1 + SOS-2 (n = 109)		Deposit: Alvo 118 Apatite: ALV-1 + ALV-2 (n = 93)	
	Mean	Range	Mean	Range
CaO	54.44	48.92–55.78	53.95	52.58–55.29
SrO	0.02	0.001–0.07	0.01	0.001–0.04
Na_2O	0.06	0.003–0.34	0.11	0.002–0.34
La_2O_3	0.07	0.002–1.65	0.03	0.002–0.08
Ce_2O_3	0.11	0.001–3.07	0.03	0.002–0.12
Pr_2O_3	0.05	0.002–0.34	0.03	0.001–0.08
Nd_2O_3	0.06	0.001–0.77	0.03	0.001–0.14
MnO	0.02	0.001–0.05	0.01	0.001–0.04
FeO	0.03	0.002–0.27	0.06	0.001–0.35
BaO	0.01	0.001–0.04	0.02	0.001–0.05
K_2O	0.01	0.001–0.05	0.003	0.001–0.01
Al_2O_3	0.18	0.001–9.59	0.02	0.001–0.27
P_2O_5	42.36	40.02–43.34	42.59	41.32–43.49
SiO_2	0.03	0.001–0.27	0.07	0.01–0.22
SO_3	0.01	0.001–0.03	0.01	0.001–0.02
TiO_2	0.004	0.001–0.01	0.005	0.001–0.03
F	3.62	2.44–5.23	5.16	2.07–7.18
Cl	0.28	0.03–1.50	0.02	0.002–0.11
–O = F,Cl	-1.59	-1.03–-2.54	-2.18	-0.87–-3.05
Total	99.56	97.46–102.35	99.80	98.06–101.40
Est. OH	0.24	0.003–0.93	0.50	0.06–1.48
Net Correct. Total	99.69	97.72–102.35	99.83	98.06–101.40

Abbreviations: BDL = below detection limit

Table 4 Selected LA-ICP-MS trace element concentrations for apatite

LA-ICP-MS (ppm)	Neoarchean (ca. 2.72–2.68 Ga) deposits						Neoarchean (ca. 2.57 Ga) deposits			
	Deposit: Sequeirinho Apatite: SEQ-1 (n = 11)		Deposit: Sequeirinho Apatite: SEQ-2 (n = 12)		Deposit: GT-46 Apatite: GT-yg (n = 24)		Deposit: Grota Funda Apatite: GR-1 (n = 11)		Deposit: Grota Funda Apatite: GR-2 (n = 18)	
	Mean	Range	Mean	Range	Mean	Range	Mean	Range	Mean	Range
Mg	20.44	2.80–155.49	147.54	7.02–1361.34	39.18	11.17–309.90	178.21	15.7–1185.90	29.40	12.21–214.36
Si	1435.34	1200.39–1744.57	699.57	386.10–2090.50	645.93	128.76–1185.66	1098.14	603.84–2550.06	595.34	276.73–884.76
Sc	0.25	0.09–0.48	1.04	0.63–1.38	0.94	0.52–1.37	1.14	0.85–1.67	0.98	0.66–1.84
Ti	65.43	58.41 72.91	622.78	597.96 644.97	661.36	622.67 701.82	608.18	570.61 634.12	594.69	565.20 616.80
V	1.34	0.66–2.93	1.34	0.35–3.34	0.20	0.13–0.33	1.28	0.31–7	0.39	0.10–1.60
Mn	107.83	80.77–126.29	162.17	112.88–234.88	113.32	101.24–123.35	428.50	385.46–475.62	414.56	356.03–523.98
Cu	0.40	0.10–1.07	23.81	21.27–25.02	27.73	8.13–118.17	23.03	18.52–25.55	24.52	19.22–61.84
Ga	6.85	4.55–11.37	0.17	0.04–0.50	0.08	0.02–0.31	0.27	0.07–0.88	0.84	0.03–6.77
Ge	2.20	0.81–5.36	9.82	4.44–19.67	10.36	4.65–23.22	19.13	8.01–29.95	5.62	1.93–10.80
Rb	0.10	0.02–0.33	0.08	0.02–0.24	0.23	0.15–0.54	0.40	0.18–1.42	0.20	0.09–0.69
Sr	180.11	107.13–379.66	226.88	66.67–389.28	122.65	112.29–130.49	67.36	51.41–92.32	63.60	43.04–82.34
Y	116.49	91.60–150.78	201.33	132.79–263.63	970.15	718.29–1212.73	1203.30	852.97–1649.16	615.84	463.01–817.11
Nb	0.02	0.01–0.04	0.02	0.02–0.04	0.10	0.05–0.14	0.03	0.03–0.05	0.02	0.01–0.04
Mo	0.05	0.003–0.11	0.13	0.08–0.18	0.12	0.09–0.15	0.24	0.15–0.36	0.21	0.12–0.30
Cd	0.03	0.03–0.03	0.07	0.04–0.18	0.05	0.03–0.10	0.05	0.03–0.09	0.05	0.04–0.07
Sn	0.94	0.55–1.43	0.26	0.11–1.45	0.08	0.05–0.12	0.10	0.04–0.31	0.09	0.05–0.18
Sb	0.04	0.004–0.08	0.02	0.01–0.03	0.01	0.01–0.02	0.01	0.01–0.02	0.01	0.01–0.02
Ba	12.18	3.09–33.18	1.40	0.31–5.10	0.70	0.11–8.76	1.52	0.09–4.79	5.92	0.13–37.69
La	77.21	30.72–184.34	51.29	16–98.59	26.09	13.78–61.30	82.56	34.10–169.32	13.37	3.29–31.37
Ce	241.81	105.31–542.6	205.02	70.90–437.22	148.91	67.69–385.11	364.08	136.12–691.53	71.58	17.75–170.74
Pr	33.72	15–71.89	32.89	12.50–70.45	29.60	12.44–75.15	59.95	23.01–103.10	14.41	3.59–32.45
Nd	149.39	73.36–294.01	167.32	70.51–349.11	178.14	76.88–416.50	317.95	128.66–511.72	88.87	25.71–173.16
Sm	28.75	16.46–54.52	49.16	24.47–83.90	73.76	40.58–132.91	101.69	50.12–144.1	38.14	15.06–57.40
Eu	3.49	2.10–6.67	6.10	2.52–13.97	6.79	4.70–10.06	8.10	3.92–11.23	3.98	2.36–5.48
Gd	30.38	20.59–50.86	37.78	17.39–70.40	49.03	27.26–94.02	89.48	43.23–131.37	31.71	13.69–46.93
Tb	3.50	2.50–5.59	9.93	5.77–14.52	23.41	15.45–35.41	31.65	19.58–39.10	14.18	8.73–19.56
Dy	20.29	15.29–31.46	41.22	26.39–51.23	139.31	101.30–176.04	189.90	132.58–254.04	92.78	63–126.67
Ho	4.33	3.48–5.80	9.81	6.58–12.20	38.10	28.56–46.78	52.89	37.03–71.43	26.55	19.40–35.78

Table 4 (continued)

LA-ICP-MS (ppm)	Neoarchean (ca. 2.72–2.68 Ga) deposits						Neoarchean (ca. 2.57 Ga) deposits			
	Deposit: Sequeirinho Apatite: SEQ-1 (n = 11)		Deposit: Sequeirinho Apatite: SEQ-2 (n = 12)		Deposit: GT-46 Apatite: GT-yg (n = 24)		Deposit: Grota Funda Apatite: GR-1 (n = 11)		Deposit: Grota Funda Apatite: GR-2 (n = 18)	
	Mean	Range	Mean	Range	Mean	Range	Mean	Range	Mean	Range
Er	11.30	9.35–14.20	22.69	13.94–29.22	88.60	63.91–113.61	121.95	82.99–165.49	59.39	42.97–80.44
Tm	1.36	1.05–1.70	2.90	1.86–3.86	15.34	11.44–18.95	19.82	13.78–28.08	9.75	7.02–13.31
Yb	6.76	4.96–8.43	12.25	7.43–17	69.82	50.12–88.34	85.99	58.46–121.62	42.11	30.48–55.47
Lu	1.06	0.76–1.26	1.76	1.09–2.36	10.02	7.53–12.36	12.07	8.36–17.49	5.94	4.41–8.09
Hf	0.02	0.01–0.06	-	BDL	0.24	0.21–0.31	0.18	0.16–0.19	0.14	0.14–0.14
W	0.72	0.03–1.38	0.23	0.03–0.58	1.16	0.52–2.40	0.26	0.10–0.49	0.22	0.06–0.59
Pb	0.50	0.14–1.38	0.47	0.14–2.54	0.70	0.17–1.74	6.73	0.18–57.9	3.44	0.01–30.11
Th	1.42	0.51–2.39	0.34	0.09–0.78	3.04	0.28–8.71	4.54	0.36–11.78	1.82	0.03–5.07
U	0.41	0.24–0.85	0.29	0.09–0.58	13.36	1.72–61.87	4.30	1.17–7.25	0.83	0.27–1.99
Total REE + Y	729.86	416.32–1423.26	851.42	410.14–1479.66	1867.08	1239.93–2878.92	2741.39	1624.91–3607.16	1128.60	720.82–1514.09
Total LREE	502.14	224.39–1092.84	456.51	169.91–955.37	382.75	170.79–938.06	824.54	321.89–1475.67	188.23	50.69–407.72
La_N/Yb_N	7.56	2.69–14.85	2.69	1.21–4.71	0.25	0.16–0.47	0.63	0.31–1.23	0.21	0.07–0.55
Ce/Ce*	1.15	1.12–1.19	1.21	1.15–1.27	1.28	1.20–1.42	1.25	1.18–1.31	1.24	1.18–1.31
Eu/Eu*	0.36	0.33–0.41	0.41	0.29–0.57	0.36	0.27–0.43	0.27	0.20–0.34	0.37	0.23–0.51

Table 4 (continued)

LA-ICP-MS (ppm)	Neoarchean (ca. 2.57 Ga) deposits		Paleoproterozoic (ca. 1.90–1.87 Ga) deposits							
	Deposit: Igarapé Bahia/Alemão Apatite: IG-br (n = 13)		Deposit: Sossego Apatite: SOS-1 (n = 11)		Deposit: Sossego Apatite: SOS-2 (n = 11)		Deposit: Alvo 118 Apatite: ALV-1 (n = 5)		Deposit: Alvo 118 Apatite: ALV-2 (n = 8)	
	Mean	Range	Mean	Range	Mean	Range	Mean	Range	Mean	Range
Mg	42.55	6.32–253.35	236.17	6.73–593.46	76.85	6.29–536.17	190.73	4.63–906.02	27.81	2.14–97.74
Si	545.32	293.02–1077.35	1109.74	398.89–1451.44	488.84	157.22–1480.53	834.34	240.63–1518.63	756.13	377.92–1025.32
Sc	1.71	0.41–7.21	1.04	0.57–1.33	1.10	0.74–1.98	1.12	0.89–1.46	0.99	0.64–1.22
Ti	642.02	545.56–1412.89	651.45	611.88–675.11	637.93	627.85–648.09	598.16	588.36–609.05	605.64	588.41–635.33
V	0.34	0.02–0.97	0.69	0.29–1.09	0.22	0.09–0.72	0.40	0.17–0.67	0.24	0.02–0.39
Mn	356.11	306.95–403.67	134.24	100.98–180.71	141.93	75.30–235.27	63.27	47.42–86.30	52.96	42.75–64.25
Cu	24.78	19.45–32.42	23.32	11.83–26.53	25.31	24.18–28.10	20.12	19.39–20.52	20.16	18.12–25.30
Ga	0.18	0.02–0.66	4.59	0.99–17.97	1.55	0.56–3.15	0.33	0.04–0.91	0.05	0.03–0.11
Ge	3.55	2.33–5.05	141.04	65.52–314.67	21.92	8.95–44.98	13.93	10.48–16.39	10.43	8.13–12.23
Rb	0.13	0.03–0.86	2.45	0.50–4.68	2.30	0.72–5.10	0.71	0.26–1.46	0.36	0.10–1.16
Sr	462.87	407.71–524.34	220.62	138.66–251.44	163.69	91.63–205.19	93.08	81.69–102.93	80.76	59.09–101.65
Y	271.12	229.17–321.7	726.44	470.71–1174.19	520.88	272.86–970.49	1622.22	728.55–2246.04	1672.70	657.86–2563.64
Nb	0.59	0.02–1.71	0.13	0.06–0.33	0.04	0.02–0.10	0.03	0.01–0.06	0.02	0.02–0.02
Mo	0.19	0.12–0.26	0.19	0.11–0.26	0.14	0.11–0.17	-	BDL	-	BDL
Cd	0.04	0.03–0.06	0.10	0.04–0.34	0.07	0.03–0.14	0.05	0.04–0.06	0.05	0.03–0.09
Sn	0.10	0.05–0.20	0.13	0.09–0.16	0.24	0.06–1.10	0.26	0.05–0.74	0.07	0.06–0.08
Sb	0.02	0.02–0.03	0.04	0.01–0.18	0.03	0.01–0.10	0.02	0.02–0.02	0.02	0.02–0.02
Ba	2.10	0.09–5.39	40.53	3.36–201.20	17.02	4.79–33.70	4.50	1.86–9.61	1.76	1.76–1.76
La	21.24	10.77–47.29	3564.44	1524.26–8830.59	208.79	39.99–432.57	62.47	48.06–88.08	41.93	31.65–53.54
Ce	67.01	37.79–128.41	8821.21	3600.44–20753.92	747.49	209.72–1403.30	240.21	182.06–292.66	173.00	132.48–211.78
Pr	9.88	6.01–16.09	851.30	368.01–1978.14	95.79	33.47–191.92	40.66	31.20–46.60	30.05	23.07–35.03
Nd	53.68	35.43–81.73	2586.67	1128.80–6252.51	382.08	145.57–789.05	222.46	167.69–257.72	166.94	124.71–196.29
Sm	21.89	16.14–29.28	369.54	174.64–844.94	93.71	50.04–184.97	102.33	81.54–116.73	79.07	63.02–94.75
Eu	13.76	10.67–19.75	46.63	23.17–95.89	12.19	6.93–19.90	21.33	17.99–24.13	17.85	13.84–22.15
Gd	22.98	17.12–29.18	678.80	311.11–1509.20	97.38	41.37–183.06	83.00	69.75–96.27	66.17	51.43–82.55
Tb	9.57	7.83–11.23	76.70	40.17–167.17	23.06	14.22–37.40	35.18	26.90–45.21	30.45	16.77–41.44
Dy	60.05	52.44–69.29	160.75	98.40–253.05	104.79	54.26–191.46	215.42	132.02–281.61	204.47	89.23–296.44
Ho	14.51	12.74–16.79	35.15	23.06–54.19	25.84	13.01–48.99	56.25	31.06–78.29	54.33	21.03–80.35

Table 4 (continued)

LA-ICP-MS (ppm)	Neoarchean (ca. 2.57 Ga) deposits		Paleoproterozoic (ca. 1.90–1.87 Ga) deposits							
	Deposit: Igarapé Bahia/Alemão Apatite: IG-br (n = 13)		Deposit: Sossego Apatite: SOS-1 (n = 11)		Deposit: Sossego Apatite: SOS-2 (n = 11)		Deposit: Alvo 118 Apatite: ALV-1 (n = 5)		Deposit: Alvo 118 Apatite: ALV-2 (n = 8)	
	Mean	Range	Mean	Range	Mean	Range	Mean	Range	Mean	Range
Er	25.15	20.54–30.70	127.31	80.52–231.93	60.61	34.27–109.99	122.50	63.33–173.75	123.27	46.37–186.32
Tm	3.11	2.39–3.99	10.52	6.51–17	8.67	4.64–18.23	21.34	9.14–30.16	22.10	6.97–35.52
Yb	11.29	8.37–16.63	48.18	27.55–78.20	37.29	19.70–80.36	97.93	37.61–142.82	107.60	30.41–178.22
Lu	1.24	0.87–2.04	6.09	3.32–9.73	4.94	2.13–10.34	12.99	4.06–18.92	14.89	4.11–25.68
Hf	0.13	0.13–0.13	0.45	0.27–0.75	0.18	0.16–0.22	0.18	0.16–0.20	0.16	0.14–0.21
W	0.12	0.02–0.55	0.08	0.05–0.15	0.17	0.06–0.36	0.29	0.17–0.49	0.14	0.08–0.23
Pb	0.17	0.11–0.36	20.06	3.99–52.88	11.53	6.53–20.17	0.30	0.03–0.55	0.09	0.02–0.18
Th	0.14	0.003–0.76	23.09	9.67–76.27	2.01	0.02–4.02	0.56	0.21–1.42	0.23	0.09–0.49
U	5.25	0.03–40.52	20.72	4.89–59.68	2.33	0.12–8.26	0.99	0.05–4.37	0.13	0.01–0.25
Total REE + Y	606.49	491.86–807.95	18109.72	8364.22–41945.05	2423.50	1189.71–3769.86	2956.31	1877.80–3929.52	2804.82	1406.84–4102.81
Total LREE	151.82	90.15–263.20	15823.61	6621.51–37815.16	1434.15	428.75–2775.89	565.80	429.01–679.81	411.92	311.91–496.64
La_N/Yb_N	1.26	0.61–2.04	50.46	18.45–117.23	4.88	0.79–13.93	0.52	0.27–1.06	0.32	0.20–0.72
Ce/Ce*	1.13	1.06–1.23	1.22	1.16–1.33	1.32	1.19–1.52	1.16	1.11–1.22	1.18	1.14–1.24
Eu/Eu*	1.87	1.77–2.06	0.29	0.26–0.31	0.43	0.15–0.66	0.71	0.68–0.73	0.75	0.70–0.83

Abbreviations: BDL = below detection limit

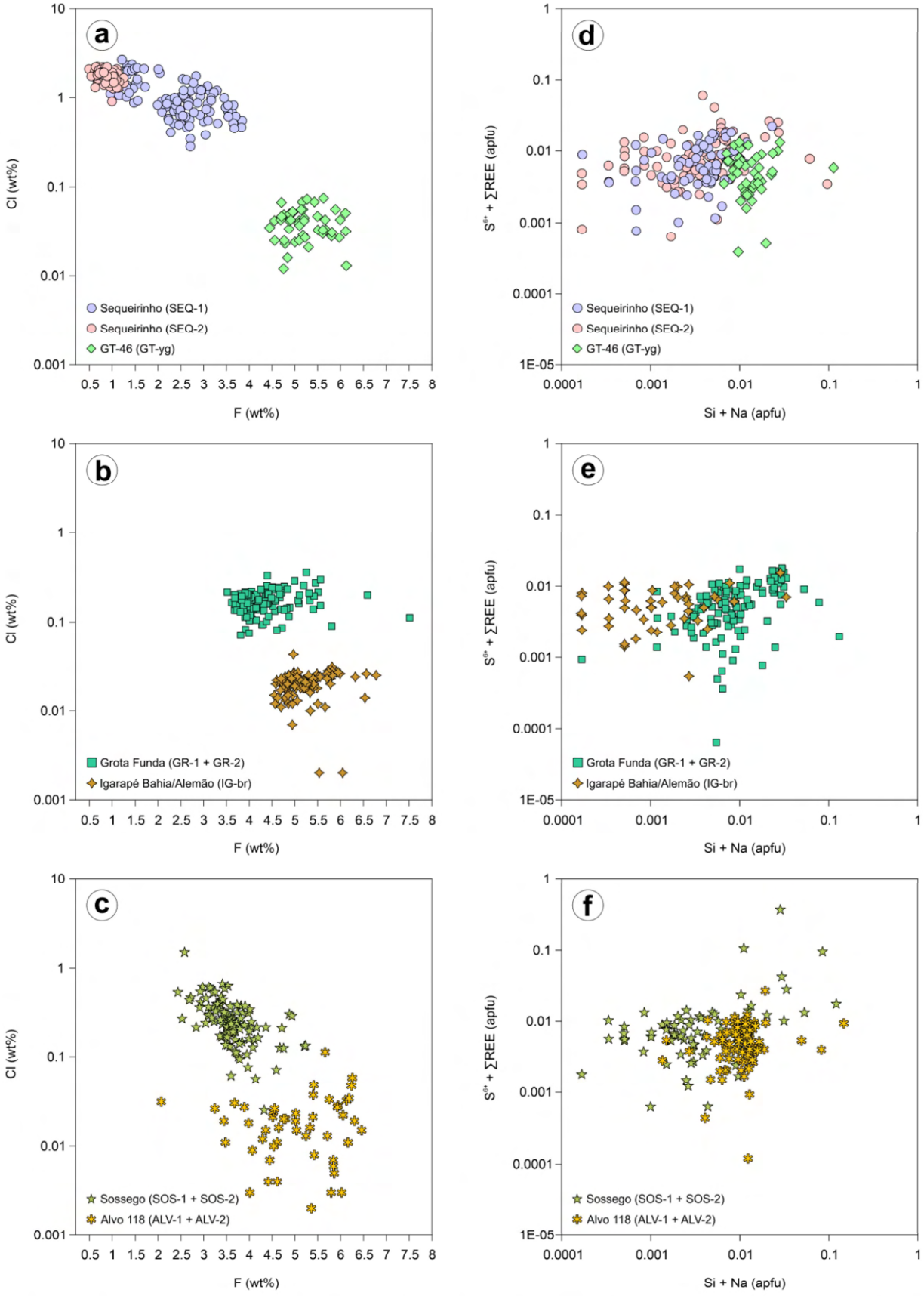

Fig. 12. Divalent plots of (a) to (c) Cl vs. F and (d) to (f) S^{6+} + (REE + Y) vs. Si + Na for apatite at Carajás.

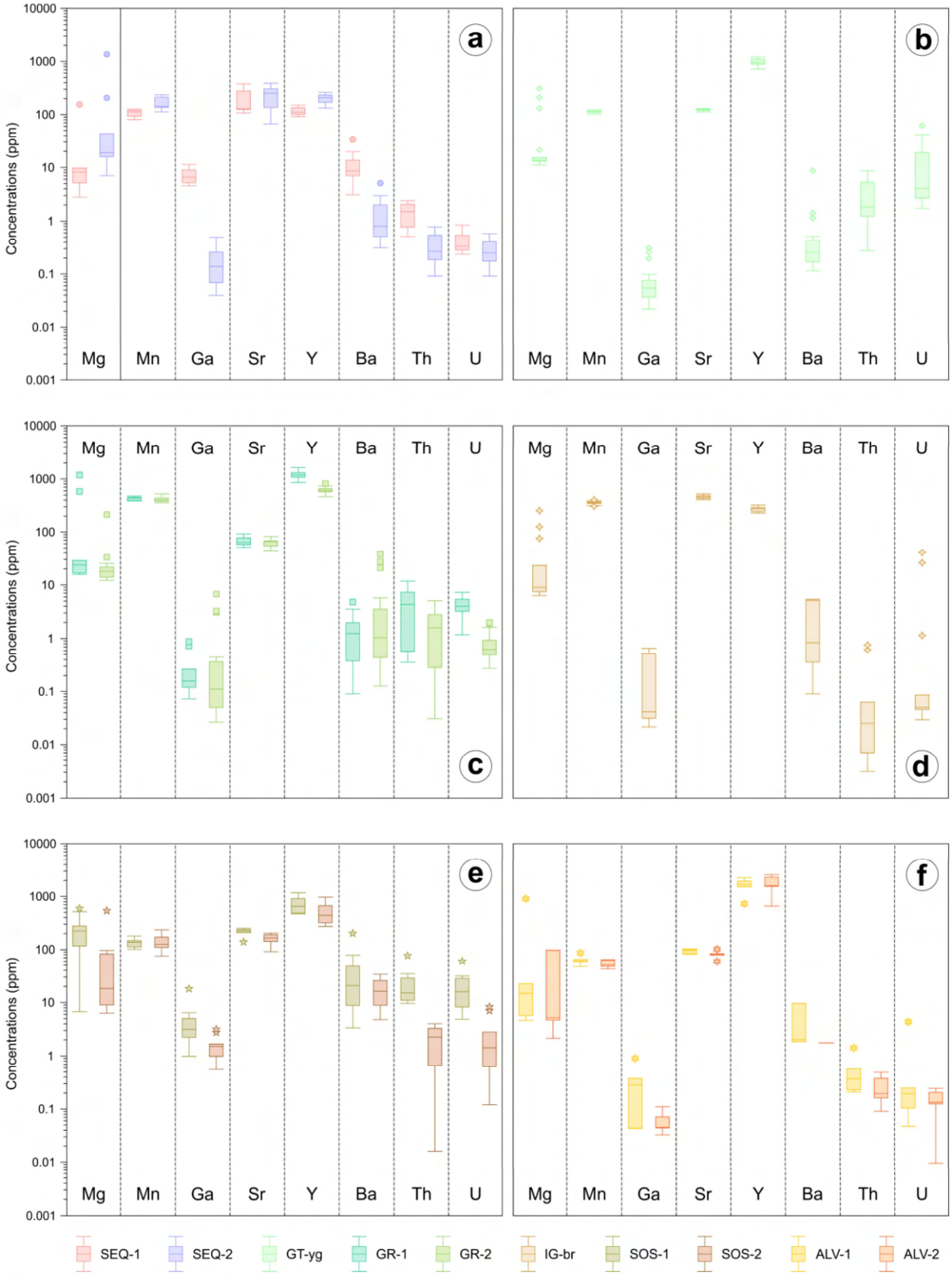

Fig. 13. Comparative box plots displaying compositions of representative trace elements in apatite from the IOCG deposits of Carajás. Sample sizes smaller than five were not considered for plotting due to the lack of statistical representativeness. Boxes identify the interquartile range (IQR) and outliers fall above or below quartiles ± 1.5 IQR.

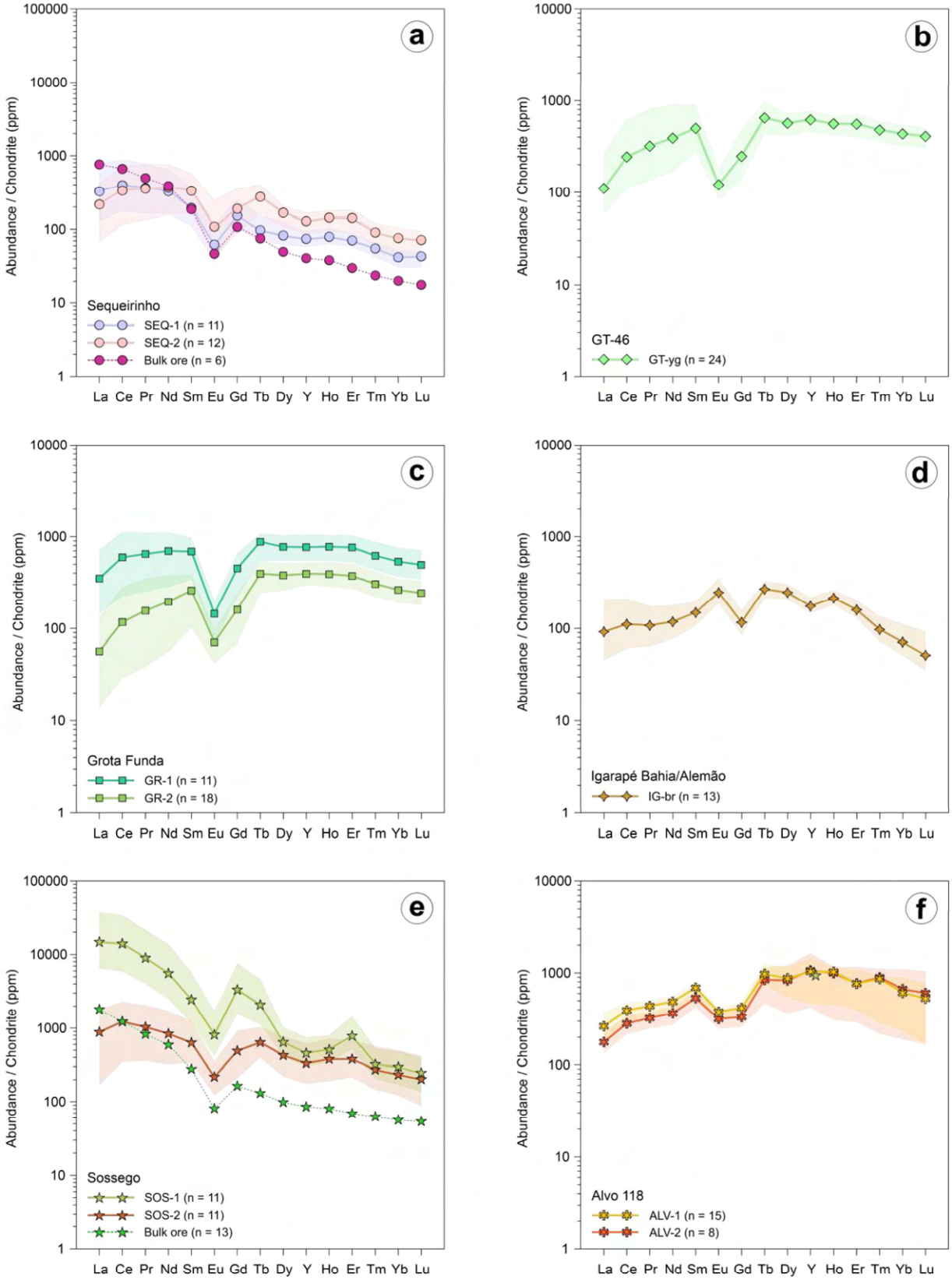

Fig. 14. Chondrite-normalized REE plots for analysed apatite grains from the (a) Sequeirinho, (b) GT-46, (c) Grota Funda, (d) Igarapé Bahia/Alemão, (e) Sossego, and (f) Alvo 118 IOCG deposits. All lines represent average values for each apatite variety and shaded regions denote

their REE + Y distribution pattern. Chondrite normalization values are from McDonough and Sun (1995). Bulk ore values for the Sequeirinho and Sossego orebodies are from Carvalho (2009).

Table 5 Summary of apatite cathodoluminescence features and main chemical attributes

Deposit / Orebody name	Apatite abbreviation	Cathodoluminescence features	Main chemical attributes
Sequeirinho	SEQ-1	Orange luminescence	Hydroxyapatite with negative Eu anomaly and LREE enrichment
	SEQ-2	Orange luminescence	OH- to F-rich apatite with negative Eu anomaly and LREE enrichment
GT-46	GT-yg	Yellowish-green luminescence	Fluorapatite with negative Eu anomaly, HREE enrichment and high Y contents
Grota Funda	GR-1	Purplish luminescence	Fluorapatite with negative Eu anomaly, HREE enrichment
	GR-2	Yellowish-green luminescence	Fluorapatite with negative Eu anomaly and HREE enrichment and high Mn contents
Igarapé-Bahia/Alemão	IG-br	Brownish luminescence	Fluorapatite with positve Eu anomaly, MREE enrichment and high Sr contents
Sossego	SOS-1	Purplish luminescence	Fluorapatite with negative Eu anomaly and LREE enrichment
	SOS-2	Brownish-yellow luminescence	Fluorapatite with negative Eu anomaly and LREE enrichment
Alvo 118	ALV-1	Bluish luminescence	Fluorapatite with negative Eu anomaly, HREE enrichment and high Y contents
	ALV-2	Greyish luminescence	Fluorapatite with negative Eu anomaly, HREE enrichment and high Y contents

6. Discussions

6.1. Secondary REE-bearing minerals associated with apatite and their mechanisms of formation

Detailed petrographic studies and SEM-EDS analyses conducted in this research have revealed that monazite, allanite, and xenotime are commonly found as inclusions, along grain rims, or within internal fractures in apatite from most of the deposits here investigated. Experimental studies have confirmed that fluid-induced precipitation of monazite and xenotime inclusions in apatite can happen under a wide range of P–T conditions (300–900 ºC

and 500–1000 MPa), usually as a result of coupled dissolution-reprecipitation (CDRP) processes regulated by metasomatic alteration (Harlov, 2015; Harlov et al., 2005; Putnis, 2009). In general, such chemical processes are defined by the replacement of a mineral phase that had previously interacted with a reactant fluid, and subsequently reprecipitated with a different composition or eventually originated a completely distinct phase (Putnis, 2009, 2002). As a consequence of coupled dissolution–reprecipitation in apatite, original REE-rich regions that were affected by the reaction front give place to reprecipitated REE-depleted domains (Harlov et al., 2005), as clearly evidenced by comparing CL images and trace element data between the GR-1 and GR-2 (**Fig. 9b–c** and **14c**) as well as between the SOS-1 and SOS-2 apatites **(Fig. 10b** and **14e**). Furthermore, these REE-depleted regions are typically characterized by an interconnected net of nano- to microscale pores that facilitate fluid infiltration through the metasomatized apatite, thus aiding mass transfer of REE and other trace elements that can be readily incorporated into secondary REE-bearing phases (Harlov et al., 2005). Indeed, monazite inclusions are extremely abundant in apatite from the Sossego orebody and most commonly associated with nucleation sites at REE-depleted regions within the SOS-2 apatite (**Fig. 10c**). At Sequeirinho, on the other hand, the observed monazite inclusions are seemingly associated with exceptionally porous zones within the SEQ-1 apatite (**Fig. 7b**).

Allanite overgrowths on apatite, occasionally exhibiting reaction textures with monazite, are a striking feature recognized in the SEQ-2, GR-2, and GT-yg apatite rims (**Fig. 7f**, **8d** and **9e**). According to Budzyń et al. (2011), allanite formation can be triggered by the destabilization of monazite in the presence of a F-rich reactant fluid with high-Ca activities. This is in accordance with fluid inclusion data for late vein-type quartz at Sequeirinho and ore-related apatite from the Grota Funda deposit, that suggest the participation of fluids compositionally close to the $CaCl_2$–NaCl–H_2O system (Carvalho, 2009; Hunger et al., 2018). Alternatively, allanite precipitation at GT-46 could possibly have been triggered by fluid-mediated reactions involving monazite and neighboring silicate minerals (e.g., hornblende).

In brief, it is proposed that significant LREE leaching must have occurred during hydrothermal alteration of apatite in the abovementioned deposits. Part of these leached LREE would have been reincorporated by newly formed, secondary REE-bearing phases, such as monazite and allanite, which are preferentially associated with altered domains within the studied apatite grains.

6.2. Constraints on the redox state of the Carajás' IOCG deposits

Investigating the redox conditions of hydrothermal fluids is particularly important to understand the evolution of mineral systems since they represent one of the key factors that control the solubility of chemical components, the speciation of ligands responsible for metal transport and complexation, and even ore precipitation and remobilization processes (Mercer et al., 2020). In this sense, apatite chemical compositions have been largely utilized to evaluate the oxidation state of magmas and ore systems, due to its capability to host significant amounts of redox-sensitive elements such as Mn, Eu, S, Ce, and Ga (Belousova et al., 2002; Cao et al., 2012; Konecke et al., 2017; Mercer et al., 2020; Pan et al., 2016; Streck and Dilles, 1998). However, it is important to point out that apatite oxybarometers that are solely based on single element content variations (e.g., Mn-in-apatite; Miles et al., 2014) are relatively limited in application, considering that compositional shifts in apatite are not exclusively governed by redox conditions, but also by other parameters including pressure, temperature, and fluid compositions. As a result, the combined variation of two multi-valence elements with contrasting partitioning behaviors into apatite (e.g. Eu, Ce and Ga), depending on changes in the oxidation state, represents a much more reliable approach to evaluating the redox conditions of magmatic-hydrothermal systems (Mercer et al., 2020; Pan et al., 2016).

In a general way, apatite favors the incorporation of ions with the same valence or whose ionic radii are compatible in size with that of Ca^{2+} (Pan and Fleet, 2002). Thus, Ce^{3+}, $Eu^{3+,}$ and Ga^{2+} tend to be preferentially incorporated through coupled substitutions, over Eu^{2+}, $Ce^{4+,}$ and Ga^{3+}. In this sense, and considering that reducing fluids are relatively depleted in Eu^{3+} but, oppositely, more enriched in Ga^{2+} and Ce^{3+}, it is expected that apatite crystallized from such fluids exhibit relatively lower Eu and higher Ce and Ga contents when compared to those formed under oxidizing conditions (Cao et al., 2012; Pan et al., 2016).

According to Eu/Eu* and Ce/Ce* ratios of apatite grains investigated in this study, moderately reduced conditions seemingly prevailed during the crystallization of the SEQ-1 apatite within Na-Ca-altered zones of the Sequeirinho orebody, whereas moderately oxidizing conditions probably contributed to the formation of the ore-related, SEQ-2 apatite (**Fig. 15a**). This is further corroborated by the Ga contents in these two apatite varieties, which also indicate that the SEQ-2 apatite crystalized at higher fO_2 than SEQ-1 (**Fig. 15b**). Moderately reduced conditions have also apparently controlled the precipitation of the GT-yg, GR-1, and SOS-1 apatites (**Fig. 15a**, **c**, and **e**). Thus, a shift towards moderate oxidation levels is likely to have occurred while the GR-2 and SOS-2 apatites were being developed, as indicated by Eu/Eu* ratios and Ga concentrations (**Fig. 15c–f**). In the Alvo 118 deposit, on the other hand, the ALV-1 apatite supposedly precipitated under moderately oxidized

conditions, whereas the ALV-2 apatite was possibly originated in a dominant oxidized environment, which has also regulated the formation of fluorapatite (IG-br) at Igarapé Bahia/Alemão (**Fig. 15c–f**).

These results are in accordance with the general tendency shown by chalcopyrite magnetite-dominant IOCG systems worldwide, which are generally categorized as intermediate-redox or relatively reduced Cu-Au systems mainly depending on the abundance of key Fe-sulfide (e.g., pyrite, pyrrhotite) Fe-oxide (e.g., magnetite, hematite) minerals in the hydrothermal and ore assemblages (Skirrow, 2022). In fact, variable proportions of pyrrhotite and/or pyrite are found within the ore zones of the Sequeirinho, GT-46, Grota Funda, and Sossego deposits (Hunger et al., 2018; Monteiro et al., 2008a; Toledo et al., 2019), thus justifying the fO_2 conditions from which the SEQ-1, GT-yg, GR-1 and SOS-1 apatites crystallized in these deposits. On the other hand, the occurrence of hematite in association with chalcopyrite and apatite in the ore zones of the Alvo 118 deposit (Torresi et al., 2012) would explain the moderately oxidized conditions that governed the ALV-1 apatite formation. Later interaction with relatively more oxidizing fluids would have led to the small, but noticeable, shift towards higher fO_2 conditions during the precipitation of the SEQ-2, GR-2, ALV-2, and SOS-2 apatites at Sequeirinho, Grota Funda, Alvo 118, and Sossego, respectively. These fluids are likely the main responsible for the formation of hematite-rich hydrothermal assemblages in the late stages of the ore system evolution in the Sequeirinho, Alvo 118, and Sossego deposits (Monteiro et al., 2008a; Torresi et al., 2012), as well as for the late replacement of chalcopyrite by bornite in the main brecciated ore zone at Grota Funda (Hunger et al., 2018).

Finally, the dominant oxidizing conditions registered during the formation of fluorapatite at Igarapé Bahia/Alemão are somewhat intriguing, given the complete absence of hematite in the deposit hydrothermal and ore assemblages. Therefore, the relatively high Eu/Eu* ratios shown by ore-related apatite in the Igarapé Bahia deposit could not be necessarily reflecting its precipitation from a highly oxidizing fluid but instead the ready incorporation of Eu^{2+} into apatite in this case, despite its preference for Eu^{3+} (Rakovan et al., 2001).

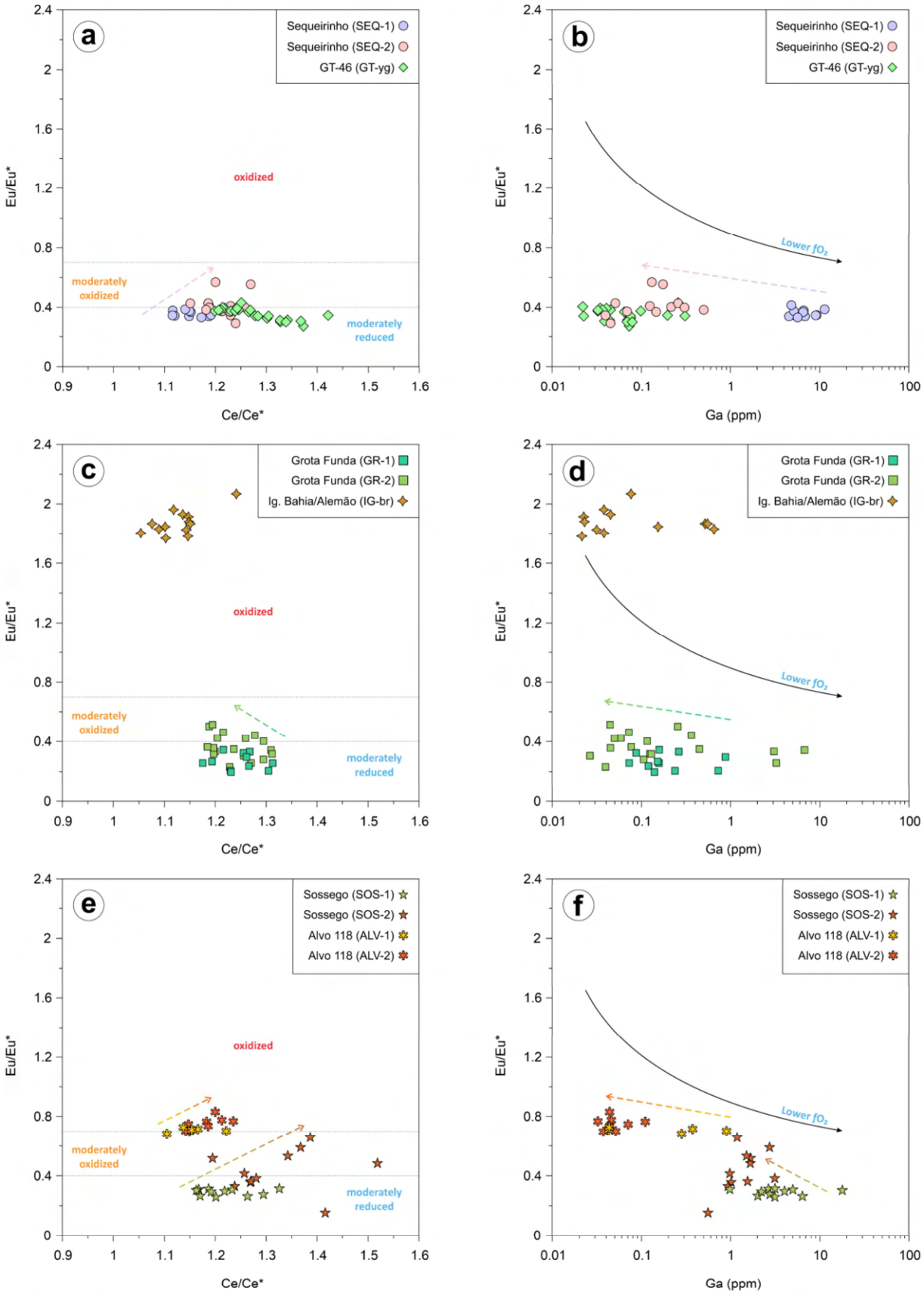

Fig. 15. (a), (c), and (e) Divalent plots of Ce/Ce* vs. Eu/Eu* for the analysed apatite grains. Discriminative fields are from Cao et al. (2012). (b), (d), and (f) Ga vs. Eu/Eu* biplots.

6.3. Apatite textural and compositional variations and their implications for the evolution of hydrothermal fluids in the investigated deposits

EPMA and LA-ICP-MS data of apatite have demonstrated significant compositional variations among samples from distinct IOCG deposits of the CD, especially in what concerns key transition elements and their REE chemical signatures. For instance, the incorporation of REE and Y into apatite are most commonly charge-balanced through the following coupled substitution mechanisms: (i) $Si^{4+} + (REE + Y)^{3+} = Ca^{2+} + P^{5+}$; (ii) $S^{6+} + (REE + Y)^{3+} + Si^{4+} + Na^{+} = 2Ca^{2+} + 2P^{5+}$; (iii) $(REE + Y)^{3+} + Na^{+} = 2Ca^{2+}$ (Pan and Fleet, 2002; Parat et al., 2002). Thus, the evident lack of positive correlation between Si + Na and S^{6+} + ΣREE + Y (**Fig. 12b**, **d** and **f**), combined with the Na-poor nature of all apatite analyzed in this study, represent strong indications that additional complex coupled substitutions must have occurred in the M cationic and ZO_4 tetrahedral sites to account for the REE and other trace element abundances in these apatite grains.

In hydrothermal systems such as those associated with the genesis of IOCG and iron-oxide apatite (IOA) deposits worldwide, substantial variations of REE and other trace elements within an individual apatite grain are generally a consequence of post-crystallization modifications (e.g., coupled dissolution-reprecipitation) promoted by fluid metasomatism (Harlov, 2015; Li and Zhou, 2015; Liao et al., 2022; Mercer et al., 2020; Zeng et al., 2016). These modifications are not only chemically evident but also reflected in complex textural attributes that are commonly revealed by BSE and CL imaging, as shown in this work and several other case studies, and which are currently being used to track the evolution of hydrothermal processes in mineral systems (Bouzari et al., 2016; Decrée et al., 2020; Liao et al., 2022; Mercer et al., 2020).

Recent studies have demonstrated that concentrations of REE, Sr, and Y can be used to petrogenetically distinguish apatite samples into three main categories (Li et al., 2022; O'Sullivan et al., 2020): magmatic, metamorphic/granitic, and hydrothermal CDRP. In a general way, magmatic apatite tends to be enriched in LREE and demonstrate high $(La/Yb)_N$ and Sr/Y ratios (>10), whereas hydrothermal apatite is comparatively low in REE and, hence, exhibits lower $(La/Yb)_N$ and $(La/Sm)_N$ (Broom-Fendley et al., 2016; Lu et al., 2021; Mercer et al., 2020). On a Sr/Y vs. LREE diagram, all apatite samples analysed in this study show a dominant hydrothermal signature compatible with CDRP mechanisms, except for the SOS-1 apatite which indicates to be magmatic in origin (**Fig. 16a–c**). Similarly, on a $(La/Yb)_N$ and $(La/Sm)_N$ biplot, the SOS-1 apatite falls mostly within the magmatic field, whereas fluid-

driven, hydrothermal processes seem to have controlled the precipitation of the remaining apatite samples (**Fig. 16d–f**).

In the Sequeirinho orebody, ore-related fluorapatite (SEQ-2) is undoubtedly more enriched in total REE + Y contents and has higher Sr/Y, $(La/Yb)_N$, and $(La/Sm)_N$ ratios in relation to that associated with Na-Ca alteration zones (SEQ-1), which is oppositely OH- and Cl-richer (**Fig. 11, 12a, 16a** and **d**). Therefore, we propose that a progressive decrease of chlorine contents in the hydrothermal fluid responsible for the precipitation of the SEQ-1 apatite, could have been triggered by mixing with F-rich fluids during the onset of ore precipitation in the deposit, thus leading to the formation of the SEQ-2 apatite. A similar interpretation has been raised to explain the chlorine-poor nature of amphibole crystals within the ore zones (i.e., actinolite/Fe-actinolite) of the Sequeirinho orebody, relative to those associated with Na-Ca-altered domains (Fe-edenite/hastingsite; Monteiro et al., 2008b). Additionally, fluid inclusion data supports a fluid mixing model as the main mechanism governing the precipitation of the ore assemblage at Sequeirinho (Carvalho, 2009; Monteiro et al., 2008b).

Apatite in the GT-46 (GT-yg) and Grota Funda (GR-1 and GR-2) deposits have evidenced noticeable HREE-enriched fractionation patterns (**Fig. 14b–c**). Relatively high HREE abundances in apatite is usually the result of preferential leaching of LREE from early formed apatite, leading to the precipitation of a HREE-enriched metasomatic apatite characterized by low $(La/Yb)_N$ ratios (Broom-Fendley et al., 2016; Harlov, 2015; Li et al., 2022). In this sense, the HREE-enriched signature shown by the GT-yg and GR-2 apatites most likely reflects the hydrothermal remobilization of LREE away from primary domains (GT-bl [?] and GR-1, respectively), which could have been later reincorporated by allanite overgrowths, as previously discussed. Moreover, and although relatively speculative due to the lack of chemical data on the GT-bl apatite, it could represent remnants of pristine metamorphic apatite grains that subsequently interacted with hydrothermal fluids to form the GT-yg apatite (**Fig. 16a**). This hypothesis is reasonable considering the upper amphibolite facies metamorphism that had affected the host rocks of the deposit (Toledo et al., 2019). In fact, recent chemical data on apatite from the host G2 granite of the GT-46 deposit suggest that the apatite rim regions ($G2_{rim}$) could have been either formed by the interaction of early precipitated magmatic apatite ($G2_{core}$) with metamorphic or hydrothermal fluids (**Fig.16a**; Diniz et al., 2023).

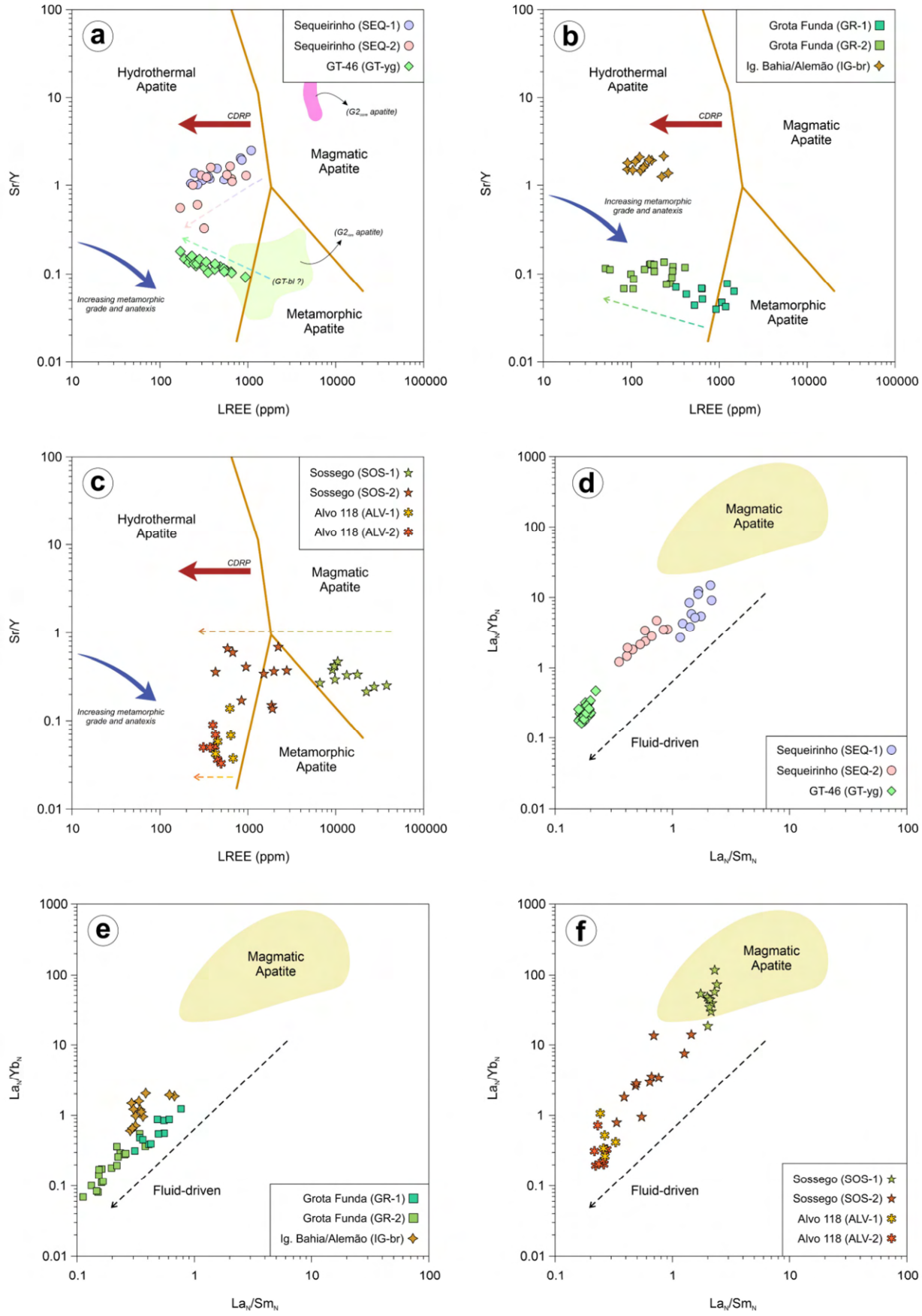

Fig. 16. (a), (b), and (c) Divalent plots of LREE vs. Sr/Y (modified after O'Sullivan et al., 2020). (d), (e), and (f) Binary plots of La_N/Sm_N vs. La_N/Yb_N. Data on magmatic apatite are

from Brassinnes et al. (2005), Chakhmouradian et al. (2017), Chen and Simonetti (2013), Ladenburger et al. (2016), Lu et al. (2021), Su et al. (2021), Xu et al. (2010), Zhang et al. (2019), and references therein.

Hydrothermal fluorapatite at Igarapé Bahia/Alemão (IG-br) has a unique chondrite-normalized REE + Y fractionation pattern in comparison to the other investigated deposits, which is marked by clear MREE enrichment and positive Eu anomalies (**Fig. 14d**). Such chemical behavior is particularly uncommon in apatite and thus far only reported for samples from orogenic-Au deposits (Brugger et al., 2008; Mao et al., 2016) and IOCG systems within the Olympic Dam (Krneta et al., 2017a) and Kangdian (Li and Zhou, 2015; Liao et al., 2022) metallogenic districts. According to several authors, crystallization from fluids enriched in Eu relative to other REE due to the sericitization of feldspars could represent a possible explanation for the observed positive Eu anomalies (Krneta et al., 2017a; Mao et al., 2016). However, sericite formation is notably unexpressive at Igarapé Bahia/Alemão (Melo et al., 2019a) and, therefore, is unlikely to have substantially contributed to the breakdown of feldspars from host rocks and the consequent release of REE into migrating hydrothermal fluids. Alternatively, the MREE enrichment and positive Eu anomalies could have been the result of apatite crystallization from alkaline, CO_2-rich hydrothermal fluids, as suggested for the Olympic Dam deposit and Wirrda Well and Acropolis prospects (Krneta et al., 2017a, 2017b). Indeed, geochemical and fluid inclusion data indicate the participation of CO_2-CH_4-bearing and low-salinity fluids during ore precipitation at Igarapé Bahia/Alemão (Dreher et al., 2008). According to Melo et al. (2019), these fluids would have interacted with metalliferous brines possibly exsolved from highly fractionated A-type, peralkaline granites (e.g., Old Salobo) formed at 2.57 Ga in the CD.

Pronounced LREE contents (>37000 ppm) combined with high $(La/Yb)_N$ ratios (up to 13.93) point to a magmatic origin for the SOS-1 fluorapatite from the Na-Ca alteration zone of the Sossego orebody (**Fig. 16c** and **d**). The participation of magmatic fluids in the evolution of the IOCG deposits of Carajás has been suggested by several lines of evidence (e.g., fluid inclusion and isotope data; Chiaradia et al., 2006; Hunger et al., 2018; Melo et al., 2019b; Monteiro et al., 2008a; Toledo et al., 2019), although a genetic link between IOCG genesis and coeval magmatism in the CD is still highly debatable. At Sossego, the involvement of magmatic fluids during the development of early hydrothermal alteration assemblages (i.e., sodic, sodic-calcic, potassic) is somewhat ambiguous, although indicated by stable O isotope data. According to Monteiro et al. (2008a), high-temperature (~400ºC), ^{18}O-

enriched fluids ($\delta^{18}O_{H2O}$ = 3.7±1.5) dominated during apatite formation in Na-Ca-altered zones of the Sossego deposit, and could represent either primary magmatic waters or low-temperature formational/metamorphic fluids. Additionally, Cl/Br ratios (742–1786) and $\delta^{37}Cl$ values (0.25–1.53) obtained for fluid inclusions in quartz also suggest that at least part of the high-temperature, hypersaline fluids associated with the early stages of hydrothermal activity at Sossego could be linked to a mantle-derived, magmatic source (Chiaradia et al., 2006). Nevertheless, the clear decrease in LREE and $(La/Yb)_N$ ratios demonstrated by the SOS-2 apatite relative to the SOS-1 apatite (**Fig. 16c**) could be attributed to the mobilization of LREE due to superimposed hydrothermal alteration (e.g., potassic, carbonatization), in this case probably associated with Cl-rich fluids, as suggested by mineral chemistry and fluid inclusion data (Carvalho, 2009; Monteiro et al., 2008b).

Ore-related fluorapatite varieties from the Alvo 118 deposit (ALV-1 and ALV-2) are hydrothermal in origin (**Fig. 16c** and **f**) and have showed marked left-sloping REE fractionation patterns, characteristic of a HREE enrichment (**Fig. 14f**). The cause of such enrichment is uncertain, although one possible explanation would be the involvement of originally HREE-rich hydrothermal fluids controlling apatite precipitation during ore formation. At Alvo 118, chlorine-rich, highly saline fluids (>30 wt.% NaCl eq.) have been interpreted as the main responsible for metal transport during the early stages of hydrothermal activity in the deposit (Torresi et al., 2012). Under hydrothermal conditions, Cl^- has been proven to be one of the most efficient ligands able to form REE complexes (Tropper et al., 2011; Williams-Jones et al., 2012), which would eventually destabilize during rapid precipitation of apatite in a cooling system (Louvel et al., 2015; Migdisov and Williams-Jones, 2014). Indeed, fluid inclusion data for the Alvo 118 ore breccia indicate that the interaction of the Cl-rich brines with a relatively diluted and cooler fluid would have triggered ore precipitation, possibly contributing to early apatite formation (Torresi et al., 2012). In this scenario, due to the relatively lower stability of HREE complexes relative to those with LREE (Broom-Fendley et al., 2017), their preferential destabilization could have caused the readily incorporation of HREE into the precipitated apatite at Alvo 118. Nevertheless, these observations are in accordance with the overall geochemical signature for the ore zone of the deposit, which is also characterized by high HREE contents, mainly due to the presence of a Be-B-HREE-rich gadolinite group mineral, besides apatite, in the ore assemblage (Torresi et al., 2012).

7. Conclusions

Apatite chemical and textural data of representative IOCG deposits from the CD allowed the following conclusions to be drawn:

(1) The observed compositional and morphological variations among apatite samples investigated in this study reflect the history of fluid-apatite interaction and the hydrothermal system evolution in each deposit. Processes that controlled the REE and other trace elements incorporation into apatite, as well as their internal remobilization (e.g., CDRP), were dominantly regulated by metasomatic activity associated with distinct fluid regimes that operated at a deposit scale, with no apparent relation with specific metallogenic epochs (Neoarchean vs. Paleoproterozoic).

(2) Eu/Eu*, Ce/Ce* and Ga values suggest that apatite formed under relatively distinct fO_2 at Carajás, from relatively reduced (Sequeirinho, GT-46, Grota Funda, and Sossego to more oxidized conditions (Alvo 118 and Igarapé Bahia). Late-formed apatite generations (i.e., SEQ-2, GR-2, ALV-2, and SOS-2 apatites) reflect the progressive interaction of primary apatite grains with highly oxidizing fluids in the final stages of hydrothermal activity in some of the studied deposits.

(3) Secondary REE-bearing phases such as monazite and allanite occur associated with hydrothermally altered domains within apatite grains from the majority of the investigated deposits and are the result of CDRP processes regulated by metasomatic activity. These processes were responsible for significant LREE leaching from primary apatite regions and its subsequent reincorporation by newly formed, secondary REE-rich minerals.

References

Almada, M. do C.O., Villas, R.N., 1999. O depósito Bahia: um possível exemplo de depósito de sulfeto vulcanogênico tipo Besshi arqueano em Carajás. Rev. Bras. Geociências 29, 579–592.

Almeida, J. de A.C. de, Dall'Agnol, R., de Oliveira, M.A., Macambira, M.J.B., Pimentel, M.M., Rämö, O.T., Guimarães, F.V., Leite, A.A. da S., 2011. Zircon geochronology, geochemistry and origin of the TTG suites of the Rio Maria granite-greenstone terrane: Implications for the growth of the Archean crust of the Carajás province, Brazil. Precambrian Res. 187, 201–221. https://doi.org/10.1016/j.precamres.2011.03.004

Almeida, J.A.C., Dall'Agnol, R., Dias, S.B., Althoff, F.J., 2010. Origin of the Archean leucogranodiorite-granite suites: Evidence from the Rio Maria terrane and implications for granite magmatism in the Archean. Lithos 120, 235–257. https://doi.org/10.1016/j.lithos.2010.07.026

Araújo Filho, R.C., Nogueira, A.C.R., Araújo, R.N., 2020. New stratigraphic proposal of a Paleoproterozoic siliciclastic succession: Implications for the evolution of the Carajás Basin, Amazonian craton, Brazil. J. South Am. Earth Sci. 102, 102665. https://doi.org/10.1016/j.jsames.2020.102665

Araújo, R., Nogueira, A., 2019. Serra sul diamictite of the carajas basin (Brazil): A paleoproterozoic glaciation on the amazonian craton. Geology 47, 1166–1170. https://doi.org/10.1130/G46923.1

Avelar, V.G., Lafon, J.M., Correia Jr., F.C., Macambira, E.M.B., 1999. O magmatismo arqueano da região de Tucumã - Província Mineral De Carajás: Novos resultados geocronológicos. Rev. Bras. Geociências 29, 453–460.

Barros, C.E.M., Macambira, M.J.B., Barbey, P., Scheller, T., 2004. Dados isotópicos Pb-Pb em zircão (evaporação) e Sm-Nd do Complexo Granítico Estrela, Província Mineral de Carajás, Brasil: Implicações petrológicas e tectônicas. Rev. Bras. Geociências 34, 531–538.

Barros, C.E.M., Sardinha, A.S., Macambira, M.J.B., Barbey, P., Boullier, A.-M., 2009. Structure, petrology, geochemistry and zircon U/Pb and Pb/Pb geochronology of the synkinematic archean (2.7 Ga) A-type granites from the Carajás Metallogenetic Province, northern Brazil. Can. Mineral. 47, 1423–1440. https://doi.org/10.3749/canmin.47.6.1423

Barton, M.D., 2014. Iron Oxide(-Cu-Au-REE-P-Ag-U-Co) Systems, in: Holland, H., Turkian, K. (Eds.), Treatise on Geochemistry: Second Edition. Elsevier Ltd., pp. 515–541. https://doi.org/10.1016/B978-0-08-095975-7.01123-2

Belousova, E.A., Griffin, W.L., O'Reilly, S.Y., Fisher, N.I., 2002. Apatite as an indicator mineral for mineral exploration: Trace-element compositions and their relationship to host rock type. J. Geochemical Explor. 76, 45–69. https://doi.org/10.1016/S0375-6742(02)00204-2

Bouzari, F., Hart, C.J.R., Bissig, T., Barker, S., 2016. Hydrothermal Alteration Revealed by Apatite Luminescence and Chemistry: A Potential Indicator Mineral for Exploring Covered Porphyry Copper Deposits. Econ. Geol. 11, 1397–1410.

Brassinnes, S., Balaganskaya, E., Demaiffe, D., 2005. Magmatic evolution of the differentiated ultramafic, alkaline and carbonatite intrusion of Vuoriyarvi (Kola Peninsula, Russia). A LA-ICP-MS study of apatite. Lithos 85, 76–92. https://doi.org/10.1016/j.lithos.2005.03.017

Broom-Fendley, S., Brady, A.E., Wall, F., Gunn, G., Dawes, W., 2017. REE minerals at the Songwe Hill carbonatite, Malawi: HREE-enrichment in late-stage apatite. Ore Geol. Rev. 81, 23–41. https://doi.org/10.1016/j.oregeorev.2016.10.019

Broom-Fendley, S., Styles, M.T., Appleton, J.D., Gunn, G., Wall, F., 2016. Evidence for dissolution-reprecipitation of apatite and preferential LREE mobility in carbonatite-derived late-stage hydrothermal processes. Am. Mineral. 101, 596–611. https://doi.org/10.2138/am-2016-5502CCBY

Brugger, J., Etschmann, B., Pownceby, M., Liu, W., Grundler, P., Brewe, D., 2008. Oxidation state of europium in scheelite: Tracking fluid-rock interaction in gold deposits. Chem. Geol. 257, 26–33. https://doi.org/10.1016/j.chemgeo.2008.08.003

Budzyń, B., Harlov, D.E., Williams, M.L., Jercinovic, M.J., 2011. Experimental determination of stability relations between monazite, fluorapatite, allanite, and REE-

epidote as a function of pressure, temperature, and fluid composition. Am. Mineral. 96, 1547–1567. https://doi.org/10.2138/am.2011.3741

Cao, M., Li, G., Qin, K., Seitmuratova, E.Y., Liu, Y., 2012. Major and trace element characteristics of apatites in granitoids from central Kazakhstan: Implications for petrogenesis and mineralization. Resour. Geol. 62, 63–83. https://doi.org/10.1111/j.1751-3928.2011.00180.x

Carvalho, E.R., 2009. Caracterização geológica e gênese das mineralizações de óxido de Fe-Cu-Au e metais associados na Província Mineral de Carajás: Estudo de caso do depósito de Sossego. University of Campinas.

Chakhmouradian, A.R., Reguir, E.P., Zaitsev, A.N., Couëslan, C., Xu, C., Kynický, J., Mumin, A.H., Yang, P., 2017. Apatite in carbonatitic rocks: Compositional variation, zoning, element partitioning and petrogenetic significance. Lithos 274–275, 188–213. https://doi.org/10.1016/j.lithos.2016.12.037

Chen, W., Simonetti, A., 2013. In-situ determination of major and trace elements in calcite and apatite, and U-Pb ages of apatite from the Oka carbonatite complex: Insights into a complex crystallization history. Chem. Geol. 353, 151–172. https://doi.org/10.1016/j.chemgeo.2012.04.022

Chiaradia, M., Banks, D., Cliff, R., Marschik, R., Haller, A., 2006. Origin of fluids in iron oxide-copper-gold deposits: Constraints from $\delta^{37}Cl$, $^{87}Sr/^{86}Sr$ and Cl/Br. Miner. Depos. 41, 565–573. https://doi.org/10.1007/s00126-006-0082-6

Cole, D.R., Chakraborty, S., 2001. Rates and mechanisms of isotopic exchange. Rev. Mineral. Geochemistry 43, 83–223. https://doi.org/10.1515/9781501508745-005

Cordani, U.G., Teixeira, W., 2007. Proterozoic accretionary belts in the Amazonian Craton. Mem. Geol. Soc. Am. 200, 297–320. https://doi.org/10.1130/2007.1200(14)

Costa UAP, Paula RR, Silva DPB et al. (2016) Programa Geologia do Brasil-PGB – Mapa de integração geológico-geofísica da ARIM Carajás. Escala 1:250.000. CPRM, Belém

Dardenne, M.A., Ferreira Filho, C.F., Meirelles, M.R., 1988. The role of shoshonitic and calc-alkaline suites in the tectonic evolution of the Carajás District, Brazil. J. South Am. Earth Sci. 1, 363–372. https://doi.org/10.1016/0895-9811(88)90023-5

Decrée, S., Cawthorn, G., Deloule, E., Mercadier, J., Frimmel, H., Baele, J.M., 2020. Unravelling the processes controlling apatite formation in the Phalaborwa Complex (South Africa) based on combined cathodoluminescence, LA-ICPMS and in-situ O and Sr isotope analyses, Contributions to Mineralogy and Petrology. Springer Berlin Heidelberg. https://doi.org/10.1007/s00410-020-1671-6

Diniz, A.C., Melo, G.H.C., Lana, C. de C., Queiroga, G.N., Castro, M.P. de, Reis, H.L.S., 2023. Unravelling magmatic-hydrothermal processes at Salobo and GT-46 IOCG deposits, Carajás mineral province, Brazil: Constraints from whole-rock geochemistry and trace elements in apatite. J. South Am. Earth Sci. 125, 104290. https://doi.org/10.1016/j.jsames.2023.104290

DOCEGEO, 1988. Revisão litoestratigráfica da Província Mineral de Carajás - Litoestratigrafia e principais depósitos minerais, in: XXXV Congresso Brasileiro de Geologia. SBG, Belém, pp. 11–54.

Dreher, A.M., Xavier, R.P., Taylor, B.E., Martini, S.L., 2008. New geologic, fluid inclusion and stable isotope studies on the controversial Igarapé Bahia Cu-Au deposit, Carajás

Province, Brazil. Miner. Depos. 43, 161–184. https://doi.org/10.1007/s00126-007-0150-6

Feio, G.R.L., Dall'Agnol, R., Dantas, E.L., Macambira, M.J.B., Gomes, A.C.B., Sardinha, A.S., Oliveira, D.C., Santos, R.D., Santos, P.A., 2012. Geochemistry, geochronology, and origin of the Neoarchean Planalto Granite suite, Carajás, Amazonian craton: A-type or hydrated charnockitic granites? Lithos 151, 57–73. https://doi.org/10.1016/j.lithos.2012.02.020

Feio, G.R.L., Dall'Agnol, R., Dantas, E.L., Macambira, M.J.B., Santos, J.O.S., Althoff, F.J., Soares, J.E.B., 2013. Archean granitoid magmatism in the Canaã dos Carajás area: Implications for crustal evolution of the Carajás province, Amazonian craton, Brazil. Precambrian Res. 227, 157–185. https://doi.org/10.1016/j.precamres.2012.04.007

Ferreira Filho, C.F., 1985. Geologia e Mineralizações Sulfetadas do Prospecto Bahia, Província Mineral de Carajás. University of Brasilia.

Ferreira Filho, C.F., Cançado, F., Correa, C., Macambira, E.M.B., Junqueira-Brod, T.C., Siepierski, L., 2007. Mineralizações estratiformes de PGE-Ni associadas a complexos acamadados em Carajás: os exemplos de Luanga e Serra da Onça, in: Rosa-Costa, L.T., Klein, E.L., Viglio, E.P. (Eds.), Contribuições à Geologia Da Amazônia. SBG-Núcleo Norte, Belém, pp. 1–14.

Figueiredo e Silva, R.C., Lobato, L.M., Zucchetti, M., Hagemann, S., Vennemann, T., 2020. Geotectonic signature and hydrothermal alteration of metabasalts under- and overlying the giant Serra Norte iron deposits, Carajás mineral Province. Ore Geol. Rev. 120. https://doi.org/10.1016/j.oregeorev.2020.103407

Gao, J.-F., Zhou, M.-F., Lightfoot, P.C., Wang, C.Y., Qi, L., Sun, M., 2013. Sulfide Saturation and Magma Emplacement in the Formation of the Permian Huangshandong Ni-Cu Sulfide Deposit, Xinjiang, Northwestern China. Econ. Geol. 108, 1833–1848.

Goldoff, B., Webster, J.D., Harlov, D.E., 2012. Characterization of fluor-chlorapatites by electron probe microanalysis with a focus on time-dependent intensity variation of halogens. Am. Mineral. 97, 1103–1115. https://doi.org/10.2138/am.2012.3812

Griffin, W.L., Powell, W.J., Pearson, N.J., O'Reilly, S.Y., 2008. Glitter: Data reduction software for laser ablation ICP-MS, in: Sylvester, P. (Ed.), Laser Ablation ICP-MS in the Earth Sciences: Current Practices and Outstanding Issues. Short Course Series, Volume 40. Mineralogical Association of Canada, pp. 308–311. https://doi.org/10.2113/gsecongeo.104.4.601

Harlov, D.E., 2015. Apatite: A fingerprint for metasomatic processes. Elements 11, 171–176. https://doi.org/10.2113/gselements.11.3.171

Harlov, D.E., Wirth, R., Förster, H.J., 2005. An experimental study of dissolution-reprecipitation in fluorapatite: Fluid infiltration and the formation of monazite. Contrib. to Mineral. Petrol. 150, 268–286. https://doi.org/10.1007/s00410-005-0017-8

Hughes, J.M., Rakovan, J.F., 2015. Structurally robust, chemically diverse: Apatite and apatite supergroup minerals. Elements 11, 165–170. https://doi.org/10.2113/gselements.11.3.165

Huhn, S.R.B., Macambira, M.J.B., Dall'Agnol, R., 1999. Geologia e geocronologia Pb-Pb do Granito Alcalino Planalto, Região da Serra do Rabo, Carajás-PA, in: VI Simpósio de Geologia Da Amazônia. SBG-Núcleo Norte, pp. 463–466.

Huhn, S.R.B., Nascimento, J.A.S., 1997. São os depósitos cupríferos de Carajás do tipo Cu-Au-U-ETR?, in: Costa, M.L., Angélica, R.S. (Eds.), Contribuições à Geologia Da Amazônia. SBG, Belém, pp. 143–160.

Hunger, R.B., Melo, G.H.C., Xavier, R.P., Moreto, C.P.N., Talavera, C., Su, Z.K., Zhao, X.F., 2021. The Santa Lúcia Cu-Au deposit, Carajás Mineral Province, Brazil: a Neoarchean (2.68 Ga) member of the granite-related copper-gold systems of Carajás. Miner. Depos. https://doi.org/10.1007/s00126-020-01034-z

Hunger, R.B., Xavier, R.P., Moreto, C.P.N., Gao, J.-F., 2018. Hydrothermal Alteration, Fluid Evolution, and Re-Os Geochronology of the Grota Funda Iron Oxide Copper-Gold Deposit, Carajás Province (Pará State), Brazil. Econ. Geol. 113, 1769–1794. https://doi.org/10.5382/econgeo.2018.4612

Jia, F., Zhang, C., Liu, H., Meng, X., Kong, Z., 2020. In situ major and trace element compositions of apatite from the Yangla skarn Cu deposit, southwest China: Implications for petrogenesis and mineralization. Ore Geol. Rev. 127, 103360. https://doi.org/10.1016/j.oregeorev.2020.103360

Jochum, K.P., Weis, U., Schwager, B., Stoll, B., Wilson, S.A., Haug, G.H., Andreae, M.O., Enzweiler, J., 2016. Reference Values Following ISO Guidelines for Frequently Requested Rock Reference Materials. Geostand. Geoanalytical Res. 40, 333–350. https://doi.org/10.1111/j.1751-908X.2015.00392.x

Justo, A.P., Dantas, E.L., Freitas-Silva, F.H., Rodrigues, J.B., 2018. Detrital zircon populations in the Neoarchean to Paleoproterozoic sedimentary coverage of Carajás, Amazon Craton, Brazil, in: 49o Congresso Brasileiro de Geologia. SBG, Rio de Janeiro, p. 1890.

Ketcham, R.A., 2015. Technical Note: Calculation of stoichiometry from EMP data for apatite and other phases with mixing on monovalent anion sites. Am. Mineral. 100, 1620–1623. https://doi.org/10.2138/am-2015-5171

Konecke, B.A., Fiege, A., Simon, A.C., Parat, F., Stechern, A., 2017. Co-variability of S^{6+}, S^{4+}, and S^{2-} in apatite as a function of oxidation state: Implications for a new oxybarometer. Am. Mineral. 102, 548–557. https://doi.org/10.2138/am-2017-5907

Kreidler, E., Hummel, F., 1970. The crystal chemistry of apatite: Structure fields of fluor-and chlorapatite. Am. Mineral. 55, 170–184.

Krneta, S., Ciobanu, C.L., Cook, N.J., Ehrig, K., Kontonikas-Charos, A., 2017a. Rare Earth Element Behaviour in Apatite from the Olympic Dam Cu–U–Au–Ag Deposit, South Australia. Minerals 7, 1–26. https://doi.org/10.3390/min7080135

Krneta, S., Cook, N.J., Ciobanu, C.L., Ehrig, K., Kontonikas-Charos, A., 2017b. The Wirrda Well and Acropolis prospects, Gawler Craton, South Australia: Insights into evolving fluid conditions through apatite chemistry. J. Geochemical Explor. 181, 276–291. https://doi.org/10.1016/j.gexplo.2017.08.004

Ladenburger, S., Marks, M.A.W., Upton, B., Hill, P., Wenzel, T., Markl, G., 2016. Compositional variation of apatite from rift-related alkaline igneous rocks of the Gardar Province, South Greenland. Am. Mineral. 101, 612–626. https://doi.org/10.2138/am-2016-5443

Li, J., Ye, C., Ying, J., 2022. In Situ Geochemical and Sr-Nd Isotope Analyses of Apatite from the Shaxiongdong Alkaline-Carbonatite Complex (South Qinling, China): Implications for magma evolution and mantle source. Minerals 12, 1–19.

Li, X., Zhou, M.F., 2015. Multiple stages of hydrothermal REE remobilization recorded in fluorapatite in the Paleoproterozoic Yinachang Fe-Cu-(REE) deposit, Southwest China. Geochim. Cosmochim. Acta 166, 53–73. https://doi.org/10.1016/j.gca.2015.06.008

Liao, W., Su, Z.K., Li, X.C., Zhang, C., Zhao, X.F., 2022. Cathodoluminescent, chemical and strontium isotopic characteristics of apatite from Lanniping Fe-Cu deposit, southwestern China: Implications for fluid evolution in IOCG systems. Ore Geol. Rev. 145, 104882. https://doi.org/10.1016/j.oregeorev.2022.104882

Liu, Y., Hu, Z., Gao, S., Günther, D., Xu, J., Gao, C., Chen, H., 2008. In situ analysis of major and trace elements of anhydrous minerals by LA-ICP-MS without applying an internal standard. Chem. Geol. 257, 34–43. https://doi.org/10.1016/j.chemgeo.2008.08.004

Louvel, M., Bordage, A., Testemale, D., Zhou, L., Mavrogenes, J., 2015. Hydrothermal controls on the genesis of REE deposits: Insights from an in situ XAS study of Yb solubility and speciation in high temperature fluids (T<400°C). Chem. Geol. 417, 228–237. https://doi.org/10.1016/j.chemgeo.2015.10.011

Lu, J., Chen, W., Ying, Y., Jiang, S., Zhao, K., 2021. Apatite texture and trace element chemistry of carbonatite-related REE deposits in China: Implications for petrogenesis. Lithos 398–399, 106276. https://doi.org/10.1016/j.lithos.2021.106276

Macambira, M.J.B., Vasquez, M.L., Silva, D.C.C. da, Galarza, M.A., Barros, C.E. de M., Camelo, J. de F., 2009. Crustal growth of the central-eastern Paleoproterozoic domain, SW Amazonian craton: Juvenile accretion vs. reworking. J. South Am. Earth Sci. 27, 235–246. https://doi.org/10.1016/j.jsames.2009.02.001

Machado, N., Lindenmayer, Z., Krogh, T.E., Lindenmayer, D., 1991. U-Pb geochronology of Archean magmatism and basement reactivation in the Carajás area, Amazon shield, Brazil. Precambrian Res. 49, 329–354. https://doi.org/10.1016/0301-9268(91)90040-H

Mao, M., Rukhlov, A.S., Rowins, S.M., Spence, J., Coogan, L.A., 2016. Apatite trace element compositions: A robust new tool for mineral exploration. Econ. Geol. 111, 1187–1222. https://doi.org/10.2113/econgeo.111.5.1187

Marangoanha, B., Oliveira, D.C. de, Dall'Agnol, R., 2019. The Archean granulite-enderbite complex of the northern Carajás province, Amazonian craton (Brazil): Origin and implications for crustal growth and cratonization. Lithos 350–351, 105275. https://doi.org/10.1016/j.lithos.2019.105275

Martins, P.L.G., Toledo, C.L.B., Silva, A.M., Chemale, F., Santos, J.O.S., Assis, L.M., 2017. Neoarchean magmatism in the southeastern Amazonian Craton, Brazil: Petrography, geochemistry and tectonic significance of basalts from the Carajás Basin. Precambrian Res. 302, 340–357. https://doi.org/10.1016/j.precamres.2017.10.013

McDonough, W.F., Sun, S. -s., 1995. The composition of the Earth. Chem. Geol. 120, 223–253.

Melo, G.H.C., Monteiro, L.V.S., Hunger, R.B., Toledo, P.I.F., Xavier, R.P., Zhao, X.F., Su, Z.K., Moreto, C.P.N., Jesus, S. dos S.G.P. de, 2021. Magmatic-hydrothermal fluids leaching older seafloor exhalative rocks to form the IOCG deposits of the Carajás Province, Brazil: Evidence from boron isotopes. Precambrian Res. 365, 106412. https://doi.org/10.1016/j.precamres.2021.106412

Melo, G.H.C., Monteiro, L.V.S., Xavier, R.P., Moreto, C.P.N., Arquaz, R.M., Silva, M.A.D., 2019a. Evolution of the Igarapé Bahia Cu-Au deposit, Carajás Province (Brazil): Early

syngenetic chalcopyrite overprinted by IOCG mineralization. Ore Geol. Rev. 111, 102993. https://doi.org/10.1016/j.oregeorev.2019.102993

Melo, G.H.C., Monteiro, L.V.S., Xavier, R.P., Moreto, C.P.N., Santiago, E., 2019b. Tracing Fluid Sources for the Salobo and Igarapé Bahia Deposits: Implications for the Genesis of the Iron Oxide Copper-Gold Deposits in the Carajás Province, Brazil. Econ. Geol. 114, 697–718. https://doi.org/10.5382/econgeo.4659

Melo, G.H.C., Monteiro, L.V.S., Xavier, R.P., Moreto, C.P.N., Santiago, E.S.B., Dufrane, S.A., Aires, B., Santos, A.F.F., 2016. Temporal evolution of the giant Salobo IOCG deposit, Carajás Province (Brazil): Constraints from paragenesis of hydrothermal alteration and U-Pb geochronology. Miner. Depos. 52, 709–732. https://doi.org/10.1007/s00126-016-0693-5

Mercer, C.N., Watts, K.E., Gross, J., 2020. Apatite trace element geochemistry and cathodoluminescent textures—A comparison between regional magmatism and the Pea Ridge IOAREE and Boss IOCG deposits, southeastern Missouri iron metallogenic province, USA. Ore Geol. Rev. 116, 103129. https://doi.org/10.1016/j.oregeorev.2019.103129

Migdisov, A.A., Williams-Jones, A.E., 2014. Hydrothermal transport and deposition of the rare earth elements by fluorine-bearing aqueous liquids. Miner. Depos. 49, 987–997. https://doi.org/10.1007/s00126-014-0554-z

Miles, A.J., Graham, C.M., Hawkesworth, C.J., Gillespie, M.R., Hinton, R.W., Bromiley, G.D., 2014. Apatite: A new redox proxy for silicic magmas? Geochim. Cosmochim. Acta 132, 101–119. https://doi.org/10.1016/j.gca.2014.01.040

Monteiro, L.V.S., Xavier, R.P., Carvalho, E.R., Hitzman, M.W., Johnson, C.A., Souza Filho, C.R., Torresi, I., 2008a. Spatial and temporal zoning of hydrothermal alteration and mineralization in the Sossego iron oxide–copper–gold deposit, Carajás Mineral Province, Brazil: paragenesis and stable isotope constraints. Miner. Depos. 43, 129–159. https://doi.org/10.1007/s00126-006-0121-3

Monteiro, L.V.S., Xavier, R.P., Hitzman, M.W., Juliani, C., Souza Filho, C.R., Carvalho, E. de R., 2008b. Mineral chemistry of ore and hydrothermal alteration at the Sossego iron oxide-copper-gold deposit, Carajás Mineral Province, Brazil. Ore Geol. Rev. 34, 317–336. https://doi.org/10.1016/j.oregeorev.2008.01.003

Moreto, C.P.N., Monteiro, L.V.S., Xavier, R.P., Amaral, W.S., dos Santos, T.J.S., Juliani, C., de Filho, C.R.S., 2011. Mesoarchean (3.0 and 2.86 Ga) host rocks of the iron oxide-Cu-Au Bacaba deposit, Carajás Mineral Province: U-Pb geochronology and metallogenetic implications. Miner. Depos. 46, 789–811. https://doi.org/10.1007/s00126-011-0352-9

Moreto, C.P.N., Monteiro, L.V.S., Xavier, R.P., Creaser, R.A., DuFrane, S.A., Melo, G.H.C., Silva, M.A.D., Tassinari, C.C.G., Sato, K., 2015a. Timing of multiple hydrothermal events in the iron oxide–copper–gold deposits of the Southern Copper Belt, Carajás Province, Brazil. Miner. Depos. 50, 517–546. https://doi.org/10.1007/s00126-014-0549-9

Moreto, C.P.N., Monteiro, L.V.S., Xavier, R.P., Creaser, R.A., DuFrane, S.A., Tassinari, C.C.G., Sato, K., Kemp, A.I.S., Amaral, W.S., 2015b. Neoarchean and paleoproterozoic iron oxide-copper-gold events at the Sossego deposit, Carajás Province, Brazil: Re-Os and U-Pb geochronological evidence. Econ. Geol. 110, 809–835. https://doi.org/10.2113/econgeo.110.3.809

Motta, J.G., Souza Filho, C.R. d., Carranza, E.J.M., Braitenberg, C., 2019. Archean crust and metallogenic zones in the Amazonian Craton sensed by satellite gravity data. Sci. Rep. 9, 1–10. https://doi.org/10.1038/s41598-019-39171-9

Mougeot, R., Respaut, J.P., Brique, L., Ledru, P., Milesi, J.P., Lerouge, C., Marcoux, E., Huhn, S.R.B., Macambira, M.J.B., 1996. Geochronological constraints for the age of the Águas Claras Formation (Carajás Province, Pará, Brazil), in: XXXIX Congresso Brasileiro de Geologia. SBG, Salvador, pp. 579–581.

Nathwani, C.L., Loader, M.A., Wilkinson, J.J., Buret, Y., Sievwright, R.H., Hollings, P., 2020. Multi-stage arc magma evolution recorded by apatite involcanic rocks. Geology 48, 323–327. https://doi.org/10.1130/G46998.1

O'Sullivan, G., Chew, D., Kenny, G., IIenrichs, I., Mulligan, D., 2020. The trace element composition of apatite and its application to detrital provenance studies. Earth-Science Rev. 201, 103044. https://doi.org/10.1016/j.earscirev.2019.103044

Oliveira, R.G. de, Teixeira, N.A., Costa, I.S.L., Tavares, F.M., Domingos, N.R.R., 2017. Levantamento aerogravimétrico Carajás - Contribuição a geotectônica e metalogenia da porção leste do Cráton Amazonas, in: XV Simpósio de Geologia Da Amazônia. SBG, Belém, pp. 251–254.

Pan, L.C., Hu, R.Z., Wang, X.S., Bi, X.W., Zhu, J.J., Li, C., 2016. Apatite trace element and halogen compositions as petrogenetic-metallogenic indicators: Examples from four granite plutons in the Sanjiang region, SW China. Lithos 254–255, 118–130. https://doi.org/10.1016/j.lithos.2016.03.010

Pan, Y., Fleet, M.E., 2002. Compositions of the apatite-group minerals: Substitution mechanisms and controlling factors. Rev. Mineral. Geochemistry 48, 13–50. https://doi.org/10.2138/rmg.2002.48.2

Parat, F., Dungan, M.A., Streck, M.J., 2002. Anhydrite, pyrrhotite, and sulfur-rich apatite: Tracing the sulfur evolution of an Oligocene andesite (Eagle Mountain, CO, USA). Lithos 64, 63–75. https://doi.org/10.1016/S0024-4937(02)00155-X

Pereira, R.M.P., Rosière, C.A., Santos, J.O.S., Lobato, L.M., Silva, R.C.F., McNaughton, N.J., 2009. Unidade Caninana: sequência clástica Paleoproterozóica revelada por datação U-Pb em zircões detríticos da Província Mineral Carajás, in: XI Simpósio de Geologia Da Amazônia. SBG, Manaus, pp. 376–379.

Piccoli, P.M., Candela, P.A., 2002. Apatite in igneous systems. Rev. Mineral. Geochemistry 48, 255–292. https://doi.org/10.213 8/rmg. 2002.48.6

Pidgeon, R.T., Macambira, M.J.B., Lafon, J.M., 2000. Th-U-Pb isotopic systems and internal structures of complex zircons from an enderbite from the Pium Complex, Carajás Province, Brazil: Evidence for the ages of granulite facies metamorphism and the protolith of the enderbite. Chem. Geol. 166, 159–171. https://doi.org/10.1016/S0009-2541(99)00190-4

Pinheiro, R.V.L., Holdsworth, R.E., 2000. Evolução tectonoestratigráfica dos sistemas transcorrentes Carajás e Cinzento, Cinturão Itacaiúnas, na borda leste do Cráton Amazônico,Pará. Rev. Bras. Geociências 30, 597–606.

Previato, M., Monteiro, L.V.S., Bello, R.M. da S., Gonçales, L.C.G., 2020. Evolution of brines and CO2-rich fluids and hydrothermal overprinting in the genesis of the Borrachudo copper deposit, Carajás Province. Ore Geol. Rev. 121, 103561. https://doi.org/10.1016/j.oregeorev.2020.103561

Ptáček, P., 2016. Introduction to Apatites, in: Apatites and Their Synthetic Analogues - Synthesis, Structure, Properties and Applications. pp. 1–60. https://doi.org/10.5772/62208

Putnis, A., 2009. Mineral replacement reactions. Rev. Mineral. Geochemistry 70, 87–124. https://doi.org/10.2138/rmg.2009.70.3

Putnis, A., 2002. Mineral replacement reactions: from macroscopic observations to microscopic mechanisms. Mineral. Mag. 66, 689–708. https://doi.org/10.1180/0026461026650056

Rakovan, J., Newville, M., Sutton, S., 2001. Evidence of heterovalent europium in zoned llallgua apatite using wavelength dispersive XANES. Am. Mineral. 86, 697–700. https://doi.org/10.2138/am-2001-5-610

Rigon, J.C., Munaro, P., Santos, L.A., Nascimento, J.A.S., Barreira, C.F., 2000. Alvo 118 copper-gold deposit: Geology and mineralization, Serra dos Carajás, Pará, Brazil, in: 31th International Geological Congress. Rio de Janeiro, p. [CD-ROM].

Salgado, S.S., de Andrade Caxito, F., Figueiredo e Silva, R.C., Lana, C., 2019. Provenance of the Buritirama Formation reveals the Paleoproterozoic assembly of the Bacajá and Carajás blocks (Amazon Craton) and the chronocorrelation of Mn-deposits in the Transamazonian/Birimian system of northern Brazil/West Africa. J. South Am. Earth Sci. 96, 102364. https://doi.org/10.1016/j.jsames.2019.102364

Santos, R.D. dos, Galarza, M.A., Oliveira, D.C. De, 2013. Geologia, geoquímica e geocronologia do Diopsídio-Norito Pium, Província Carajás. Bol. do Mus. Para. Emílio Goeldi - Série Ciências Nat. 8, 355–382.

Sardinha, A.S., Barros, C.E.M., Krymsky, R., 2006. Geology, geochemistry, and U-Pb geochronology of the Archean (2.74 Ga) Serra do Rabo granite stocks, Carajás Metallogenetic Province, northern Brazil. J. South Am. Earth Sci. 20, 327–339. https://doi.org/10.1016/j.jsames.2005.11.001

Sha, L.K., Chappell, B.W., 1999. Apatite chemical composition, determined by electron microprobe and laser-ablation inductively coupled plasma mass spectrometry, as a probe into granite petrogenesis. Geochim. Cosmochim. Acta 63, 3861–3881. https://doi.org/10.1016/S0016-7037(99)00210-0

Siepierski, L., Ferreira Filho, C.F., 2016. Spinifex-textured komatiites in the south border of the Carajas ridge, Selva Greenstone belt, Carajás Province, Brazil. J. South Am. Earth Sci. 66, 41–55. https://doi.org/10.1016/j.jsames.2015.12.011

Silva, M.G., Teixeira, J.B.G., Pimentel, M.M., Vasconcelos, P.M., Arielo, A., Rocha, W.J.S.F., 2005. Geologia e mineralizações de Fe-Cu-Au do Alvo GT46 (Igarapé Cinzento), Carajás, in: Marini, O.J., Queiroz, E.T., Ramos, B.W. (Eds.), Caracterização de Depósitos Minerais Em Distritos Mineiros Da Amazônia. DNPM/CT-Mineral/ADIMB, Brasília, pp. 94–151.

Skirrow, R.G., 2022. Iron oxide copper-gold (IOCG) deposits – A review (part 1): Settings, mineralogy, ore geochemistry and classification. Ore Geol. Rev. 140, 104569. https://doi.org/10.1016/j.oregeorev.2021.104569

Souza, S.R.B., Macambira, M.J.B., Sheller, T., 1996. Novos dados geocronológicos para os granitos deformados do Rio Itacaiúnas (Serra dos Carajás, PA): implicações estratigráficas, in: V Simpósio de Geologia Da Amazônia. SBG, Belém, pp. 380–383.

Streck, M.J., Dilles, J.H., 1998. Sulfur evolution of oxidized arc magmas as recorded in apatite from a porphyry copper batholith. Geology 26, 523–526. https://doi.org/10.1130/0091-7613(1998)026<0523:SEOOAM>2.3.CO;2

Su, J.H., Zhao, X.F., Li, X.C., Su, Z.K., Liu, R., Qin, Z.J., Chen, M., 2021. Fingerprinting REE mineralization and hydrothermal remobilization history of the carbonatite-alkaline complexes, Central China: Constraints from in situ elemental and isotopic analyses of phosphate minerals. Am. Mineral. 106, 1545–1558. https://doi.org/10.2138/am-2021-7746

Tallarico, F.H.B., 2003. O cinturão cupro-aurífero de Carajás, Brasil. Universidade Estadual de Campinas.

Tallarico, F.H.B., Figueiredo, B.R., Groves, D.I., Kositcin, N., McNaughton, N.J., Fletcher, I.R., Rego, J.L., 2005. Geology and SHRIMP U-Pb geochronology of the Igarapé Bahia deposit, Carajás copper-gold belt, Brazil: An Archean (2.57 Ga) example of Iron-Oxide Cu-Au-(U-REE) mineralization. Econ. Geol. 100, 7–28. https://doi.org/10.2113/100.1.0007

Tallarico, F.H.B., McNaughton, N.J., Groves, D.I., Fletcher, I.R., Figueiredo, B.R., Carvalho, J.B., Rego, J.L., Nunes, A.R., 2004. Geological and SHRIMP II U-Pb constraints on the age and origin of the Breves Cu-Au-(W-Bi-Sn) deposit, Carajás, Brazil. Miner. Depos. 39, 68–86. https://doi.org/10.1007/s00126-003-0383-y

Tassinari, C.C.G., Macambira, M.J.B., 1999. Geochronological provinces of the Amazonian Craton. Episodes 22, 174–182. https://doi.org/10.1080/00206819709465329

Tavares, F.M., Trouw, R.A.J., da Silva, C.M.G., Justo, A.P., Oliveira, J.K.M., 2018. The multistage tectonic evolution of the northeastern Carajás Province, Amazonian Craton, Brazil: Revealing complex structural patterns. J. South Am. Earth Sci. 88, 238–252. https://doi.org/10.1016/j.jsames.2018.08.024

Tazava, E., Oliveira, C.G. de, 2000. The Igarapé Bahia Au-Cu-(REE-U) deposit, Carajás Mineral Province, northern Brazil, in: Porter, T.M. (Ed.), Hydrothermal Iron Oxide Copper-Gold & Related Deposits: A Global Perspective, Volume 1. PGC Publishing, Adelaide, pp. 203–212.

Toledo, P.I. de F., Moreto, C.P.N., Xavier, R.P., Gao, J., Matos, J.H. da S.N. de, Melo, G.H.C., 2019. Multistage Evolution of the Neoarchean (ca. 2.7 Ga) Igarapé Cinzento (GT-46) Iron Oxide Copper-Gold Deposit, Cinzento Shear Zone, Carajás Province, Brazil. Econ. Geol. 114, 1–34. https://doi.org/10.5382/econgeo.2019.4617

Torresi, I., Xavier, R.P., Bortholoto, D.F.A., Monteiro, L.V.S., 2012. Hydrothermal alteration, fluid inclusions and stable isotope systematics of the Alvo 118 iron oxide-copper-gold deposit, Carajás Mineral Province (Brazil): Implications for ore genesis. Miner. Depos. 47, 299–323. https://doi.org/10.1007/s00126-011-0373-4

Trendall, A.F., Basei, M.A.S., De Laeter, J.R., Nelson, D.R., 1998. SHRIMP zircon U-Pb constraints on the age of the Carajás formation, Grão Pará Group, Amazon Craton. J. South Am. Earth Sci. 11, 265–277. https://doi.org/10.1016/S0895-9811(98)00015-7

Tropper, P., Manning, C.E., Harlov, D.E., 2011. Solubility of $CePO_4$ monazite and YPO_4 xenotime in H_2O and H_2O-NaCl at 800°C and 1GPa: Implications for REE and Y transport during high-grade metamorphism. Chem. Geol. 282, 58–66. https://doi.org/10.1016/j.chemgeo.2011.01.009

Vasquez, M.L., Macambira, M.J.B., Armstrong, R.A., 2008a. Zircon geochronology of granitoids from the western Bacajá domain, southeastern Amazonian craton, Brazil: Neoarchean to Orosirian evolution. Precambrian Res. 161, 279–302. https://doi.org/10.1016/j.precamres.2007.09.001

Vasquez, M.L., Rosa-Costa, L.T., Silva, C.M.G., Klein, E.L., Ricci, P.S.F., Barbosa, J.P.O., Lopes, E.C.S., Macambira, E.M.B., Chaves, C.L., Carvalho, J.M.A., Oliveira, J.G.F., Anjos, G.C., Silva, H.R., João, X.S.J., 2008b. Geologia e Recursos Minerais do Estado do Pará: Sistema de Informações Geográficas - SIG: texto explicativo dos mapas Geológico e Tectônico e de Recursos Minerais do Estado do Pará. Escala 1:1.000.000. CPRM, Belém.

Villas, R.N., Santos, M.D., 2001. Gold deposits of the Carajás mineral province: Deposit types and metallogenesis. Miner. Depos. 36, 300–331. https://doi.org/10.1007/s001260100178

Webster, J.D., Piccoli, P.M., 2015. Magmatic apatite: A powerful, yet deceptive, mineral. Elements 11, 177–182. https://doi.org/10.2113/gselements.11.3.177

Williams-Jones, A.E., Migdisov, A.A., Samson, I.M., 2012. Hydrothermal mobilisation of the rare earth elements-a tale of "ceria" and "yttria." Elements 8, 355–360. https://doi.org/10.2113/gselements.8.5.355

Wirth, K.R., Gibbs, A.K., Olszewski Jr., W.J., 1986. U-Pb ages of zircons from the Grão-Pará Group and Serra dos Carajás Granites, Pará, Brazil. Rev. Bras. Geociências 16, 195–200.

Xavier, R.P., Monteiro, L.V.S., Moreto, C.P.N., Pestilho, A.L.S., Melo, G.H.C., Silva, M.A.D., Aires, B., Ribeiro, C., Silva, F.H.F., 2012. The iron oxide copper-gold systems of the Carajás mineral province. Econ. Geol. 16, 433–454.

Xavier, R.P., Monteiro, L.V.S., Rusk, B., Torresi, I., 2011. Comparing Iron Oxide Copper-Gold systems of the Carajás Mineral Province (Brazil) using apatite and magnetite trace elements: implications on genesis and exploration, in: 11th SGA Biennial Meeting. pp. 461–463.

Xavier, R.P., Moreto, C.P.N., Melo, G.H.C., Toledo, P.I. de F., Hunger, R.B., Delinardo da Silva, M.A., Faustinoni, J.M., Lopes, A.M., Monteiro, L.V.S., Previato, M., Jesus, S. dos S.G.P., Huhn, S.R.B., 2017. Geology and Metallogeny of Neoarchean and Paleoproterozoic Copper Systems of the Carajás Domain, Amazonian Craton, Brazil, in: 14th SGA Biennial Meeting. SGA, Quebéc, pp. 899–902.

Xu, C., Kynicky, J., Chakhmouradian, A.R., Campbell, I.H., Allen, C.M., 2010. Trace-element modeling of the magmatic evolution of rare-earth-rich carbonatite from the Miaoya deposit, Central China. Lithos 118, 145–155. https://doi.org/10.1016/j.lithos.2010.04.003

Zeng, L.P., Zhao, X.F., Li, X.C., Hu, H., McFarlane, C., 2016. In situ elemental and isotopic analysis of fluorapatite from the Taocun magnetite-Apatite deposit, Eastern China: Constraints on fluid metasomatism. Am. Mineral. 101, 2468–2483. https://doi.org/10.2138/am-2016-5743

Zhang, D., Liu, Y., Pan, J., Dai, T., Bayless, R.C., 2019. Mineralogical and geochemical characteristics of the Miaoya REE prospect, Qinling orogenic Belt, China: Insights from Sr-Nd-C-O isotopes and LA-ICP-MS mineral chemistry. Ore Geol. Rev. 110, 102932. https://doi.org/10.1016/j.oregeorev.2019.05.018

Zirner, A.L.K., Marks, M.A.W., Wenzel, T., Jacob, D.E., Markl, G., 2015. Rare earth elements in apatite as a monitor of magmatic and metasomatic processes: The Ilímaussaq complex, South Greenland. Lithos. https://doi.org/10.1016/j.lithos.2015.04.013

ANEXO B: Superimposition of hydrothermal events in the granite-related Santa Lúcia Cu-Au deposit, Carajás Domain (Brazil): Insights from trace element geochemistry and U-Pb geochronology in apatite

Raphael B. Hunger [a,*], Carolina P. N. Moreto [a], Roberto P. Xavier [a], Gláucia N. Queiroga [b], Cristiano de C. Lana [b], Wang Liao [c], Xin-Fu Zhao [c], Gustavo H. C. de Melo [b]

[a] Institute of Geosciences, University of Campinas, 250 Carlos Gomes, Campinas, São Paulo 13083-855, Brazil

[b] Department of Geology - Morro do Cruzeiro Campus, Federal University of Ouro Preto, Nove Street, Ouro Preto 35400-000, Brazil

[c] State Key Laboratory of Geological Processes and Mineral Resources, and Faculty of Earth Resources, China University of Geosciences, 388 Lumo Road, Wuhan 430074, China

* Corresponding author: raphael.hunger@gmail.com; ORCID ID: 0000-0003-3712-8406

Abstract

The Santa Lúcia Cu-Au-(W-Bi-Sn) deposit, within the Southern Copper Belt of the Carajás Province (Brazil), represents a Neoarchean (ca. 2.68 Ga) member of the granite-related class of deposits that are currently recognized in this ore district. The hydrothermal system evolution at Santa Lúcia is remarkably complex and counted with multiple events of metasomatic activity that have been registered through compositional and textural variations in apatite grains associated with the ore zones of deposit. Based on cathodoluminescence microscopic investigations we have identified three distinct hydrothermal apatite generations (SL-1, SL-2, and SL-3) in these ore zones. The primary SL-1 apatite represents cores for the SL-2 and SL-3 apatites and is relatively richer in Cl, with overall higher trace and rare earth elements (REE) contents, according to high-precision EPMA and LA-ICP-MS analyses. Coupled dissolution-reprecipitation processes caused by the interaction of the SL-1 apatite with highly reactant, acidic, and moderately oxidizing F-rich fluids, led to the later precipitation of the SL-2 and SL-3 apatites. Remobilization of light-REE in this process triggered the crystallization of monazite inclusions mostly within the SL-3 apatite. The U-Pb results obtained in this study suggest that ore-related apatite at Santa Lúcia recorded a superimposition of metasomatic events that involved at least three distinct hydrothermal pulses, spanning from the Neoarchean (ca. 2.56 Ga) to the Paleoproterozoic (ca. 2.1 and 1.81 Ga).

Keywords: Santa Lúcia deposit, Southern Copper Belt, Carajás Province, Apatite, Hydrothermal alteration

1. Introduction

The Southern Copper Belt (SCB), within the Carajás Province (Brazil), constitutes a remarkably fertile ore district that hosts an extraordinary number of copper deposits, comprising, among others, small tonnage (<50 Mt) granite-related Cu-Au-(W-Bi-Sn) ore systems (Pollard et al., 2019; Xavier et al., 2017, 2012). Striking features shown by deposits of this class include their iron oxide-poor nature, extensive quartz-muscovite-rich alteration assemblages (e.g., greisenization), relatively reduced ore paragenesis, and marked geochemical affinity for granitophile elements (e.g., W, Bi, Sn, Li) (Grainger et al., 2008; Hunger et al., 2021; Pollard et al., 2019; Tallarico et al., 2004). Furthermore, the vast majority of the currently known granite-related deposits at Carajás have been formed during the Paleoproterozoic (ca. 1.88 Ga; Grainger et al., 2008; Tallarico et al., 2004; Volp, 2005), coevally with the extensive A-type magmatic event that originated several granite stocks in the province.

The Santa Lúcia deposit lies in the southeastern margin of the SCB and constitutes the only Neoarchean (ca. 2.68 Ga; Hunger et al., 2021) member of this deposit class known so far. However, the paragenetic evolution of the deposit is still poorly constrained in time and a more complex evolutionary history not necessarily restrict to the Neoarchean cannot be completed discarded. Thus, the combined trace element geochemistry and U-Pb systematics of apatite, which, in turn, represents a remarkably abundant gangue mineral within the ore zones of the deposit, could provide important information about the fluid and geochronological evolution at Santa Lúcia. In fact, apatite trace element compositions and microtextural characterization have been widely applied to trace metasomatic processes in ore systems (Mao et al., 2016; Mercer et al., 2020). Furthermore, apatite can be an effective U-Pb geochronometer, considering its closure temperature of up to 600ºC (Cochrane et al., 2014; Kirkland et al., 2018). As such, we investigate compositional and textural variations in ore-related apatite grains from the Santa Lúcia deposit, combining it with *in-situ* laser ablation-inductively coupled plasma-mass spectroscopy (LA-ICP-MS) U-Pb analyses, with the aim of better constraining the history of hydrothermal overprinting in the deposit, with possible implications for the metallogenesis of the SCB.

2. Geological background

2.1. Regional geology of the Carajás Domain

The Carajás Domain (CD), within the Carajás Province (Amazonian Craton; **Fig. 1a–b),** is bounded to the north by the Buritirama shear zone (Costa et al., 2016), which separates it from the Paleoproterozoic (2.3–2.05 Ga; Vasquez et al., 2008) Bacajá Domain (BD). Conversely, a geophysically inferred, E-W lineament isolates the CD from the Rio Maria Domain (RMD) to the south (Feio et al., 2013; Motta et al., 2019). Mesoarchean rocks (ca. 3.0 to 2.85 Ga; Silva et al., 2021 and references therein) comprising migmatitic orthogneisses, orthogranulite and a broad set of granitoids constitute the basement substrate to the CD. Overlying these basement rocks are metavolcano-sedimentary sequences that compose the Neoarchean to Paleoproterozoic (ca. 2.76–2.0 Ga) Carajás Basin, whose recently reinterpreted stratigraphy includes, from bottom to top, mafic volcanic/volcanoclastic rocks and banded iron formation of the Grão Pará Group, as well as clastic sedimentary strata associated with the Serra Sul, Azul, Águas Claras and Gorotire formations (Araújo Filho et al., 2020; DOCEGEO, 1988; Tavares et al., 2018). The Carajás Basin was possibly originated in an intracratonic rift (DOCEGEO, 1988; Tavares et al., 2018) or arc-related setting (Dardenne et al., 1988; Figueiredo e Silva et al., 2020).

Neoarchean (ca. 2.76–2.73 Ga and ca. 2.57 Ga) granite stocks (Feio et al., 2013; Machado et al., 1991) and mafic-ultramafic intrusive bodies (Mansur and Ferreira Filho, 2016) are broadly recognized within the CD. Paleoproterozoic (ca. 1.88 Ga) felsic magmatism is mostly characterized by the A-type granites of the Serra dos Carajás Intrusive Suite (Machado et al., 1991; Tallarico et al., 2004). The structural configuration of the CD involved a progressive WNW-ESE compression that produced major regional-scale discontinuities, including mostly the Carajás, Cinzento, and Canaã shear zones (Pinheiro et al., 2013).

2.2. Geology of the Santa Lúcia granite-related deposit

The Santa Lúcia deposit (5–14 Mt at 1.4–2.0% Cu, 0.2–0.4 g/t Au; OZ Minerals, 2019) is situated in the Southern Copper Belt (SCB; **Fig. 1c**) of the CD, near the Serra do Rabo region, and is hosted by a subvolcanic rhyolitic rock correlated with the Grão Pará Group (**Fig. 1d**). An unmineralized pegmatite intrusive body crosscut the subvolcanic host rock and displays macro- (e.g., boudinaged megacrysts) to microscopic (e.g., crystal stretching and bending) features that suggest an emplacement during a transition from ductile to brittle deformation regimes. The Santa Lúcia hydrothermal system is marked by an early event of chlorite alteration, which is ensued by spatially restrict potassic alteration with K-feldspar and greisenization. Both potassic and greisen alteration stages are interpreted to be spatially and genetically associated with the emplacement of the pegmatite in the deposit area.

Copper-gold ore is spatially associated with greisenized domains and chiefly represented by matrix-supported, chalcopyrite-rich breccias with sphalerite and pyrrhotite. Fluorapatite (**Fig. 7a**) and quartz are the main gangue minerals found within the ore zones of the deposit, occurring in paragenesis with the sulfide minerals. Post-ore sericite and hematite veining and fracture infill overprint previous zones of hydrothermal alteration and the ore zones. A weighted average $^{207}Pb/^{206}Pb$ age of 2688 ± 27 Ma (MSWD = 0.14) was obtained through in-situ analyses of hydrothermal monazite grains from the main brecciated ore zone of the Santa Lúcia deposit (Hunger et al., 2021).

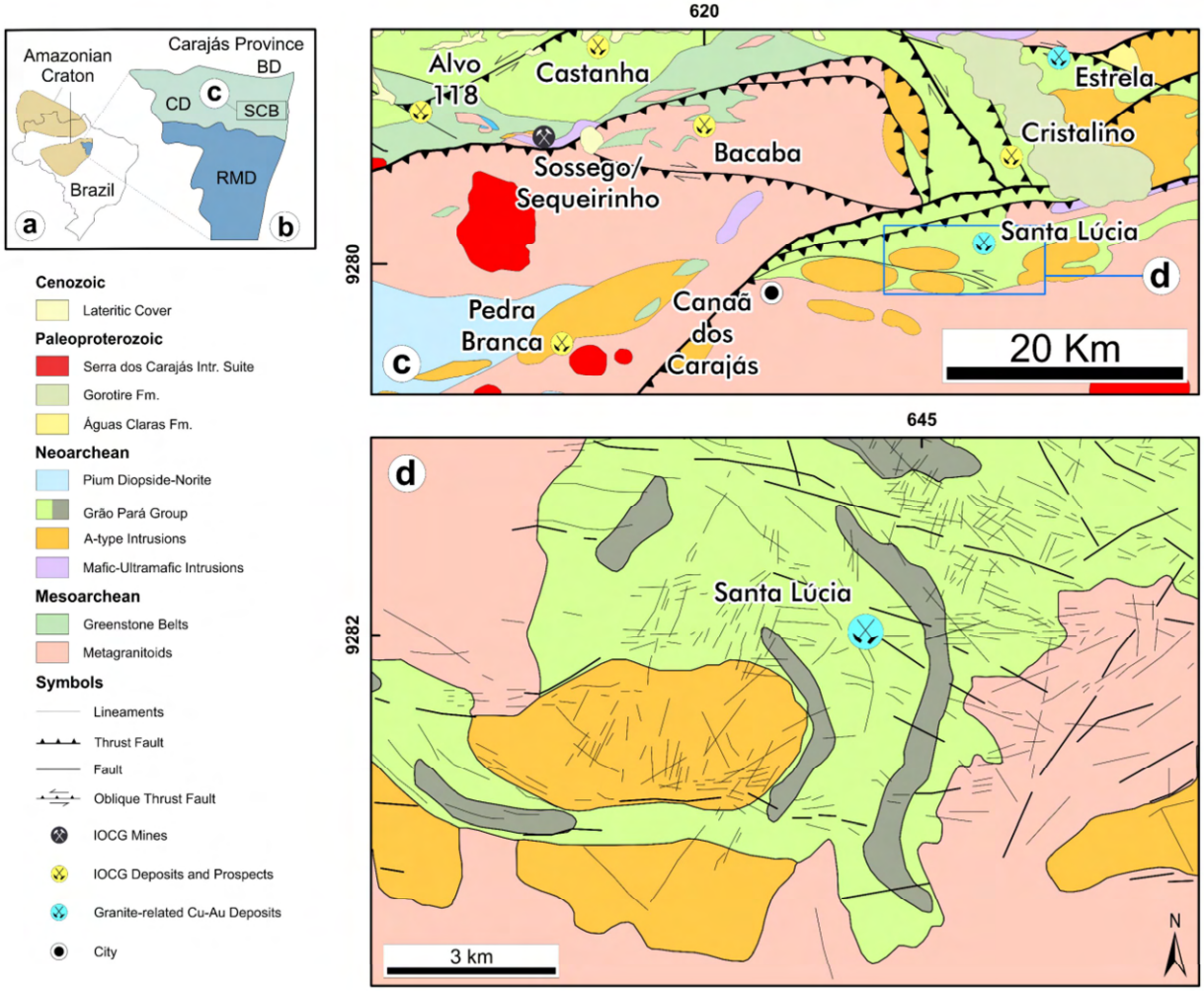

Fig. 1. (a) The Carajás Province (blue) within the Brazilian Amazonian Craton (beige). (b) Subdivision of the Carajás Province into the Carajás (north) and Rio Maria (south) domains. Note the BD limiting to the north the CD. (c) Simplified geological map of the SCB, displaying the location of the main copper-gold deposits and mines found in the area (modified from Costa et al., 2016). (d) Local geological map of the granite-related Santa Lúcia deposit region (modified from Lima, 2002). Abbreviations: BD = Bacajá Domain, CD

= Carajás Domain, IOCG = iron oxide copper-gold, RMD = Rio Maria Domain, SCB = Southern Copper Belt.

3. Analytical methods

3.1. Sampling and petrographic characterization

Prior to chemical analyses, representative apatite crystals from the Santa Lúcia (sample SL-22/76.1) deposit ore zone were investigated by conventional petrography and backscattered electron (BSE)-imaged utilizing a LEO 430i scanning electron microscope (SEM), at Institute of Geosciences of the University of Campinas (UNICAMP), Brazil. An Oxford energy dispersive spectroscopy (EDS) system was employed for the identification of inclusions within apatite grains. Optical microscopic cathodoluminescence (OM-CL) images were acquired at the State Key Laboratory of Geological Processes and Mineral Resources (GPMR - China University of Geosciences), by a CITL8200 MK-5 CL system attached to a LEICA DM 2700P microscope. The CL equipment was configured to capture images by using an exposure time of 6 s, a 10 kV accelerating voltage and a 250 μA beam current.

3.2. Electron probe microanalysis (EPMA)

EPMA analyses were carried out at the Federal University of Ouro Preto (UFOP) on a JEOL JXA-8230 instrument operated using the wavelength-dispersion mode, with a 40 nA probe current, an accelerating potential of 20 kV, and a beam diameter of 5 nm. Apatite stoichiometry was calculated following the "Approach 2" of Ketcham (2015), on the basis of 25 oxygen atoms and assuming an ideal behavior of the monovalent anion site. Reported fluorine contents are most likely overestimated due to an increase in F X-ray counts during the analytical sections, whereas chlorine concentrations are possibly underestimated in response to a decrease in Cl X-ray counts. Thus, as a consequence of these imprecisions, the calculated OH contents (i.e., OH = 2 – F – Cl) were considered below detection limit when negative values were yielded.

3.3. Trace element and U-Pb LA-ICP-MS analyses

Trace element and U-Pb analyses in apatite were performed at the Applied Isotope Research Lab (UFOP) utilizing a ThermoFisher Element II sector field (SF)-LA-ICP-MS, respectively attached to 213 Nd:YAG (CETAC UP-213 nm) and CETAC LSX-213 G2+ laser ablation systems. For the trace element analyses, operating conditions included a 6 Hz repetition rate, a fluence of 6 J/cm^{2,} and a spot size of 40 μm, employing 20 s of background acquisition, ensued by 60 s of sample ablation. For calibration purposes, a CaO concentration

of 54.0 wt% was adopted as an internal standard, according to previously conducted EPMA analyses. To assure quality control, the NIST612, BHVO, and BCR glasses were used as calibration materials (reference values are from Jochum et al., 2016). Data reduction and concentration calculations were performed using the Glitter software (Griffin et al., 2008), after offline processing of raw counts.

In situ U-Pb data were acquired with the instrument operating in time-resolved, peak-jumping and pulse-counting mode, considering 25 s of background measurement, followed by 30 s of sample ablation. Analyses were undertaken employing a nominal energy output of 30%, repetition rate of 10 Hz, laser fluence of ~3.5 J/cm^2, and a spot size of 40 μm. Due to the microtextural complexity of the analysed apatite grains, analytical spots were not always precisely placed within the distinct domains revealed by CL imaging. The Glitter software (Van Achterberg et al., 2001) and an in-house program (Saturn; Silva, 2020) were used for offline data reduction, whilst age calculations were obtained through IsoplotR (Vermeesch, 2018). Calculated sample ages correspond to the lower intercept in a Tera-Wasserburg diagram and were determined through unanchored regression lines. Multiple analyses of reference materials, including the in-house Tanzania zircon (Tanz 1) and the Madagascar (MAD1 and MAD2; ID-TIMS ages of 486.58 ± 0.85 Ma and 474.25 ± 0.41 Ma, respectively; Thomson et al., 2012), 401 (LA-ICP-MS age of 506.2 ± 8.1 Ma; Thompson et al., 2016), and Sumé (ID-TIMS age of 568 ± 1.0 Ma; Lana et al., 2022) apatites, were conducted for quality control purposes. Concordia ages of 603.5 ± 2.3 Ma (MSWD = 1.5) and 599.6 ± 2.0 Ma (MSWD = 1.3) were calculated for the Tanz 1 zircon and are in agreement, within uncertainty, with the reference ID-TIMS age of 601 ± 1.0 Ma (Lana et al., 2022). Yielded intercept ages for the MAD1 (481.66 ± 7.84 Ma), MAD2 (469.07 ± 4.51 Ma), 401 (507.51 ± 1.53 Ma), and Sumé (571.67 ± 1.68 Ma) apatites are consistent, within errors, with those determined by Thomson et al. (2012), Thompson et al. (2016), and Lana et al. (2022), respectively.

4. Results

4.1. Textural aspects of apatite

Apatite grains in the breccia ore zone of the Santa Lúcia deposit, are medium- to coarse-grained (<0.3 mm in size), BSE-monotone, and mostly euhedral with prismatic habit. They occur dispersed in a sulfide-dominant matrix that mainly encompasses chalcopyrite, pyrrhotite, and sphalerite (**Fig. 2a**). In general, grains display clear oscillatory zoning marked by brownish CL domains (SL–1) that are involved by bright yellowish-green regions (SL–2;

Fig. 2b). Greenish CL zones (SL–3) are essentially characterized along grain rims or extending outward from fractures (**Fig. 2c**), these generally filled with chalcopyrite, sphalerite, sericite, or monazite. A significant number of inclusions, which may comprise chalcopyrite, monazite, quartz, sphalerite, pyrrhotite, and allanite, are recognized within apatite at Santa Lúcia. Notably, monazite inclusions can be substantially big (>300 µm in size), especially when near grain rims (**Fig. 2d**). In this case, they commonly form small aggregates that are generally enveloped by greenish CL halos (**Fig. 2e**). Furthermore, several apatite grains are rimmed by monazite overgrowths (**Fig. 2f**) which are seemingly connected to sericite-hematite-chlorite alteration fronts (**Fig. 2g**).

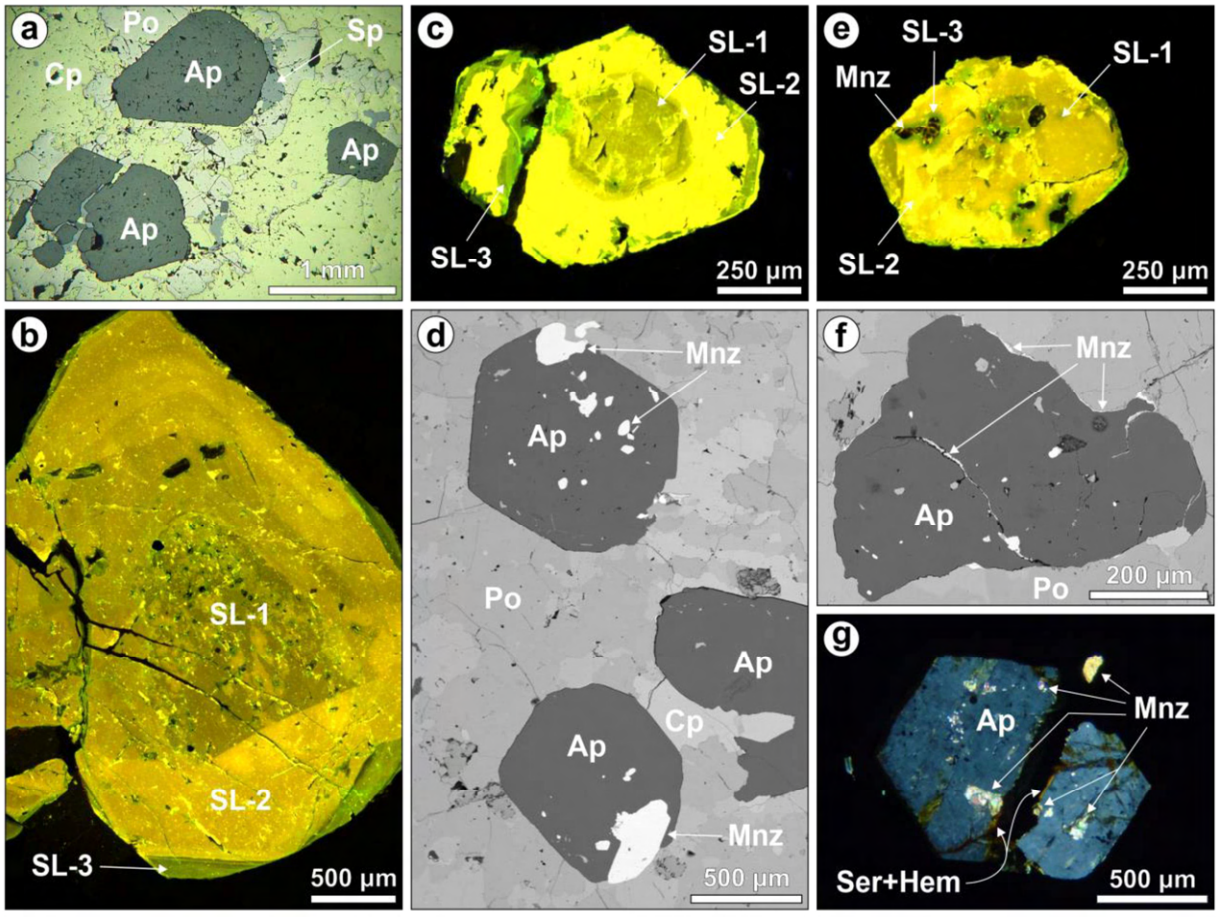

Fig. 2. Photomicrographs of apatite grains from the Santa Lúcia deposit, displaying their main characteristics. (a) Prismatic apatite grains associated with chalcopyrite, pyrrhotite and sphalerite in the main breccia ore zone (reflected light/plane-polarized light [PPL]). (b) Apatite grain showing notably oscillatory zoning with brownish CL domains/core (SL–1) involved by yellowish-green CL regions (SL–2) and greenish CL rims (SL–3). (c) Prismatic apatite crystal with oscillatory zoning. Note that greenish luminescent regions (SL–3) also extend outward from the internal fracture. (d) BSE image of apatite grains in association with chalcopyrite-pyrrhotite-rich zones and rimmed by coarse-grained monazite overgrowths. (e)

Hexagonally-shaped apatite crystal evidencing complex luminescence texture and monazite aggregates that are involved by greenish CL halos (SL–3). (f) BSE image of apatite associated with pyrrhotite and rimmed by monazite overgrowths. Note that monazite also occurs as fracture infills within apatite. (g) Intensively fractured apatite crystal with monazite overgrowths in apparent association with sericite-hematite alteration fronts (transmitted light/cross-polarized light [TL/XPL]). Abbreviations: Ap = apatite, Cp = chalcopyrite, Hem = hematite, Mnz = monazite, Po = pyrrhotite, Ser = sericite, Sph = sphalerite.

4.2. Apatite major and trace element compositions

Representative major and trace element compositional data of apatite from the ore breccia zone of the Santa Lúcia deposit are shown in **Appendix 1** and **2**. In a ternary F-Cl-OH diagram, the analysed apatite types plot fundamentally within the fluorapatite field (**Fig. 3a**), although the SL-3 apatite exhibits relatively lower Cl contents (0.003–0.15 wt%) when compared to the SL-1 and SL-2 apatites combined (0.09–0.31 wt%; **Fig. 3b**). Conversely, F (5.07 wt% on average), CaO (49.72–56.44 wt%), and P_2O_5 (39.62–43.60 wt%) values for the SL-3 apatite are slightly higher than those showed by the SL-1 and SL-2 apatites combined (4.88 wt% on average, 46.71–55.73 wt%, 36.66–43.18 wt%, respectively). Estimated OH contents span from 0.05 to 0.47 wt% for the combined SL-1 and SL-2 apatites, whereas values for the SL-3 are essentially below detection limit (BDL). All apatite types display significantly low concentrations of Na_2O (≤0.10 wt%, but normally BDL), SrO (≤0.08 wt%), BaO (≤0.05 wt%), and TiO_2 (≤0.02 wt%). Low to moderate concentrations of SO_3 (0.001–5.85 wt%) and FeO (0.004–5.22 wt%) are observed for the SL-3 apatite, whereas values shown by the SL-1 and SL-2 apatites combined are usually low for both compounds (≤0.4 wt%).

In a general way, the SL-3 apatite tends to be significantly depleted in trace element contents when compared to the SL-1 and SL-2 apatites (**Fig. 3c**). Average magnesium concentrations are higher than 100 ppm for the SL-1 (108.99 ppm) and SL-2 (125.07) apatites, but most commonly below 80 ppm for the SL-3 apatite. Significant amounts of Mn (>2000 ppm) are found in the SL-1 and SL-2 apatites, although values are slightly higher for the latter (550.94–2472.70 ppm). Gallium and barium contents are considerably low (<10 ppm) in all apatite varieties. Conversely, average yttrium concentrations are consistently above 100 ppm for all the analysed apatite types, with the highest values attained by the SL-1 apatite (905.25–2141.21 ppm). Strontium contents reach up to a few hundreds of ppm in all apatite types, with the lowest values exhibited by the SL-3 apatite (88.20–210.01

ppm). Both Th and U contents are progressively lower from the SL-1 apatite (0.01–0.24 and 0.27–5.65, respectively) to the SL-2 (0.002–0.09 and 0.12–2.09, respectively) and SL-3 (0.002–0.04 and 0.001–0.15, respectively) apatites (**Fig. 3c**).

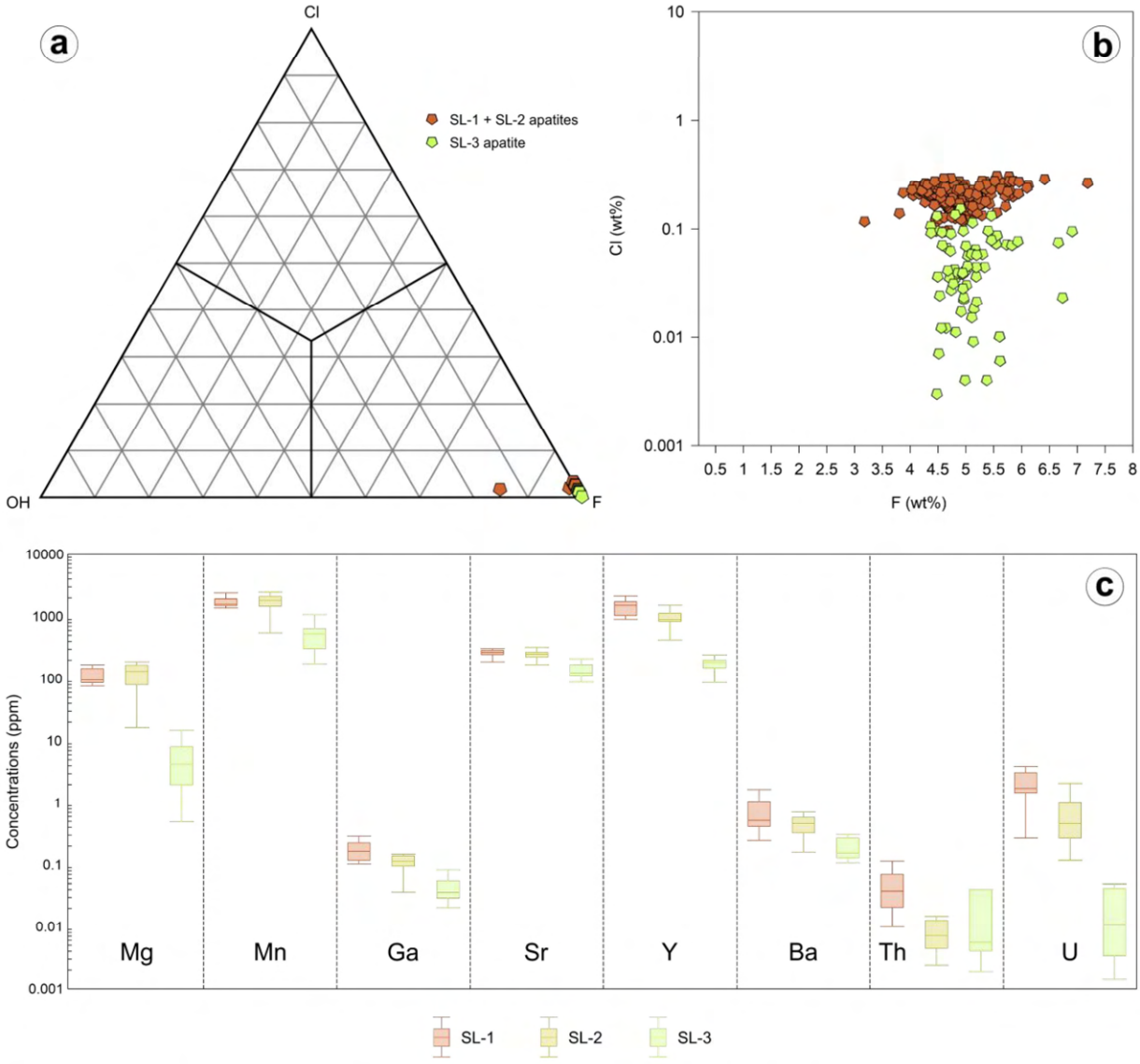

Fig. 3. (a) Ternary F-Cl-OH diagram (Webster and Piccoli, 2015) and (b) F vs. Cl (wt%) biplot based on halogen atomic proportions for the analysed apatite. (c) Representative box plots of selected trace elements for apatite at Santa Lúcia. Boxes represent the interquartile range (IQR).

The SL-1 apatite exhibits the highest LREE contents (1005.80–3047.46 ppm), as well as higher average $(La/Yb)_N$ and $(La/Sm)_N$ ratios (1.84 and 0.88, respectively) among the analysed apatite varieties (**Fig. 4a–c**), but analogous and relatively flat chondrite-normalized REE patterns when compared to the SL-2 apatite (La_N/Yb_N = 1.17–2.37). Both apatite types are, however, marked by a noticeable HREE depletion (ΣHREE = 659.00 and 418.19 ppm on

average, respectively). Conversely, the SL-3 apatite is considerably LREE-depleted (ΣLREE = 60.68–714.73 ppm) and display a clear middle-REE (MREE) enrichment (La_N/Yb_N = 1.00–2.42). All apatite varieties demonstrate strong negative Eu anomalies (Eu/Eu* = 0.31–0.39 on average). In a $(Ce/Ce^*)_N$ vs. $(Eu/Eu^*)_N$ plot, the SL-1 and Sl-2 apatites plot essentially within the "moderately reduced" field of Cao et al. (2012), whereas data for SL-3 apatite can fall within the "moderately oxidized" field (**Fig. 4d**).

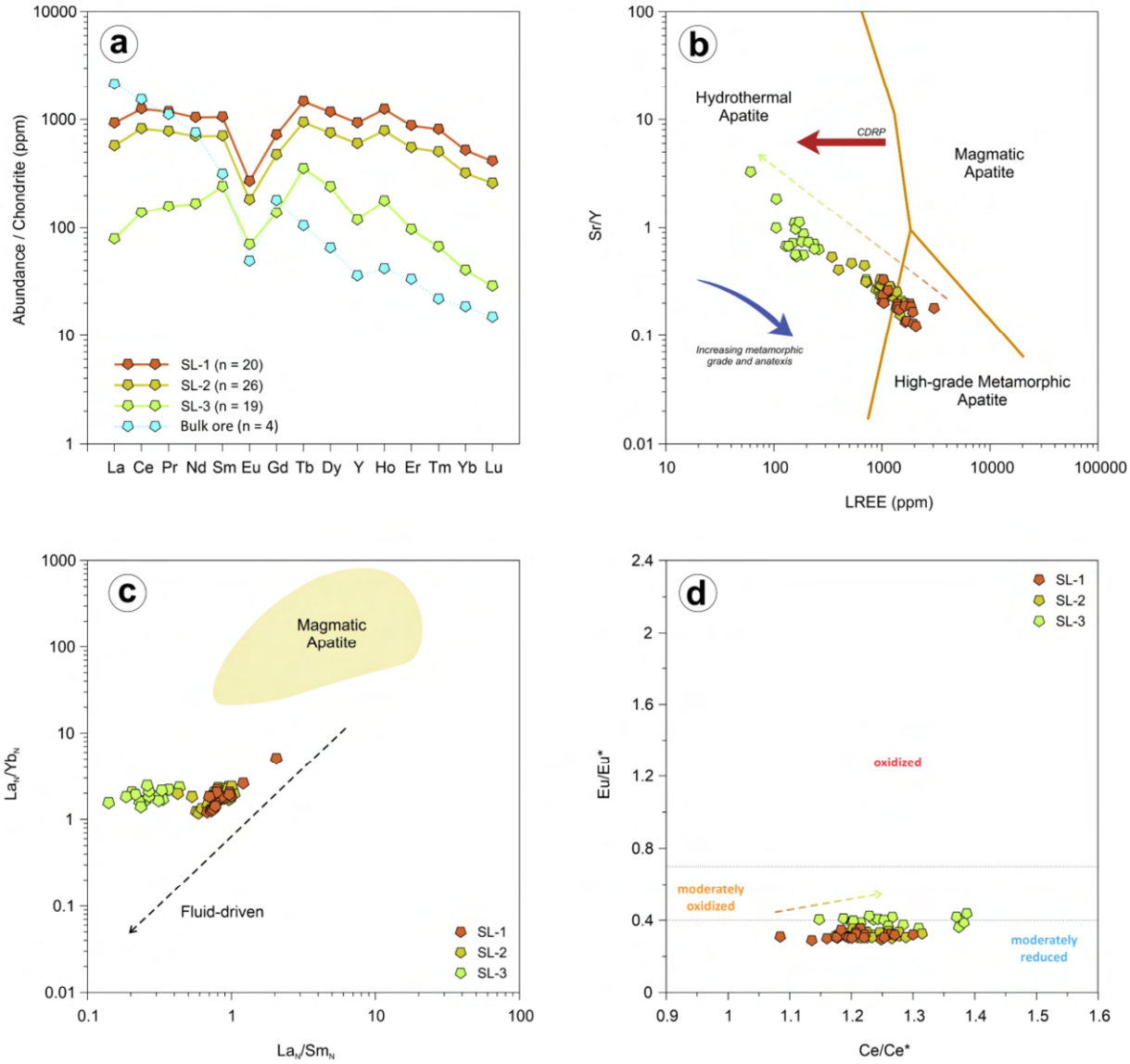

Fig. 4. (a) Chondrite-normalized REE distribution patterns for ore-related apatite at Santa Lúcia. Normalization values follow those of McDonough and Sun (1995). (b) LREE vs. Sr/Y, (c) La_N/Sm_N vs. La_N/Yb_N and (d) $(Ce/Ce^*)_N$ vs. $(Eu/Eu^*)_N$ divalent plots. Fields in (b) are modified from Li et al. (2022), after O'Sullivan et al. (2020). The yellowish shaded area in (c) represents a compilation of magmatic apatite data found in Li et al. (2022) and references therein. Discriminative fields in (d) are from Cao et al. (2012).

4.3. Apatite U-Pb ages

Geochronological U-Pb data based on thirty-six analytical spots distributed on fourteen apatite grains from the main breccia ore zone of the Santa Lúcia deposit (**Appendix 3)** have revealed three distinct age groups on a Tera–Wasserburg diagram, according to unanchored regression lines (**Fig. 5**): i) 2563.3 ± 87.4 Ma (2σ; MSWD = 0.45); ii) 2088.3 ± 17.9 Ma (2σ; MSWD = 1.3); iii) 1813.5 ± 17.5 Ma (2σ; MSWD = 1.3). Initial $^{207}Pb/^{206}Pb$ ratios for each age group are 1.40 ± 0.33, 1.30 ± 0.10, and 1.264 ± 0.031, respectively.

5. Discussions

5.1. Constraints on the fluid evolution at Santa Lúcia

Detailed CL microscopic investigations conducted in this study allowed the discrimination of three different types of apatite within the ore zone of the Santa Lúcia deposit, with distinct major and trace element compositions. Overall, the SL-1 apatite demonstrates the highest trace and REE contents among the analysed apatite types and generally represents cores for the SL-2 and SL-3 varieties. Collectively, these textural and compositional evidence strongly indicates that the SL-1 apatite could, therefore, be primary in origin.

According to the data spreading on a LREE versus Sr/Y diagram, the SL-1 apatite plots close to the join between the "high-grade metamorphic" and "hydrothermal" fields of Li et al. (2022), suggesting that it could have been precipitated in either one of these environments. However, there are no evidence of high-grade metamorphism affecting the host rocks and ore zones of the Santa Lúcia deposit (Hunger et al., 2021), thus making it unlikely to assume that apatite had formed under such conditions. Hence, the crystallization of the SL-1 apatite was probably associated with metasomatic, fluid-driven processes, as also pointed out by its low (<10) $(La/Yb)_N$ and $(La/Sm)_N$ ratios (**Fig. 4c**), which are characteristic of hydrothermally formed apatite (Broom-Fendley et al., 2016; Lu et al., 2021; Mercer et al., 2020). Considering that the SL-1 apatite has the highest chlorine contents among all apatite varieties investigated in this study (**Fig. 3b**), as well as relatively low $(Eu/Eu^*)_N$ values (<0.4; **Fig. 4d**), the fluid responsible for its precipitation was presumably Cl-rich and moderately reduced. Therefore, it is reasonable to expect that the interaction of the SL-1 apatite with F-enriched fluids during superimposing hydrothermal events could have led to the precipitation of the SL-2 and SL-3 apatites. Indeed, under hydrothermal conditions, apatite is considerably prone to post-crystallization modifications that are normally induced by its interplay with reactant fluids (Harlov, 2015). Such fluid-induced modifications are commonly attributed to

coupled dissolution-reprecipitation (CDRP) processes, which are capable of mobilizing chemical components away from pristine apatite domains, leaving reprecipitated apatite regions relatively depleted in certain trace elements, especially REE (Harlov, 2015; Harlov et al., 2005), which is the case of the SL-2 and SL-3 apatites. In this scenario, leached LREE could have been readily reincorporated by subsequently formed monazite inclusions that occur preferentially enclosed by or as overgrowths in the SL-3 apatite (**Fig. 2e–f**).

The fluorapatite at Santa Lúcia has also registered a transition from slightly HREE-depleted signatures for the SL-1 and SL-2 types, to markedly convex and MREE-enriched distribution patterns for the SL-3 apatite (**Fig. 4a**). Such distinct shift in REE + Y chondrite-normalized patterns is similar to what is observed in fluorapatite from the hematite-sericite zone at the Olympic Dam deposit (Krneta et al., 2017) and in samples from the Pea Ridge IOA and Boss IOCG deposits (Mercer et al., 2020), which have been attributed to a combined increase in hydrothermal fluid salinity and a decrease in pH conditions. This is accordance with the hydrothermal evolution of the Santa Lúcia deposit that indicates the continuous participation of acidic fluids in late stages of metasomatic activity (i.e., greisenization followed by ore precipitation and sericite veinlet formation; Hunger et al., 2021). Furthermore, fracture-controlled hematite veinlets represent the latest metasomatic event recognized at Santa Lúcia, indicating that the hydrothermal system also became progressively more oxidizing in the deposit. Indeed, the comparatively higher $(Eu/Eu^*)_N$ values shown by the SL-3 apatite relative to the SL-1 and SL-2 apatites, suggest a precipitation under moderately oxidizing conditions, which could be explained by its apparent spatial connection with sericite-hematite alteration fronts.

5.2. U-Pb apatite ages and their implications for the metallogenesis of the SCB

Apatite is particularly useful for both thermo- and geochronological studies, especially considering that it can be dated by more than a single technique (e.g., U-Pb, U-Th-Sm/He, fission track) and, therefore, provide a better understanding of high (~550ºC) to near-surface temperature processes that had affected different types of rock materials (Glorie et al., 2020; Xiang et al., 2021). However, the fact that apatite usually has low U contents and, in turn, can contain substantial amounts of common (non-radiogenic) Pb, makes U-Pb geochronology considerably challenging (Kirkland et al., 2018). Furthermore, under hydrothermal conditions the U-Pb system in apatite can be greatly affected by metasomatic processes. In a broad sense, metasomatism can either trigger new apatite growth, which makes the U-Pb geochronometer register from the point that Pb ceases to diffuse out of the

grain, or lead to partial or complete loss of radiogenic Pb, thus recording a mixed age or even the timing of metasomatism, if Pb loss is complete (Kirkland et al., 2018). Therefore, interpretations of ages obtained through apatite U-Pb geochronology must be done with caution.

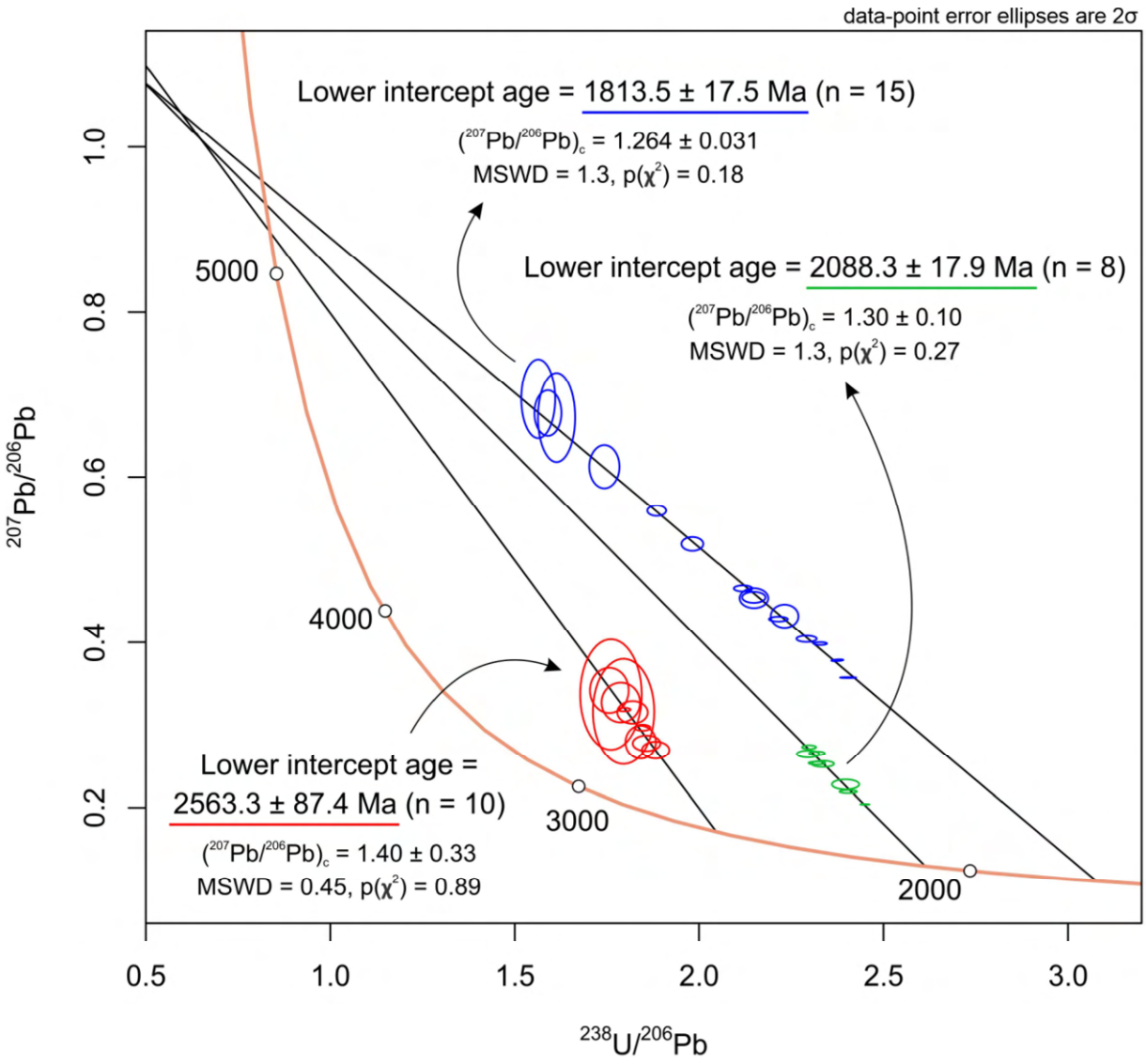

Fig. 5. Tera-Wasserburg concordia plots for apatite of the Santa Lúcia ore breccia. Reported uncertainties for each age group are 95% confidence level. Abbreviations: MSWD = mean square weighted deviation, $p(\chi^2)$ = chi-square probability.

At Santa Lúcia, pristine SL-1 apatite domains have been clearly affected by metasomatism, which, in turn, caused the later precipitation of the SL-2 and SL-3 apatites, as indicated by microtextural observations and chemical data. According to the U-Pb ages obtained in this study, at least three distinct events at ca. 2.56 Ga, 2.1 Ga, and 1.81 Ga (**Fig. 5**) have been recorded by apatite within the breccia ore zone of the deposit. The currently

available geochronological data for the Santa Lúcia deposit also include a weighted average $^{207}Pb/^{206}Pb$ age of 2688 ± 27 Ma (MSWD = 0.14), obtained through dating of hydrothermal monazite grains, which is currently interpreted as the timing of ore formation in the deposit (Hunger et al., 2021). In this sense, and considering that thermally activated diffusion of apatite could have been caused by temperature decrease during the mineralization event (Kirkland et al., 2018), the Neoarchean ca. 2.56 Ga age may represent the timing of cooling to the closure temperature for Pb diffusion, and not necessarily the moment of the SL-1 apatite precipitation. The younger ca. 2.1 Ga and 1.81 ages could, therefore, be associated with new metasomatic apatite growth (SL-2 and SL-3 ?) caused by superimposing Paleoproterozoic hydrothermal events.

From a metallogenic perspective, the significance of the ca. 2.56 Ga hydrothermal event in the SCB is still poorly understood, although magmatic-hydrothermal events with similar ages that were recognized in the northern CD have been widely debated in the last few years (Hunger et al., 2018; Melo et al., 2016; Toledo et al., 2019). So far, the only published data that suggests hydrothermal activity at this time in the SCB have been acquired through dating of hydrothermal zircon crystals from the Planalto Granite (2546 ± 56, MSWD = 7.5; Borba et al., 2021). In this case, it has been associated with the reactivation of the Carajás strike-slip fault system and the consequent channeling of hydrothermal fluids that could have possibly played a role in the evolution of the Santa Lúcia deposit.

Similarly to what is observed at Santa Lúcia, a hydrothermal episode at ca. 2.1 Ga in the SCB has been recorded by titanite (2011 ± 6.8 Ma, MSWD = 3.9; Previato et al., 2020) and monazite (2060 ± 9.6 Ma, MSWD = 1.3; Moreto et al., 2015) crystals, respectively associated with albite–titanite–apatite–chalcopyrite veins from the Borrachudo IOCG deposit and the ore zone of the Bacaba IOCG deposit. Additionally, coeval Ar-Ar ages were also obtained for hornblende (2047 ± 16 Ma), biotite (2046 ± 15 Ma), and tremolite (2009 ± 19 Ma) from Meso- to Neoarchean rocks of the SCB (Tavares et al., 2018), as well as vein-associated biotite (2193 ± 4 Ma) from the Corta Goela Cu-Au prospect (Pollard et al., 2019). Collectively, these ages have been currently interpreted to be result of an Orosirian reactivation of regional-scale structures (e.g., Carajás Fault and Canaã Shear Zone) during the collision of the CD and BD (Moreto et al., 2015a; Pollard et al., 2019; Tavares et al., 2018).

Finally, the ca. 1.81 age registered by apatite at Santa Lúcia has not yet been specifically recorded in the SCB, but overlaps within errors with the Sm-Nd isochron age of 1839 ± 15 Ma demonstrated by quartz-grunerite veins of the Gameleira deposit (Pimentel et al., 2003), which is almost contemporaneous to the emplacement of the Pojuca granite (1874

± 2 Ma; (Lindenmayer et al., 2001; Machado et al., 1991) in the northern CD. Indeed, Paleoproterozoic (ca. 1.90–1.85 Ga) felsic magmatism has been largely recognized at Carajás (Uatomã Event; Amaral, 1974) and involved the formation of several granitic intrusions (e.g., Serra dos Carajás Intrusive Suite) in the CD. Synchronous hydrothermal ore-forming events have also been proposed to justify the genesis of important IOCG deposits in the SCB, including Sossego and Alvo 118 (Moreto et al., 2015b; Torresi et al., 2012). Therefore, late hydrothermal pulses associated with the extensive Paleoproterozoic magmatism described at Carajás could possibly explain the ca. 1.81 Ga apatite age reported in this study.

6. Concluding remarks

Apatite major and trace element compositions, coupled with microtextural and U-Pb geochronological data, have revealed a complex evolution for the Santa Lúcia hydrothermal system. We argue that the observed compositional variations between different apatite generations (Sl-1, Sl-2, and SL-3) within the ore zones of the deposit is likely the result of intense metasomatism in a fluid system that got progressively more acidic and oxidizing in time. In this sense, the superimposition of metasomatic events in the deposit has been registered by apatite and involved at least three distinct hydrothermal pulses, which spanned from the Neoarchean (ca. 2.56 Ga) to the Paleoproterozoic (ca. 2.1 and 1.81 Ga).

References

Amaral, G., 1974. Geologia Pré-Cambriana da região amazônica. University of São Paulo.

Araújo Filho, R.C., Nogueira, A.C.R., Araújo, R.N., 2020. New stratigraphic proposal of a Paleoproterozoic siliciclastic succession: Implications for the evolution of the Carajás Basin, Amazonian craton, Brazil. J. South Am. Earth Sci. 102, 102665. https://doi.org/10.1016/j.jsames.2020.102665

Borba, M.L., Tassinari, C.C.G., Matos, F.M.V., Sato, K., Huhn, S., Ferreira, S.N., Medeiros, C.A., 2021. Tracking hydrothermal events using zircon REE geochemistry from the Carajás Mineral Province, Brazil. J. Geochemical Explor. 221, 106679. https://doi.org/10.1016/j.gexplo.2020.106679

Broom-Fendley, S., Styles, M.T., Appleton, J.D., Gunn, G., Wall, F., 2016. Evidence for dissolution-reprecipitation of apatite and preferential LREE mobility in carbonatite-derived late-stage hydrothermal processes. Am. Mineral. 101, 596–611. https://doi.org/10.2138/am-2016-5502CCBY

Cao, M., Li, G., Qin, K., Seitmuratova, E.Y., Liu, Y., 2012. Major and trace element characteristics of apatites in granitoids from central Kazakhstan: Implications for petrogenesis and mineralization. Resour. Geol. 62, 63–83. https://doi.org/10.1111/j.1751-3928.2011.00180.x

Cochrane, R., Spikings, R.A., Chew, D., Wotzlaw, J.F., Chiaradia, M., Tyrrell, S., Schaltegger, U., Van der Lelij, R., 2014. High temperature (>350°C) thermochronology

and mechanisms of Pb loss in apatite. Geochim. Cosmochim. Acta 127, 39–56. https://doi.org/10.1016/j.gca.2013.11.028

Dardenne, M.A., Ferreira Filho, C.F., Meirelles, M.R., 1988. The role of shoshonitic and calc-alkaline suites in the tectonic evolution of the Carajás District, Brazil. J. South Am. Earth Sci. 1, 363–372. https://doi.org/10.1016/0895-9811(88)90023-5

DOCEGEO, 1988. Revisão litocstratigráfica da Província Mineral de Carajás - Litoestratigrafia e principais depósitos minerais, in: XXXV Congresso Brasileiro de Geologia. SBG, Belém, pp. 11–54.

Feio, G.R.L., Dall'Agnol, R., Dantas, E.L., Macambira, M.J.B., Santos, J.O.S., Althoff, F.J., Soares, J.E.B., 2013. Archean granitoid magmatism in the Canaã dos Carajás area: Implications for crustal evolution of the Carajás province, Amazonian craton, Brazil. Precambrian Res. 227, 157–185. https://doi.org/10.1016/j.precamres.2012.04.007

Figueiredo e Silva, R.C., Lobato, L.M., Zucchetti, M., Hagemann, S., Vennemann, T., 2020. Geotectonic signature and hydrothermal alteration of metabasalts under- and overlying the giant Serra Norte iron deposits, Carajás mineral Province. Ore Geol. Rev. 120. https://doi.org/10.1016/j.oregeorev.2020.103407

Glorie, S., March, S., Nixon, A., Meeuws, F., O'Sullivan, G.J., Chew, D.M., Kirkland, C.L., Konopelko, D., De Grave, J., 2020. Apatite U–Pb dating and geochemistry of the Kyrgyz South Tian Shan (Central Asia): Establishing an apatite fingerprint for provenance studies. Geosci. Front. 11, 2003–2015. https://doi.org/10.1016/j.gsf.2020.06.003

Grainger, C.J., Groves, D.I., Tallarico, F.H.B., Fletcher, I.R., 2008. Metallogenesis of the Carajás Mineral Province, Southern Amazon Craton, Brazil: Varying styles of Archean through Paleoproterozoic to Neoproterozoic base- and precious-metal mineralisation. Ore Geol. Rev. 33, 451–489. https://doi.org/10.1016/j.oregeorev.2006.10.010

Griffin, W.L., Powell, W.J., Pearson, N.J., O'Reilly, S.Y., 2008. Glitter: Data reduction software for laser ablation ICP-MS, in: Sylvester, P. (Ed.), Laser Ablation ICP-MS in the Earth Sciences: Current Practices and Outstanding Issues. Short Course Series, Volume 40. Mineralogical Association of Canada, pp. 308–311. https://doi.org/10.2113/gsecongeo.104.4.601

Harlov, D.E., 2015. Apatite: A fingerprint for metasomatic processes. Elements 11, 171–176. https://doi.org/10.2113/gselements.11.3.171

Harlov, D.E., Wirth, R., Förster, H.J., 2005. An experimental study of dissolution-reprecipitation in fluorapatite: Fluid infiltration and the formation of monazite. Contrib. to Mineral. Petrol. 150, 268–286. https://doi.org/10.1007/s00410-005-0017-8

Hunger, R.B., Melo, G.H.C., Xavier, R.P., Moreto, C.P.N., Talavera, C., Su, Z.K., Zhao, X.F., 2021. The Santa Lúcia Cu-Au deposit, Carajás Mineral Province, Brazil: a Neoarchean (2.68 Ga) member of the granite-related copper-gold systems of Carajás. Miner. Depos. https://doi.org/10.1007/s00126-020-01034-z

Hunger, R.B., Xavier, R.P., Moreto, C.P.N., Gao, J.-F., 2018. Hydrothermal Alteration, Fluid Evolution, and Re-Os Geochronology of the Grota Funda Iron Oxide Copper-Gold Deposit, Carajás Province (Pará State), Brazil. Econ. Geol. 113, 1769–1794. https://doi.org/10.5382/econgeo.2018.4612

Jochum, K.P., Weis, U., Schwager, B., Stoll, B., Wilson, S.A., Haug, G.H., Andreae, M.O., Enzweiler, J., 2016. Reference Values Following ISO Guidelines for Frequently

Requested Rock Reference Materials. Geostand. Geoanalytical Res. 40, 333–350. https://doi.org/10.1111/j.1751-908X.2015.00392.x

Ketcham, R.A., 2015. Technical Note: Calculation of stoichiometry from EMP data for apatite and other phases with mixing on monovalent anion sites. Am. Mineral. 100, 1620–1623. https://doi.org/10.2138/am-2015-5171

Kirkland, C.L., Yakymchuk, C., Szilas, K., Evans, N., Hollis, J., McDonald, B., Gardiner, N.J., 2018. Apatite: a U-Pb thermochronometer or geochronometer? Lithos 318–319, 143–157. https://doi.org/10.1016/j.lithos.2018.08.007

Krneta, S., Ciobanu, C.L., Cook, N.J., Ehrig, K., Kontonikas-Charos, A., 2017. Rare Earth Element Behaviour in Apatite from the Olympic Dam Cu–U–Au–Ag Deposit, South Australia. Minerals 7, 1–26. https://doi.org/10.3390/min7080135

Lana, C., Gonçalves, G.O., Mazoz, A., Buick, I., Kamo, S., Scholz, R., Wang, H., Moreira, H., Babinski, M., Queiroga, G., 2022. Assessing the U-Pb, Sm-Nd and Sr-Sr Isotopic Compositions of the Sumé Apatite as a Reference Material for LA-ICP-MS Analysis. Geostand. Geoanalytical Res. 46, 71–95. https://doi.org/10.1111/ggr.12413

Li, J., Ye, C., Ying, J., 2022. In Situ Geochemical and Sr-Nd Isotope Analyses of Apatite from the Shaxiongdong Alkaline-Carbonatite Complex (South Qinling, China): Implications for magma evolution and mantle source. Minerals 12, 1–19.

Lima, F.D., 2002. Evolução Tectônica da Terminação Leste da Falha Carajás, Sul do Estado do Pará. Universidade Federal do Pará.

Lindenmayer, Z.G., Pimentel, M.M., Ronchi, L.H., Althoff, F.J., Laux, J.H., Araújo, J.C., Fleck, A., Baecker, C.A., Carvalho, D.B., Nowatzki, A.C., 2001. Geologia do depósito de Cu-Au de Gameleira, Serra dos Carajás, Pará, in: Jost, H., Brod, J.A., Queiroz, E.T. (Eds.), Caracterização de Depósitos Auríferos Em Distritos Mineiros. DNPM/ADIMB, Brasília, pp. 81–139.

Lu, J., Chen, W., Ying, Y., Jiang, S., Zhao, K., 2021. Apatite texture and trace element chemistry of carbonatite-related REE deposits in China: Implications for petrogenesis. Lithos 398–399, 106276. https://doi.org/10.1016/j.lithos.2021.106276

Machado, N., Lindenmayer, Z., Krogh, T.E., Lindenmayer, D., 1991. U-Pb geochronology of Archean magmatism and basement reactivation in the Carajás area, Amazon shield, Brazil. Precambrian Res. 49, 329–354. https://doi.org/10.1016/0301-9268(91)90040-H

Mansur, E.T., Ferreira Filho, C.F., 2016. Magmatic structure and geochemistry of the Luanga Mafic–Ultramafic Complex: Further constraints for the PGE-mineralized magmatism in Carajás, Brazil. Lithos 266–267, 28–43. https://doi.org/10.1016/j.lithos.2016.09.036

Mao, M., Rukhlov, A.S., Rowins, S.M., Spence, J., Coogan, L.A., 2016. Apatite trace element compositions: A robust new tool for mineral exploration. Econ. Geol. 111, 1187–1222. https://doi.org/10.2113/econgeo.111.5.1187

McDonough, W.F., Sun, S. -s., 1995. The composition of the Earth. Chem. Geol. 120, 223–253.

Melo, G.H.C., Monteiro, L.V.S., Xavier, R.P., Moreto, C.P.N., Santiago, E.S.B., Dufrane, S.A., Aires, B., Santos, A.F.F., 2016. Temporal evolution of the giant Salobo IOCG deposit, Carajás Province (Brazil): Constraints from paragenesis of hydrothermal alteration and U-Pb geochronology. Miner. Depos. 52, 709–732. https://doi.org/10.1007/s00126-016-0693-5

Mercer, C.N., Watts, K.E., Gross, J., 2020. Apatite trace element geochemistry and cathodoluminescent textures—A comparison between regional magmatism and the Pea Ridge IOAREE and Boss IOCG deposits, southeastern Missouri iron metallogenic province, USA. Ore Geol. Rev. 116, 103129. https://doi.org/10.1016/j.oregeorev.2019.103129

Moreto, C.P.N., Monteiro, L.V.S., Xavier, R.P., Creaser, R.A., DuFrane, S.A., Melo, G.H.C., Silva, M.A.D., Tassinari, C.C.G., Sato, K., 2015a. Timing of multiple hydrothermal events in the iron oxide–copper–gold deposits of the Southern Copper Belt, Carajás Province, Brazil. Miner. Depos. 50, 517–546. https://doi.org/10.1007/s00126-014-0549-9

Moreto, C.P.N., Monteiro, L.V.S., Xavier, R.P., Creaser, R.A., DuFrane, S.A., Tassinari, C.C.G., Sato, K., Kemp, A.I.S., Amaral, W.S., 2015b. Neoarchean and paleoproterozoic iron oxide-copper-gold events at the Sossego deposit, Carajás Province, Brazil: Re-Os and U-Pb geochronological evidence. Econ. Geol. 110, 809–835. https://doi.org/10.2113/econgeo.110.3.809

Motta, J.G., Souza Filho, C.R. d., Carranza, E.J.M., Braitenberg, C., 2019. Archean crust and metallogenic zones in the Amazonian Craton sensed by satellite gravity data. Sci. Rep. 9, 1–10. https://doi.org/10.1038/s41598-019-39171-9

O'Sullivan, G., Chew, D., Kenny, G., Henrichs, I., Mulligan, D., 2020. The trace element composition of apatite and its application to detrital provenance studies. Earth-Science Rev. 201, 103044. https://doi.org/10.1016/j.earscirev.2019.103044

OZ Minerals, 2019. ASX Release - Carajás Hub strategy gains pace.

Pimentel, M.M., Lindenmayer, Z.G., Laux, J.H., Armstrong, R.A., Araújo, J.C., 2003. Geochronology and Nd isotope geochemistry of the Gameleira Cu – Au deposit, Serra dos Carajás, Brazil: 1.8 - 1.7 Ga hydrothermal alteration and mineralization. J. South Am. Earth Sci. 15, 803–813.

Pinheiro, R.V.L., Kadekaru, K., Soares, A.V., Freitas, C., Ferreira, S.N., Matos, F.M.V., 2013. Carajás, Brazil - a short tectonic review, in: XIII Simpósio de Geologia Da Amazônia. SBG, Belém, pp. 1086–1089.

Pollard, P.J., Taylor, R.G., Peters, L., Matos, F., Freitas, C., Saboia, L., Huhn, S., 2019. 40Ar-39Ar dating of Archean iron oxide Cu-Au and Paleoproterozoic granite-related Cu-Au deposits in the Carajás Mineral Province, Brazil: implications for genetic models. Miner. Depos. 54, 329–346. https://doi.org/10.1007/s00126-018-0809-1

Previato, M., Monteiro, L.V.S., Bello, R.M. da S., Gonçales, L.C.G., 2020. Evolution of brines and CO2-rich fluids and hydrothermal overprinting in the genesis of the Borrachudo copper deposit, Carajás Province. Ore Geol. Rev. 121, 103561. https://doi.org/10.1016/j.oregeorev.2020.103561

Silva, J.P.A., 2020. Saturn – Uma nova ferramenta de correção de dados U-Pb para LA-ICP-MS. Federal University of Ouro Preto.

Silva, M.A.D., Monteiro, L.V.S., Santos, T.J.S., Moreto, C.P.N., Sousa, S.D., Faustinoni, J.M., Melo, G.H.C., Xavier, R.P., Toledo, B.A.M., 2021. Mesoarchean migmatites of the Carajás Province: From intra-arc melting to collision. Lithos 388–389, 106078. https://doi.org/10.1016/j.lithos.2021.106078

Tallarico, F.H.B., McNaughton, N.J., Groves, D.I., Fletcher, I.R., Figueiredo, B.R., Carvalho, J.B., Rego, J.L., Nunes, A.R., 2004. Geological and SHRIMP II U-Pb constraints on the

age and origin of the Breves Cu-Au-(W-Bi-Sn) deposit, Carajás, Brazil. Miner. Depos. 39, 68–86. https://doi.org/10.1007/s00126-003-0383-y

Tavares, F.M., Trouw, R.A.J., da Silva, C.M.G., Justo, A.P., Oliveira, J.K.M., 2018. The multistage tectonic evolution of the northeastern Carajás Province, Amazonian Craton, Brazil: Revealing complex structural patterns. J. South Am. Earth Sci. 88, 238–252. https://doi.org/10.1016/j.jsames.2018.08.024

Thompson, J., Meffre, S., Maas, R., Kamenetsky, V., Kamenetsky, M., Goemann, K., Ehrig, K., Danyushevsky, L., 2016. Matrix effects in Pb/U measurements during LA-ICP-MS analysis of the mineral apatite. J. Anal. At. Spectrom. 31, 1206–1215. https://doi.org/10.1039/c6ja00048g

Thomson, S.N., Gehrels, G.E., Ruiz, J., Buchwaldt, R., 2012. Routine low-damage apatite U-Pb dating using laser ablation-multicollector-ICPMS. Geochemistry, Geophys. Geosystems 13. https://doi.org/10.1029/2011GC003928

Toledo, P.I. de F., Moreto, C.P.N., Xavier, R.P., Gao, J., Matos, J.H. da S.N. de, Melo, G.H.C., 2019. Multistage Evolution of the Neoarchean (ca. 2.7 Ga) Igarapé Cinzento (GT-46) Iron Oxide Copper-Gold Deposit, Cinzento Shear Zone, Carajás Province, Brazil. Econ. Geol. 114, 1–34. https://doi.org/10.5382/econgeo.2019.4617

Torresi, I., Xavier, R.P., Bortholoto, D.F.A., Monteiro, L.V.S., 2012. Hydrothermal alteration, fluid inclusions and stable isotope systematics of the Alvo 118 iron oxide-copper-gold deposit, Carajás Mineral Province (Brazil): Implications for ore genesis. Miner. Depos. 47, 299–323. https://doi.org/10.1007/s00126-011-0373-4

Van Achterberg, E., Ryan, C., Jackson, S.E., Griffin, W.L., 2001. Data reduction software for LA-ICP-MS. Laser Ablation ICP-MS Earth Sci. 29, 239–243.

Vasquez, M.L., Macambira, M.J.B., Armstrong, R.A., 2008. Zircon geochronology of granitoids from the western Bacajá domain, southeastern Amazonian craton, Brazil: Neoarchean to Orosirian evolution. Precambrian Res. 161, 279–302. https://doi.org/10.1016/j.precamres.2007.09.001

Vermeesch, P., 2018. IsoplotR: A free and open toolbox for geochronology. Geosci. Front. 9, 1479–1493. https://doi.org/10.1016/j.gsf.2018.04.001

Volp, K.M., 2005. The Estrela copper deposit, Carajás, Brazil: Geology and implications of a Proterozoic copper stockwork. Miner. Depos. Res. Meet. Glob. Chall. - Proc. Eighth Bienn. SGA Meet. 1085–1088.

Webster, J.D., Piccoli, P.M., 2015. Magmatic apatite: A powerful, yet deceptive, mineral. Elements 11, 177–182. https://doi.org/10.2113/gselements.11.3.177

Xavier, R.P., Monteiro, L.V.S., Moreto, C.P.N., Pestilho, A.L.S., Melo, G.H.C., Silva, M.A.D., Aires, B., Ribeiro, C., Silva, F.H.F., 2012. The iron oxide copper-gold systems of the Carajás mineral province. Econ. Geol. 16, 433–454.

Xavier, R.P., Moreto, C.P.N., Melo, G.H.C., Toledo, P.I. de F., Hunger, R.B., Delinardo da Silva, M.A., Faustinoni, J.M., Lopes, A.M., Monteiro, L.V.S., Previato, M., Jesus, S. dos S.G.P., Huhn, S.R.B., 2017. Geology and Metallogeny of Neoarchean and Paleoproterozoic Copper Systems of the Carajás Domain, Amazonian Craton, Brazil, in: 14th SGA Biennial Meeting. SGA, Quebéc, pp. 899–902.

Xiang, D., Zhang, Z., Zack, T., Chew, D., Yang, Y., Wu, L., Hogmalm, J., 2021. Apatite U-Pb Dating with Common Pb Correction Using LA-ICP-MS/MS. Geostand. Geoanalytical Res. 45, 621–642. https://doi.org/10.1111/ggr.12404

Appendix 1 Representative major element data for apatite at Santa Lúcia

EPMA (wt%)	SL-1 + SL-2 (n = 179)		SL-3 (n = 67)	
	Mean	Range	Mean	Range
CaO	53.78	46.71–55.73	54.32	49.72–56.44
SrO	0.02	0.001–0.08	0.02	0.001–0.06
Na_2O	0.02	0.001–0.10	0.01	0.001–0.01
La_2O_3	0.03	0.002–0.10	0.03	0.002–0.07
Ce_2O_3	0.06	0.003–0.15	0.02	0.002–0.10
Pr_2O_3	0.04	0.001–0.15	0.03	0.001–0.10
Nd_2O_3	0.06	0.001–0.19	0.04	0.001–0.11
MnO	0.18	0.08–0.28	0.04	0.01–0.15
FeO	0.12	0.01–0.40	0.20	0.004–5.22
BaO	0.02	0.001–0.05	0.02	0.002–0.04
K_2O	0.003	0.001–0.02	0.004	0.001–0.04
Al_2O_3	0.01	0.001–0.46	0.02	0.001–0.28
P_2O_5	41.90	36.66–43.18	42.30	39.62–43.60
SiO_2	0.15	0.001–13.67	0.02	0.001–0.16
SO_3	0.01	0.001–0.22	0.17	0.001–5.85
TiO_2	0.00	0.001–0.02	0.00	0.001–0.01
F	4.88	3.18–7.19	5.07	4.37–6.91
Cl	0.20	0.09–0.31	0.05	0.003–0.15
–O = F,Cl	-2.10	-1.36–-3.10	-2.15	-1.84–-2.94
Total	99.31	97.56–101.49	100.10	98.11–104.09
Est. OH	0.26	0.05–0.48	-	BDL
Net Correct. Total	99.31	97.56–101.49	100.10	98.11–104.09

Abbreviations: BDL = below detection limit

Appendix 2 Representative trace element compositions of apatite at Santa Lúcia

LA-ICP-MS (ppm)	SL-1 (n = 20)		SL-2 (n = 26)		SL-3 (n = 19)	
	Mean	Range	Mean	Range	Mean	Range
Mg	108.99	76.25–168.28	125.07	16.33–189.23	11.92	0.50–85.31
Si	1036.96	303.29–2327.25	908.18	126.04–3221.63	982.61	281.76–2277.96
Sc	1.30	0.69–3.41	1.01	0.45–1.38	0.89	0.50–1.19
Ti	714.00	564.96–873.21	678.58	584.84–848.45	682.30	579.98–855.24
V	0.17	0.02–1.10	0.04	0.02–0.11	0.02	0.02–0.02
Mn	1679.80	1367.89–2403.58	1764.41	550.94–2472.70	524.39	175.75–1205.01
Cu	26.53	17.33–129.23	20.73	6.57–54.05	18.72	2.86–24.86
Ga	0.19	0.10–0.51	0.16	0.04–1.23	0.06	0.02–0.24
Ge	26.97	16.71–39.50	18.45	7.95–31.33	4.69	2.30–12.52
Rb	0.28	0.15–0.62	0.21	0.06–0.69	0.04	0.02–0.10
Sr	261.36	188.62–307.78	249.11	170.38–322.95	137.43	88.20–210.01
Y	1452.25	905.25–2141.21	938.54	336.73–1527.23	184.69	48.54–516.28
Nb	0.06	0.02–0.42	0.13	0.01–1.18	0.03	0.02–0.04
Mo	1.03	0.80–1.42	1.01	0.29–1.66	0.34	0.15–0.62
Cd	0.12	0.08–0.21	0.13	0.05–0.22	0.10	0.03–0.62
Sn	0.10	0.04–0.17	0.10	0.05–0.46	0.10	0.04–0.17
Sb	0.04	0.01–0.09	0.02	0.01–0.11	0.02	0.01–0.11
Ba	0.89	0.25–3.76	0.99	0.16–10.26	0.18	0.11–0.31
La	218.50	138.02–627.17	135.19	36.66–216.05	18.62	2.71–93.51
Ce	762.08	489.97–1522.63	501.71	150.97–792.81	84.88	21–356.80
Pr	109.10	70.18–183.98	71.73	24.78–116.27	14.64	4.95–49.22
Nd	474.23	300.24–713.68	318.37	132.08–525.67	76.53	32.02–215.20
Sm	154.94	93.16–213.44	103.85	54.09–178.15	35.70	21.25–67.83
Eu	15.23	9.35–21.02	10.29	5.51–17.81	3.92	2.22–6.85
Gd	143.15	88.08–206.63	93.95	44.30–153.89	27.36	11.39–62.58
Tb	52.52	31.17–71.51	33.77	18.68–55.50	12.69	5.05–21.07
Dy	285.82	170.77–410.88	183.69	94.28–318.64	59.18	19.67–110.76
Ho	67.40	40.84–99.76	42.74	17.01–72.65	9.74	2.88–24.76
Er	139.75	85.58–204.39	87.79	27.34–147.79	15.36	4.59–49.96
Tm	19.94	12.04–31.68	12.39	3.32–21.35	1.64	0.44–7.11
Yb	83.42	48.74–134.68	51.43	12.74–89.38	6.49	1.84–28.30
Lu	10.15	6.17–16.83	6.37	1.44–11.31	0.71	0.18–3.60
Hf	0.31	0.16–1.05	0.20	0.14–0.31	0.24	0.17–0.31
W	0.09	0.03–0.15	0.07	0.03–0.31	0.03	0.02–0.06
Pb	0.57	0.40–0.90	0.54	0.12–1.74	0.05	0.01–0.23
Th	0.06	0.01–0.24	0.01	0.002–0.09	0.01	0.002–0.04
U	2.22	0.27–5.65	0.65	0.12–2.09	0.03	0.001–0.15

Appendix 2 (continued)

LA-ICP-MS (ppm)	SL-1 (n = 20)		SL-2 (n = 26)		SL-3 (n = 19)	
	Mean	Range	Mean	Range	Mean	Range
Total REE + Y	3988.49	2513.07–5678.05	2591.81	968.26–4188.25	552.14	178.72–1613.83
Total LREE	1563.91	1005.80–3047.46	1027.00	344.49–1650.80	194.66	60.68–714.73
La_N/Yb_N	1.84	1.20–5.02	1.82	1.17–2.37	1.83	1.00–2.42
Ce/Ce*	1.21	1.08–1.30	1.23	1.17–1.31	1.26	1.15–1.39
Eu/Eu*	0.31	0.29–0.35	0.32	0.30–0.35	0.39	0.32–0.43

Appendix 3 $^{207}Pb/^{235}U$ and $^{206}Pb/^{238}U$ ratios with their respective uncertainties (2σ) for the analysed apatite grains

Age group	Spot number	$^{207}Pb/^{235}U$	2σ (%)	$^{206}Pb/^{238}U$	2σ (%)	Rho
ca. 2.56	036	19.77639	3.50369	0.53128	1.61716	0.46156
	038	20.92847	6.11403	0.54293	1.83507	0.30014
	041	20.64672	3.22059	0.53828	1.65003	0.51234
	042	24.46456	0.95110	0.55646	0.78571	0.82611
	048	24.29798	16.83677	0.55699	3.79133	0.22518
	049	23.90599	3.98061	0.54957	1.85788	0.46673
	056	26.83765	6.94338	0.56927	2.44409	0.35200
	061	26.37558	16.59849	0.56783	3.87676	0.23356
	063	25.24479	6.44543	0.55934	2.38992	0.37079
	068	22.18110	1.37667	0.54150	0.95008	0.69013
ca. 2.1	035	15.09315	0.99036	0.43116	0.79892	0.80670
	037	16.41893	0.97033	0.43515	0.67840	0.69914
	039	11.48282	0.43575	0.40823	0.41522	0.95289
	050	14.93517	1.61655	0.42817	1.05625	0.65340
	054	13.12405	2.49555	0.41718	1.26235	0.50584
	058	12.58117	1.07285	0.41592	0.80084	0.74646
	062	15.93423	1.68190	0.43571	1.07470	0.63898
	067	15.81191	1.03154	0.43112	0.74838	0.72550
ca. 1.81	063	58.74543	3.83697	0.62893	1.88578	0.49148
	064	20.49184	0.74929	0.41598	0.74076	0.98862
	065	48.43514	3.99359	0.57366	1.92243	0.48138
	068	61.26685	6.12296	0.63951	2.40276	0.39242
	069	26.67258	2.99108	0.44810	1.37574	0.45995
	073	23.57799	0.72753	0.42948	0.63772	0.87656
	075	21.94852	0.51102	0.42109	0.55585	0.91936
	076	57.43972	7.06995	0.61980	2.55438	0.36130
	077	24.31033	1.24710	0.43643	0.98010	0.78590
	078	29.10133	2.62071	0.46547	1.47825	0.56407
	079	40.85892	1.43842	0.53041	1.10374	0.76733
	080	30.27159	1.16099	0.47197	0.96758	0.83341
	081	29.17223	1.69733	0.46557	1.20926	0.71245
	082	26.66302	1.09224	0.45153	0.94275	0.86313
	085	36.07320	1.79059	0.50451	1.22323	0.68314